Chair of Reservoir Engineering

Master's Thesis

Mechanistic Study of Fracture Types Effect on Oil Production

Milos Pejic, BSc

September 2021

Milos Pejic

Master Thesis 2021

Supervisor: Univ.-Prof. Riyaz Kharrat

Mechanistic Study of Fracture Types Effect on Oil Production

dpe DEPARTMENT PETROLEUM ENGINEERING

MONTAN UNIVERSITÄT

Declaration

I hereby declare that except where specific reference is made to the work of others, the contents of this dissertation are original and have not been published elsewhere. This dissertation is the outcome of my own work using only cited literature.

Erklärung

Hiermit erkläre ich, dass der Inhalt dieser Dissertation, sofern nicht ausdrücklich auf die Arbeit Dritter Bezug genommen wird, ursprünglich ist und nicht an anderer Stelle veröffentlicht wurde. Diese Dissertation ist das Ergebnis meiner eigenen Arbeit mit nur zitierter Literatur.

Name, 21 September 2021

Acknowledgments

First of all, I would like to express my sincere gratitude to my supervisor Prof. Riyaz Kharrat for his continuous support throughout my masters. Our meetings and his vast knowledge helped me to finish my studies and this thesis. I am also very thankful for the opportunity to be able to do this research.

I would also like to thank Prof. Ali Kadkhodaie for his constant willingness to help and his valuable support.

In addition, my sincere thanks also go to my friends Nouri Alalim, Moad Ben-Ramadan, and Peyman Nazifi for our discussions and their helpful advice.

Abstract

Since more than half of the world's crude oil is stored in naturally fractured reservoirs, and easy-to-produce oils are diminishing over time, more and more research has been focused on understanding fractured reservoirs' complex production behavior. Natural fractures can be determined via FMI logs and classified according to their aperture into groups. This work features the effect of different types of fractures on oil production in primary production, waterflooding, and gas injection in a carbonate reservoir. Numerous simulation cases were run under different conditions to study the effects of different fracture sets on production. Firstly, synthetic 2D models were created as a fundament for the 3D cube model. Primary production, waterflooding, and gas injection were studied in these models, and the results are discussed in this work. Furthermore, a sector from a real giant fractured carbonated field was taken, and with the lessons learned from the synthetic models, it was studied for primary production. Verification of the results was found by getting results that follow the historical production data of the real field sector. Moreover, sensitivity runs were conducted with the 3D cube model for waterflooding and gas injection, and dimensionless numbers for these runs were calculated. The capillary number, defined as the capillary force over the viscous, and the gravity number, defined as the gravitational force over the viscous, gives insight into which forces flow through the fractured reservoir is governed.

Based on the obtained results from the synthetic and real field sector models, fractures play a key role in production. Ignoring any of the present fracture types, especially the major ones, might underestimate the reservoir's capabilities for natural depletion. In the case of waterflooding, fractures also promote higher recovery and better displacement, whereas, for the gas injection, faster breakthrough times were observed. The performance during gas injection was found to be more dependent on matrix permeability changes compared to waterflooding. This statement is also confirmed with dimensionless numbers, where for the gas injection, higher recoveries were found under matrix-dominated flow. Waterflooding, on the other hand, shows more sensitivity towards fracture properties.

Zusammenfassung

Da mehr als die Hälfte des weltweiten Rohöls in natürlich frakturierten Lagerstätten vorkommt und leicht zu fördernde Kohlenwasserstoffe im Laufe der Zeit versiegen, wird immer mehr Wert auf das Verständnis des komplexen Förderverhaltens von frakturierten Lagerstätten gelegt. Diese Arbeit umfasst große, mittlere, kleine und für den Fall des realen Feldes auch Haarrisse, die in Bezug auf ihre Öffnungsweite in absteigender Reihenfolge angeordnet sind. Zahlreiche Simulationen wurden unter verschiedenen Bedingungen durchgeführt, um die Auswirkungen verschiedener Zusammensetzungen von unterschiedlichen Rissen auf die Produktion zu untersuchen. Zunächst wurden künstliche 2D-Modelle erstellt, die als Grundlage für das darauffolgende 3D-Würfelmodell dienen. Natürliche Produktion, Wasserflutung und Gasinjektion wurden in diesen Modellen untersucht und die Ergebnisse werden in dieser Arbeit diskutiert. Darüber hinaus wurde ein Sektor aus einem echten riesigen Feld ausgewählt und mit den Erkenntnissen aus den synthetischen Modellen während der natürlichen Produktion untersucht. Es wurde eine Verifizierung der Arbeit ermöglicht, indem die erhaltenen Ergebnisse dem Trend der historischen Produktionsdaten des realen Feldsektors Folge leisten. Darüber hinaus wurden Sensitivitäts-Durchläufe mit dem 3D-Würfelmodell für die Wasserflutung und Gasinjektion durchgeführt und dimensionslose Kennzahlen für die selbigen berechnet. Die “capillary number” und die “gravity number”, jeweils definiert als Verhältnis der Kapillarkraft bzw. der Gravitationskraft durch die viskose Reibungskraft, geben Aufschluss darüber, unter welchen Kräften die durch Risse gekennzeichnete Lagerstätte dominiert wird.

Basierend auf den gewonnenen Ergebnissen aus den synthetischen und echten Sektor-Modellen spielen Risse eine Schlüsselrolle in der Produktion. Das Ignorieren eines der untersuchten Risstypen, insbesondere der großen Risse, könnte dazu führen die Lagerstätte als solche in Bezug auf natürliche Produktion zu unterschätzen. Während des Wasserflutens begünstigen Risse zudem eine höhere Produktion und eine bessere Verdrängung, während bei der Gasinjektion schnellere Durchbruchszeiten des Gases beobachtet wurden. Die Performance der Gasinjektion im Vergleich zum Wasserfluten scheint stärker von Änderungen der Matrixpermeabilität abzuhängen. Diese Feststellung wird auch durch die dimensionslosen Kennzahlen gestützt, unter welchen während der Gasinjektion höhere Ausbeuten bei matrixdominiertem Fluss beobachtet wurden. Wasserfluten hingegen zeigt eine größere Sensibilität gegenüber den Eigenschaften der Frakturen selbst.

Table of Contents

List of Figures

List of Tables

Nomenclature

Φ	porosity	[%]
g	gravitational constant	[m/s^2]
H	reservoir thickness	[m]
k_i	rel. perm. of phase i	[-]
k_f	perm. of fracture	[m^2]
k_m	perm. of matrix	[m^2]
L	reservoir length	[m]
λ_i	mobility of phase i	[1/Pa.s]
m	mass	[kg]
M	mobility ratio	[-]
$N_{cv,m}$	capillary number	[-]
$N_{gv,f}$	gravity number	[-]
μ_i	viscosity of phase i	[Pa.s]
p_{avg}	avg. reservoir pressure	[Pa]
p_{BH}	bottom hole pressure	[Pa]
p_c^*	transv. capillary pressure	[Pa]
q_f	Darcy flow vel. fracture	[m/s]
q_m	Darcy flow vel. matrix	[m/s]
r	radius	[m]
θ	contact angle	[°]
σ	interfacial tension	[N/m]
σ_{SF}	shape factor	[1/m^2]
ρ_i	density of phase i	[kg/m$^{3]}$
Rf	recovery factor	[%]
V	matrix volume	[m^3]

Abbreviations

BT	Breakthrough
DFN	Discrete Fracture Network
EMI	Electrical Micro-Imager
EOR	Enhanced Oil Recovery
FMI	Formation Micro-Imager
GAGD	Gas Assisted Gravity Drainage
HF	Hydraulic fracture
ISC	In-Situ Combustion
MW	Mixed wet wettability conditions
NF	Natural fracture
NFR	Naturally Fractured Reservoir
OW	Oil wet wettability conditions
PI	Productivity Index
SAGD	Steam Assisted Gravity Drainage
THAI	Toe-to-Heel Air Injection
VAPEX	Vapor Assisted Petroleum Extraction
WF	Waterflood
WW	Water wet wettability conditions

Chapter 1

Introduction

Until today, crude oil and gas are one of the primary energy sources modern humanity builds on. Although in most recent times, global demand dropped due to the worldwide Covid-19 pandemic and the correlated industrial and economic restrictions. Various sources state that, again, an increase in demand will follow soon (EIA, 2021; Sönnichsen, 2021). Approximately half of the worldwide crude oil reservoirs are fractured reservoirs characterized by specific production mechanisms (Kharrat, et al., 2021). The matrix-fracture system creates effects such as imbibition and drainage for water and gas injections. Many studies have been published so far regarding these effects (Firoozabadi, 2000; Kovscek, et al., 2001). Also, development strategies and simulation work of mechanisms or EOR screening involve special consideration of methods for the successful study of fractured reservoirs. Usually, such works involve Discrete Fracture Networks and dual-continuum models (Torres, et al., 2020). Naturally fractured reservoirs are considered to hold significant amounts of remaining crude oil reserves. Especially considering the fact that easily accessible hydrocarbon is diminishing slowly over the years. Understanding and using the complex production behavior of fractured reservoirs is projected to be a key element of providing the futures energy demand (Spence, et al., 2014).

1.1 Background and Objectives

Many hydrocarbon fields around the globe are considered to bear fractured reservoirs. For decades hydrocarbons have been produced from such fields, without even considering if the field's geology is fractured or not. This work tries to emphasize the importance of correct fracture estimation on oil production based on an example of the GH-field in Iran. The GH field, as of 2021, is considered a brown field, with decades of successful oil production. It holds several hundred wells, and data from many of these wells are used to construct a good

estimation of the natural fractures of this field. This information allows us to prove the importance of fractures via running simulation cases of the GH-field. Since a history match exists, a comparison of different runs with the real field data is possible. What would happen if the field had less fractures than it has? Which impact do fractures have on production, especially if they are categorized into groups in respect to their aperture? Simple questions such as these show that the effect of fractures on production deserves to be studied in more detail.

Chapter 2

Literature Review

This chapter gives insight in the basic principles of oil recovery in fractured reservoirs.

2.1 Effect of Fractures on Production

The flow of the three present phases (oil, gas, and water) in natural hydrocarbon reservoirs can be simplified into fluid flow through porous media. In her vast and beautiful heterogeneity, nature often provides hydrocarbons in fractured reservoir rocks. By doing so, she creates additional objectives that must be understood when the fluid flow through natural porous media is studied. Naturally fractured reservoirs, often referred to as NFRs, are scattered worldwide and, thus, are known to humankind for already a long time (Saidi, 1987). Fractures implied that they are not filled with cement and provide highly permeable channels, dividing the less permeable matrix blocks. This creates a highly complex rock structure and altered fluid flow mechanisms compared to conventional reservoirs (Litvak, et al., 1988).

Studies about the effects of fractures on primary, secondary, and tertiary production stages were conducted many times in the past (Bahrami, et al., 2012; Doe, et al., 2013; Gong & Rossen, 2018; Wei, et al., 2019). According to the information stated in the literature, at the beginning of the production life cycle, mostly oil fills the matrix pores and fractures. In the initial primary recovery, first the oil from the fractures is produced, resulting in very high recovery peaks, which may decline in a short amount of time (Kleppe & Morse, 1974). Additionally, it was stated that fracture properties such as aperture, length, and spacing play a significant role in studying the effects of fractures (Gong & Rossen, 2016). After the primary production diminishes, the secondary production in the form of a waterflood often starts, after which an increase in water saturation in the fractures can be observed. Assuming a vertical set of fractures and matrix blocks, the water level rises first through the fractures. But due to gravity differences and imbibition, water starts encroaching into the matrix, slowly displacing the oil. Hence, for

the waterflood, it can be stated that before the breakthrough (BT) of water, almost 100% of the oil came from the fracture network. After the BT, all the fractures are filled with water, and the produced oil comes from the matrix (Rezaveisi, et al., 2012).

One of the primary mechanisms for gas injection in NFRs is Gas Assisted Gravity Drainage (GAGD). Gas filled fractures surround the oil-filled matrix blocks, and the gas can diffuse (gravity driven) into the matrix, displacing the oil. It was found that fracture permeability is a key property for high oil recovery when gas is injected in NFRs. Even higher recovery can be achieved when the vertical fracture permeability is higher than the horizontal fracture permeability (Silva & Maini, 2016). Interestingly, the fracture conductivity is less important than the fracture spacing, if the gas is injected in a "huff and puff" regime. During a cyclic gas injection, lower fracture spacings result in higher recoveries (Wan, et al., 2016). Another feature important for gravity drainage to occur during gas injection is to have a sufficiently long reservoir in the direction of the gravity. Aghabrari and his colleagues created a model of stacked matrix blocks in the vertical direction, separated by fractured medium, allowing oil to re-imbibe from matrix to matrix forced by gravity drainage of gas (Aghabarari, et al., 2020).

Nowadays, with many fields being brown fields for decades and most of the light oils being produced, the effect of fractures in combination with different EOR methods is of interest. The Water Alternating Gas EOR method in NFR works because the gas prefers to flow in the high permeable fractures, resulting in gravity drainage. On the other hand, the water imbibes the matrix blocks and further increases oil displacement efficiency. For the WAG process, high permeable fractures and low permeable matrices are important for a successful application (Heeremans, et al., 2006).

Intensive studies were conducted in thermal EOR, where investigations for a number of methods were published. A review of the thermal methods for fractured carbonate reservoirs has been provided by Ghoodjani et al. (2011). For the In-Situ Combustion (ISC), the effects of fractures were studied by varying the fracture density, spacing, and length for vertical and horizontal fractures. The literature states that too-long fractures result in earlier BT of oxygen, leading to a poor sweep efficiency. The spacing of the fractures in vertical and horizontal directions should be towards the lateral boundaries, and the fracture density should not be too high. A dense fracture population with close spacing between each other results in faster BT and a loss in oxygen utilization; both effects lower the overall oil recovery efficiency (Fatemi, et al., 2014). Fractures can enhance the Steam Assisted Gravity Drainage (SAGD) performance by enabling a larger contact area between hot steam and oil. The steam bypasses through high permeable fractures the heavy oil in the middle of the matrix, allowing the oil to drain towards the producer. In general, vertical fractures increase the performance of SAGD by optimizing

the hot steam chamber shape, whereas horizontal fractures mitigate the effectiveness of SAGD. Also, discontinuities lead to a decreased SAGD performance, not allowing the chamber to develop properly (Fatemi, et al., 2011). Like the SAGD, the Vapor Assisted Petroleum Extraction (VAPEX) process can also profit from NFRs compared to conventional reservoirs. Fractures distribute the solvent over wider areas, meaning that the reaction time between vapor and oil increases. Over low permeable regions, fractures enhance the contact area between solvent vapor and oil in the matrix, thus delaying the BT of vapor. Higher oil recovery and delayed BT also occur because the overall shape of the vapor front changes with fractures at the lateral boundaries, as shown in Figure 1. The fractures are at the lateral boundaries of the model. The red-colored grid cells refer to oil saturations So=1, whereas the green-colored grid cells mean the oil is depleted So=0. Conventional V-shaped vapor front is replaced by vapor surrounding the still oil-bearing center matrix cells (Fatemi & Bahonar, 2009).

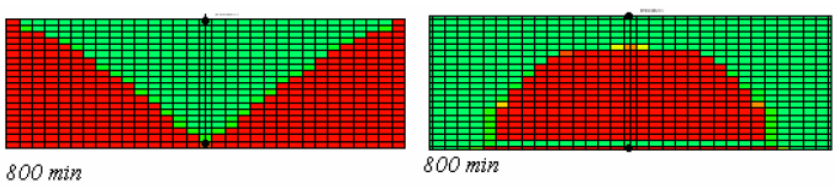

Figure 1: Oil saturation profile for conventional (left) and fractured (right) reservoir model (Fatemi & Bahonar, 2009)

For the Toe-to-Heel Air Injection (THAI) process, the fracture's ability to influence the combustion front stability and temperature was studied. This is of importance because fractures may lead to shortened air/oxygen BT times. In order to stabilize the oxygen front, water is injected to block the pathways for the oxygen through the fractures. For very high fracture permeabilities, oxygen hardly enters the matrix; thus, the average temperature of the reservoir is lowered, and the oil recovery is reduced (Fatemi, et al., 2011).

Fractures also introduce new effects in chemical EOR methods. In the case of a Surfactant Injection, the BT of water through the fracture network is delayed by surfactants due to alteration of wettability conditions from OW/MW to more WW rock. Under more WW conditions, the water is more likely to imbibe the matrix blocks, displacing the oil from the matrix-domain towards the fractures (Cheng, et al., 2018). Another effect introduced by surfactants, especially when combined with polymers in a SP-flood, is that the surfactant may lower the IFT between water and oil, thus lowering the capillary pressure and forcing the system to be more gravity-dominated. This results in more efficient oil recovery and lower residual oil saturation. Similar to already discussed effects, if the fractures are too permeable compared to the matrix, then a BT may occur faster, and oil recovery is decreased, although polymers are

known to mitigate channeling effects due to $K_{fracture}>>K_{matrix}$. Further are, decreased fracture spacing and fractures oriented parallel to the intended fluid flow considered beneficial (SayedAkram & Mamora, 2011). A very well studied area of chemical EOR already at stage of a field application is the utilization of foams in NFRs. Surfactant alternating gas (SAG) in combination with foams dispersed in gas injections lead to an increased treatment depth than SAG alone, and the foams block high permeable fractures. This process increases the potential of inaccessible fractures until then (Ocampo, et al., 2018; Ocampo, et al., 2020).

2.2 Types of Fractures

For practical applications, it is important to detect and characterize fractures, and this is done regularly. Methods to evaluate fractures can be core sample analysis, observing image logs, and conducting studies on the stress regime to find constraints (Khelifa, et al., 2014). Especially the use of image logs established as a stable method in the field. It uses images of fractures as input, and automated algorithms capture the intersections of the fractures and convert them into a Discrete Fracture Network (DFN). However, the huge variety of naturally occurring fractures and their properties represent a big difficulty. Fracture properties of importance could, e.g., be fracture length, which varies in magnitudes from cm-scale to km scale. Fracture orientations are complicated and always depend on the local stress regime in the rocks; fracture apertures and spatial densities are also widely spread over a range of variations. To cover all these variations and complexities, specialized software can be used to create fracture networks (Zuo, et al., 2019). Therefore, coping with mother nature's ingenuity makes sense to group fractures into certain types.

The most natural classification of fractures is distinguishing between natural fractures (NF) and artificially created hydraulic fractures (HF). One big difference is that hydraulic fractures require, in many cases, proppants in order to remain open. Further classification of HF into primary and secondary fractures was conducted in the past in order to study the effects of HF on the productivity index (PI) (Wang, et al., 2019). Although HF and NF share many common features and especially properties of importance on fluid flow, such as fracture length, aperture, conductivity, and network shape (Liu, et al., 2018; Jiang, et al., 2020), the scope of this work lies on NF.

Alternatively, a more general technique to distinguish between fracture types is to separate them into open fractures, partially open and closed fractures. This allows direct comparison between fields with fractures and consolidated fields. Differences in the production, including the faster decline of rates due to fractures and different behavior during secondary recoveries (water or gas injection) because of faster BT times, were reported (Khelifa, et al., 2014).

In many modern simulation studies with naturally fractured rock, single porosity approaches are not feasible. In order to simulate with a single-porosity model a fractured reservoir, the grid cell size would need to be extremely small, which could be reason for extremely intensive CPU requirements (Dershowitz, et al., 2000). Dual porosity and dual permeability models can circumvent such problems, but they must first distinguish between the fractures and the matrix. Parameters for both instances have to be generated, and only in the subsequent step fractures can be separated into more detailed groups, such as primary and secondary fractures (Gilman, et al., 2011). Classification of NF in primary and secondary fractures makes sense because it was found that not all fractures contribute the same amount to the fluid flow. This is especially important when certain fractures only contribute to the fluid flow in a specific production regime. According to that, during the primary production, all the fractures (primary and secondary) were found to contribute positively to the fluid flow, but during the secondary production, suddenly the effect of the secondary fractures diminished (Gong & Rossen, 2016; Gong & Rossen, 2017). To the authors best knowledge, currently, it is not officially regulated how fractures should be classified in simulation. Gong and Rossen classified their fractures into primary, secondary, and tertiary fractures, not based on the fracture conductivity or aperture, but on their significance to contribute to the fluid flow. A simple hypothetical fractured model with primary, secondary, and tertiary fractures was used in their work. The primary fractures contribute most to the fluid flow, and tertiary fractures the least from all studied fractures (Gong & Rossen, 2018).

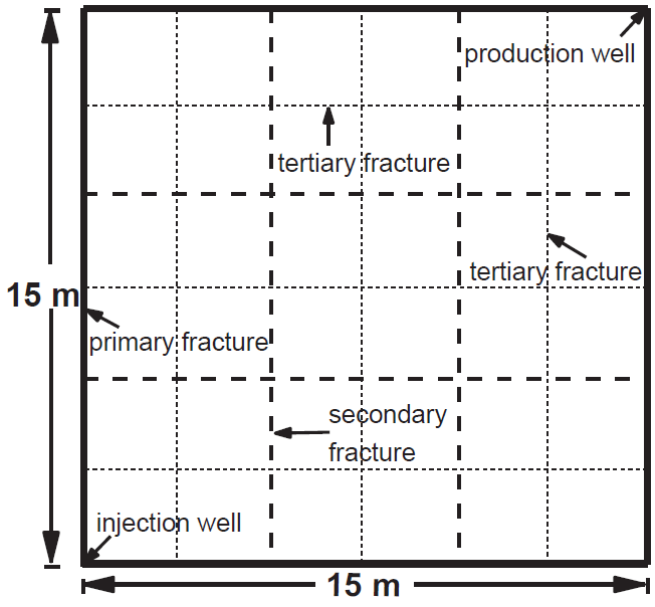

Figure 2: Simple fractured model with primary, secondary, and tertiary fractures (Gong & Rossen, 2018)

Other studies classified open fractures according to their aperture values. Based on Formation Micro-Imager (FMI) and Electrical Micro-Imager (EMI), fractures can be recognized and their aperture estimated using mathematical expression to convert from measured logging parameters to aperture. With aperture and continuity of a fractured network known, classification can be conducted by defining major, medium, and minor fractures. Major fractures are defined as the fracture type with the highest continuity and aperture values. In contrast, the minor fracture type has the lowest values. Medium fractures consist of continuous fractures with aperture values not as high as in the major fractures (Aghli, et al., 2019).

2.3 Dimensionless Numbers

Dimensionless numbers can be defined to study how reservoir (including fracture-) properties influence oil recovery. Such sensitivity analysis allows extraction of information from a simple model and implementation of those findings onto a larger real field application. Also, comparison between different fields is possible due to the physical character of dimensionless numbers (Talluru & WuMewbourne, 2017). An example of a relatively simple dimensionless number often used in reservoir engineering studies is the mobility ratio M. The mobility ratio is defined by the mobility of displacing phase over the mobility of the displaced phase. Displacing phase is often water, which displaces the oil. The mobility λ, in general, is calculated via the simple relationship (Green & Willhite, 1998):

$$\lambda_i = \frac{k_i}{\mu_i} \qquad \text{(Eq 2.3.1)}$$

Where λ represents the Mobility of phase i, with k_i being the permeability of i and μ_i is the viscosity.

However, many other prominent examples of dimensionless numbers which are often used in reservoir engineering exist. It is important to choose from this rich selection of possibilities the right one for each application. The Nusselt number, for instance, describes the ratio of convective to conductive heat transfer, meaning that in respect to a fractured reservoir, its usability is restricted to some thermal EOR applications. The main dimensionless numbers governing the pore-scale fluid flow are the capillary number, the gravity number, and their combination, the bond number. Further important dimensionless numbers often used are the Péclet number, Reynolds number, and the already discussed mobility ratio (Rashid, et al., 2012).

The capillary number and the gravity number are often used dimensionless parameters. They are generally defined as the ratio between viscous- over capillary forces and gravitational over

viscous forces. There are different definitions of these dimensionless numbers published in the literature regarding reservoir parameters used for the calculation (Coll & Muggeridge, 2001; Rostami, et al., 2010). So did AlQuaimi and Rossen publish in 2017 a new definition of the capillary number. They altered the general definition by adding a geometric term, which can be derived from the fracture itself, containing fracture properties such as wall roughness, throat diameters, the distance between two throats, and the contrast between apertures in throats and pore bodies (AlQuaimi & Rossen, 2017). One approach published in the literature is to calculate dimensionless numbers derivated from the material balance. The capillary number is defined as a capillary over viscous force ratio, giving insight into the fluid flow through the matrix. The flow through the fractures is captured by calculation of the gravity number as gravity over viscous force. Eventually, the bond number (gravity over capillary force) can be calculated from there for fractured reservoirs (Zhou, et al., 1993). These equations published in 1990 by Zhou and his colleagues were used multiple times in similar studies in the coming years. Heeremans et al. (2006) conducted studies about the WAG process in fractured reservoirs with capillary and gravity numbers defined as follows:

$$N_{cv,m} = \frac{L\, p_c^*\, k_m\, M}{H^2 \mu_o q_m (1+M)} \qquad \text{(Eq 2.3.2)}$$

$N_{cv,m}$ is the Capillary number, with reservoir length L [m], characteristic traverse capillary pressure pc* [Pa], average matrix permeability k_m [m²], mobility ratio M [-], reservoir thickness H [m], Darcy's flow velocity in the matrix q_m [m/s] and oil viscosity µo [Pa.s]

$$\mathrm{N_{gv,f}} = \frac{\mathrm{L\ g\ k_f\ \Delta\rho\ M}}{\mathrm{H\ \mu_o\ q_f\ (1+M)}} \qquad \text{(Eq 2.3.3)}$$

Where $\mathrm{N_{gv,f}}$ is the Gravity number, g [m/s²] gravitational constant, q_f [m/s] Darcy's flow velocity in the fracture, and Δρ [kg/m³] the density difference between injected fluid and oil. This allowed to conclude that for gravity-dominating conditions (high gravity number), the gas injection part of the WAG performed best. Contrary, for capillary-dominating conditions (high capillary number), the water injection is most efficient. Concluding, the WAG performance overtops simple water-flooding, allowing the gas to displace the oil due to gravity effects and at the same time allowing water to displace oil from the matrix through imbibition (Heeremans, et al., 2006). Zhou's definition of dimensionless numbers was also successfully used to quantify the performance of different EOR methods. By running sensitivity runs with different parameters, dimensionless numbers such as the capillary number and the gravity number can be calculated for each sensitivity case. In combination with the recovery factor of every case, this allows for the collection of scattered data points in a 3D space. The three axes include the capillary number, gravity, and recovery factor in the Z direction. Surface planes in 3D space

can then be interpolated for different EOR methods, allowing direct comparison (Kharrat, et al., 2021).

Reynolds number, Re, was used as an additional parameter for fluid flow simulation through fractured reservoirs. It was found out that under reservoir conditions, the value for Reynolds number was limited up to Re=100, supporting the general conclusion that viscous forces dominate over inertial forces (Sarkar, et al., 2004).

Gong and Rossen (2018) used the Péclet number as a tuning parameter to determine how different fracture types interact with primary and secondary production. They used the general definition of the Péclet number, which states diffusive forces over advective forces in such a way, to express it as a function of fracture aperture and permeability ratio $k_{fracture}/k_{matrix}$. This allows establishing a number of simulations with different Péclet numbers to see how fractures cause different oil and water saturation distribution and pressure behavior in the model (Gong & Rossen, 2018).

Aguilera, 1995 and Singha et al., 2012 published simple mathematical expressions combining fracture aperture and permeability. Although both expressions are not dimensionless, they both give a good approximate impression of how aperture impacts permeability. They are derived from Darcy's equation, and in their simplicity, they resemble the often-used cubic law (Zimmerman & Bodvarsson, 1996). Such simple yet effective expressions make simulations of fractured models easier (Aguilera, 1995; Singha Ray, et al., 2012). The fracture permeability equations of Aguilera and Singha et al. are given in Eq 2.3.4 and Eq 2.3.5, respectively.

$$k_f = 8{,}35 * 10^6 * a^2 \qquad \text{(Eq 2.3.4)}$$

With k_f [darcy] being the fracture permeability and a being the aperture [cm] (Aguilera, 1995).

$$k_f = \frac{a^3}{11{,}76} * 10^6 \qquad \text{(Eq 2.3.5)}$$

In the Singha et al. equation, k_f [darcy] is the fracture permeability and a [mm] the aperture for all apertures in the range of 0,0618744mm<a<39,9288mm (Singha Ray, et al., 2012).

Chapter 3

Methodology

3.1 General Description - Reservoir Simulator

The practical part of this work was conducted in Schlumberger's commercial software platform Petrel E&P. The software covers many possibilities in the exploration and production sector of the modern oil and gas business. Users can interpret seismic data, create geological structures and set up reservoir models. Wells can be inserted and correlated; simulation results can be visualized in plots and 2D/3D visualizations. This wide range of possibilities that Petrel covers is one of the primary drives why many industries worldwide, both in professional and academic environments, are using it (Schlumberger, 2021).

In Figure 3, the general workflow of a reservoir simulation is depicted. Modern commercial reservoir simulators provide modules, which generally can be characterized by three main components: pre-processor, processor, and post-processor (Franchi, 2006). The first part of a simulation process usually creates the static geological model, which is usually handled by the pre-processing unit in commercial software. This step involves seismic interpretation, generation of petrophysical properties, and creation of a geological model with eventual heterogeneities such as faults and fractures. Loading fluid properties, wells, production facilities, and the gridding of the now completed geological model are also considered tasks of the pre-processor. Petrel is a functional pre-processor and post-processor. Post-processing refers to the visualization of calculated results either in plots or 2D/3D visualizations of the model. The numerical calculation itself is handled by the processor component of a reservoir simulator. In terms of Schlumberger's Petrel E&P platform, this is handled by Schlumberger's simulator Eclipse. A reservoir model in Petrel can have multiple simulation cases. Each simulation case is exported automatically into Eclipse to be numerically calculated and again

imported back into Petrel for further observation of results. Potentially necessary parameter changes in simulation cases, interpretations, and property calibration can all be done in Petrel.

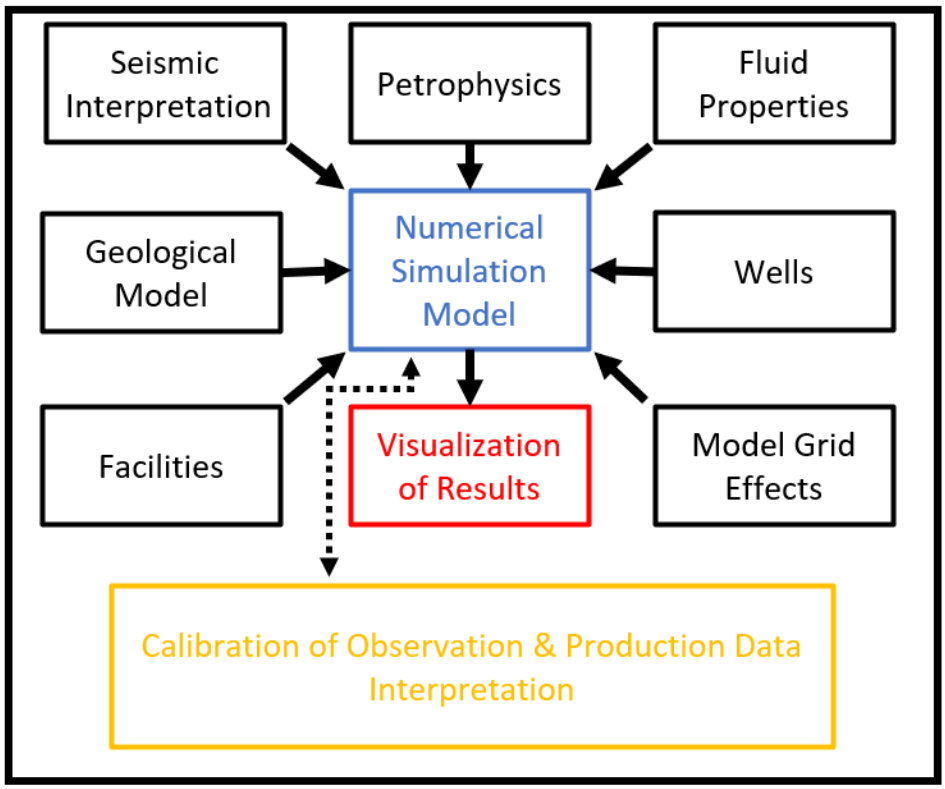

Figure 3: Overall reservoir simulation workflow

3.2 Fractured reservoir model dimensions and gridding

This chapter gives insight into what was generally done to find and verify the real field sector model results. A more detailed discussion of events is conducted in the next chapter of this thesis.

In order to simulate the impact of fractures on production, a reservoir model with different fracture sets is required. This thesis features a sector from the GH field, called the Prototype model. The Prototype model contains real field data, ranging from saturation profiles, fluid model, porosity, permeability, fluids in place, phase contacts, fracture data, and production history. The fracture orientation and properties were obtained from formation image logs and realized in DFN networks into the Prototype model. Fracture classification is conducted based on the aperture of the open fractures. This way, four distinct fracture types were found. The fractures with the highest aperture (and permeability) were referred to as the major fractures, followed by medium, minor, and hairline fractures.

Furthermore, simpler, synthetic reservoir models were created to verify the results of the Prototype model, which contains the real field data. These synthetic models were first created as 2D slices in the horizontal and vertical direction. The lessons learned from these 2D slices were then combined into a 3D cube which was then further studied to verify the effects of the Prototype model. All synthetic models use the same saturation function and fluid model as the Prototype model, but they have simpler representations of fractures. Instead of naturally dispersed and highly heterogeneously distributed fractures, the synthetic model uses deterministically set up fractures in three occurring types. The classification of fracture types again is based on aperture, and the three types were called the major, medium, and minor fractures. In Figure 4, the deterministically distributed fractures used in the 2D synthetic models are shown in three colors. Each color can represent one certain fracture type. Multiple runs were conducted to study the effects of different fracture type distributions. The “standard fracture distribution” used in most simulation cases, if not declared differently, is the following: black fractures (a) used as major fractures, red fractures (b) as medium fractures, and green fractures (c) as minor fractures. The 3D synthetic model generally uses the same fracture distribution scheme but with an increased number of fractures due to its “thickness” into the third dimension. The 3D model has six black fractures (a) instead of four, also six red fractures (b) instead of four, and nine green fractures (c) instead of six. As shown in Table 1, the synthetic model is on a smaller scale than field data. This improves CPU time and general handling with the models. Simulation cases for all synthetic models were conducted with the following fracture sets: only major fractures, major + medium fractures, and major + medium + minor

fractures. In order to generate working simulation grids with symmetrical matrix blocks in between the fractures, a fair number of grid cells had to be found. This is important because, in Petrel, the cell at the fracture location is taken as a dual-permeability cell. Other cells where no fractures are set are considered matrix cells. This forces the user to find a fitting number of cells to honor the symmetrical matrix block size between fracture sets. For example, in the 2D horizontal synthetic model, 67*67 grid cells are taken with all fracture sets (major + medium + minor), the matrix blocks in between the fractures are all 10*10 grid cells in size. If only major + medium fractures are considered in the same model, the matrix blocks are still symmetrically represented by 21x21 grid cells.

Table 1: Synthetic model dimensions

synth. Model	Dimension XYZ	grid cells	grid cell dimension
2D horizontal	15m*15m*1m	67*67*1	0.224m*0.224m*1m
2D vertical	15m*1m*15m	67*1*67	0.224m*1m*0.224m
3D	15m*15m*15m	37*37*37	0.405m*0.405m*0.405m

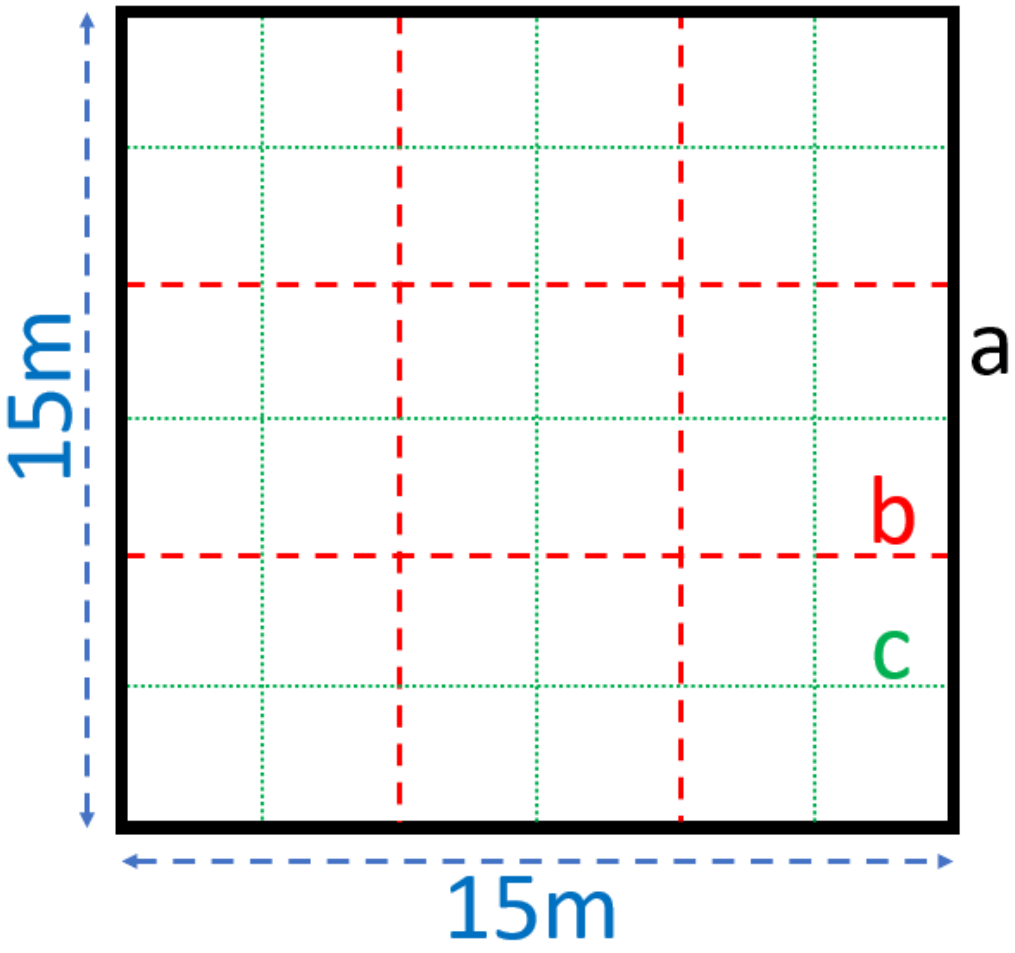

Figure 4: Scheme of the deterministically distributed fractures. (a), (b) and (c) lines can be replaced by each of the fracture types.

The Prototype model consists of 21x 65x 22 grid cells, and its shape is shown in Figure 5. The average grid cell size in the X direction is 865ft; in the Y direction, 568ft, and in the Z direction, 74ft. With the average cell size known, the approximate dimensions of the Prototype can be estimated. The Prototype model is approximately 14km in length (Figure 5 a), 3km in width (b), and 0.5km in thickness (c) large.

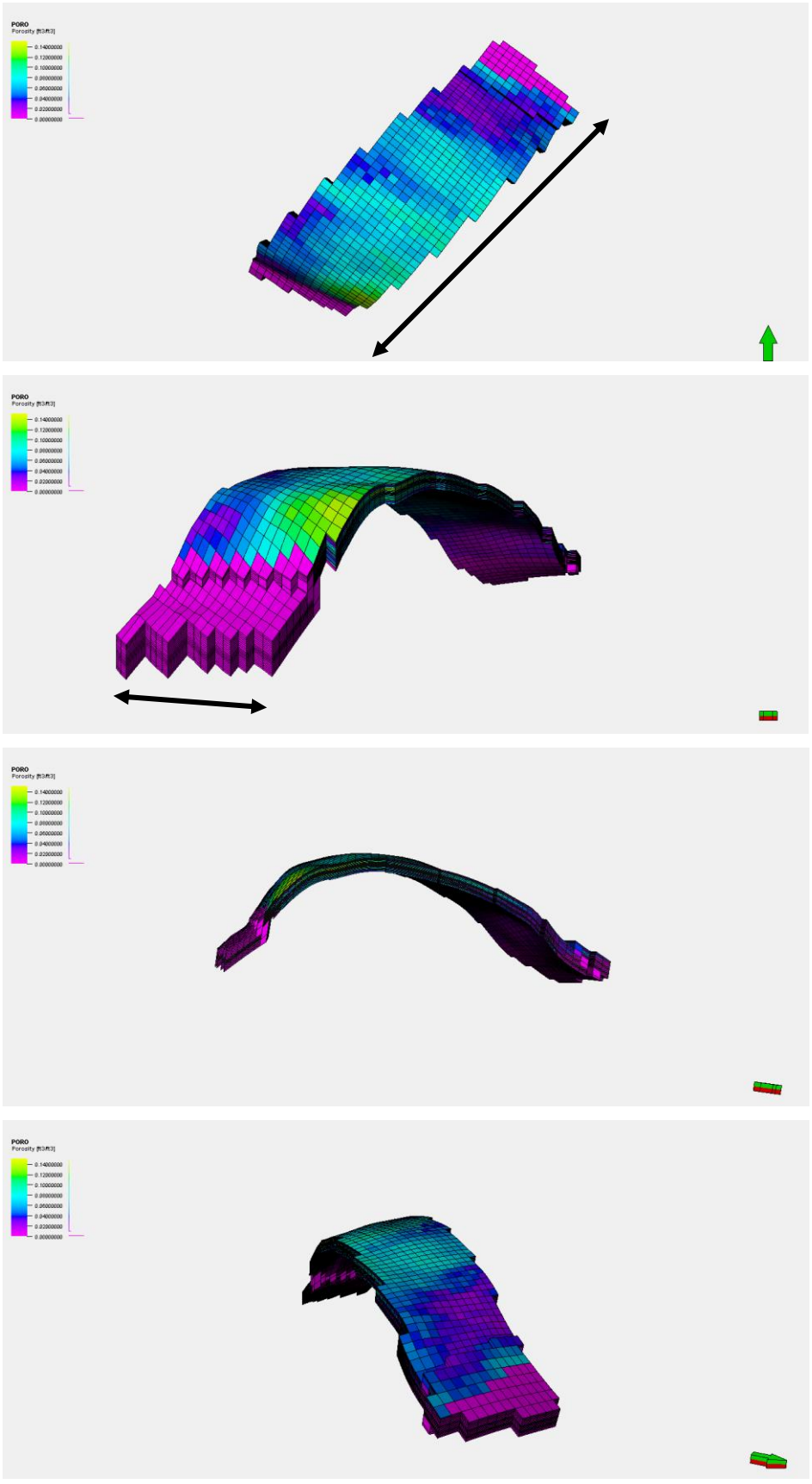

Figure 5: The Prototype model from different angles (a) length 14km (b) width 3km

3.3 Fluid model and rock physics

All reservoir models in this work use the same black oil fluid model in almost all simulation cases. This fluid model was also used in the GH model to history match the whole field. The only exception where a different fluid model was used is in the primary production simulation cases. This step of introducing another synthetic dead oil fluid model was necessary to handle convergence issues due to the fast pressure drop during primary production. The GH fluid model consists of water, oil, and gas, whereas the dead-oil fluid model consists only of water and oil phases. The densities of all phases used are given in Table 2. No region properties were applied over any of the models, meaning that once initial conditions were set for one model, they were constant over this model.

The reservoir top depth for all synthetic models was always considered to be 1000m TVD. The initial reservoir pressure was set in the initial conditions to be 250bar. The reservoir depth of the Prototype model is around 6200ft with an initial pressure of 3630psi.

On the other hand, a region property was used for the saturation functions. Eight saturation functions were applied for the matrix in the Prototype model, four for the drainage relative permeability, and four for the imbibition relative permeability. For the synthetic models, one representative saturation function (saturation function 4) was chosen for the matrix from all the available saturation functions from the Prototype model. The fractures in the synthetic model use the same saturation function as in the Prototype model. Figure 6 shows the representative saturation function for the matrix used in the synthetic models and the Prototype model. The other functions used in the other regions of the Prototype model are included in Appendix A. The fracture relative permeability curves used in all models are shown in Figure 7. The capillary pressure is considered to be zero in the fractures.

Table 2: Phase densities from the fluid model

Fluid model	Phase	Density	Unit
GH	Water	1107	kg/m^3
GH	Gas	0.913	kg/m^3
GH	Oil	855	kg/m^3
Dead Oil	Water	1020	kg/m^3
Dead Oil	Gas	0.811	kg/m^3
Dead Oil	Oil	875	kg/m^3

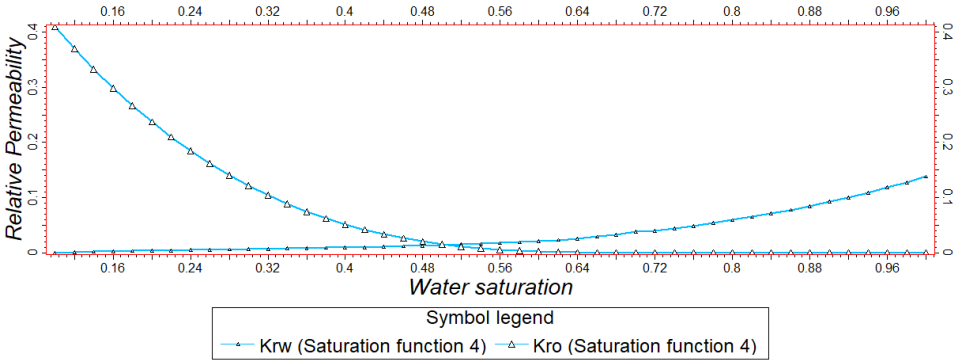

a

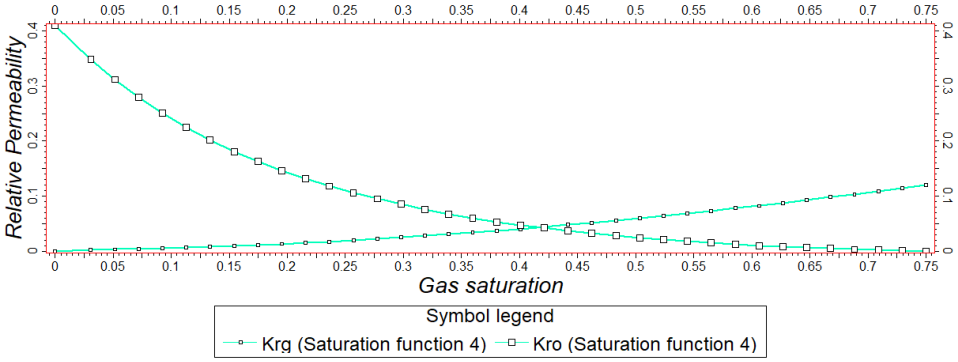

b

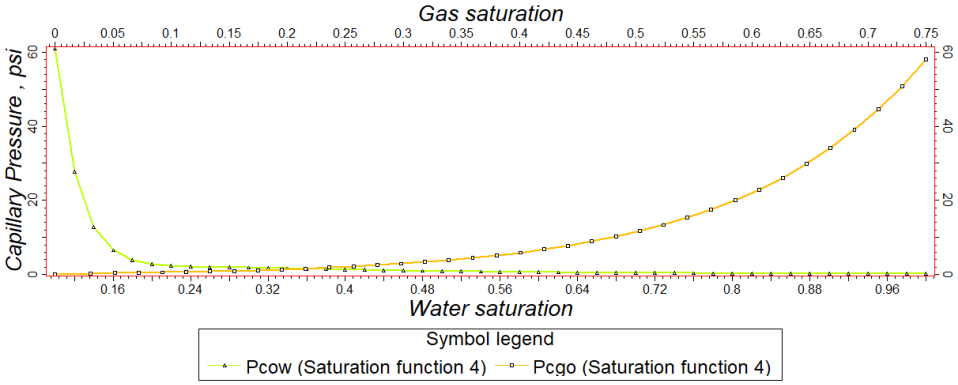

Figure 6: Rock physics: Saturation function 4. (a) oil-water relative permeability (b) gas-oil relative permeability (c) capillary pressures of oil-water contact and gas-oil contact

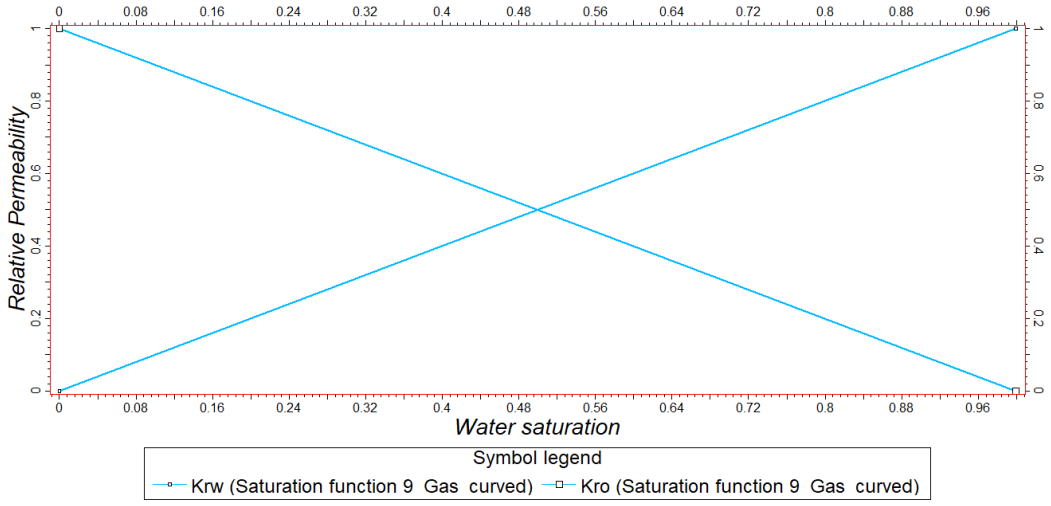

a

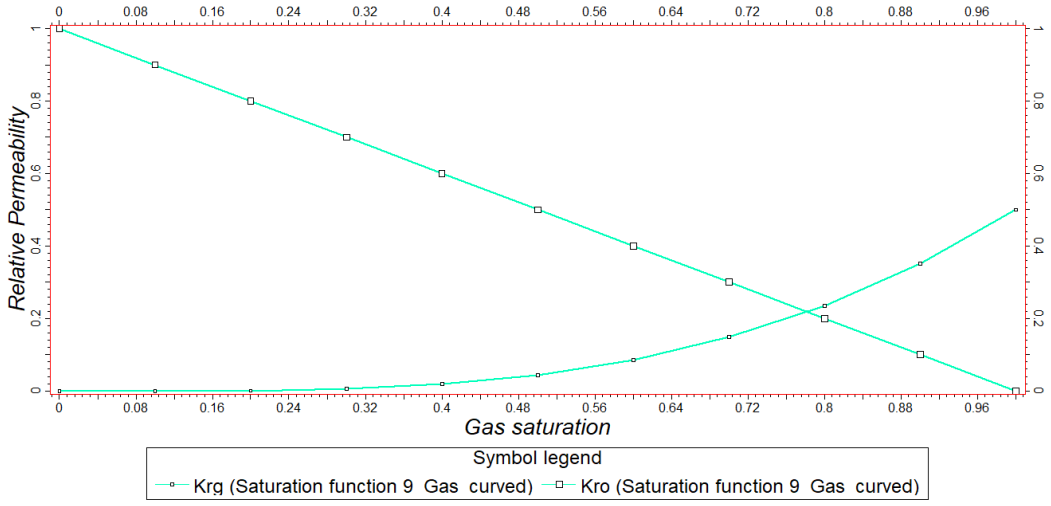

b

Figure 7: Rock physics in the fractures: Saturation function 9 with curved gas relative permeability (a) water-oil relative permeability (b) gas-oil relative permeability

3.4 Development strategy

The method of choice to study the impact of fractures on production over a long period of an oil field's lifecycle is to run simulations designed for primary and secondary production stages. The primary production consists only of the producing well, and no pressure support is included. The secondary production covers waterflooding measures or gas injection. The injecting wells are at the same location and depth for both regimes, waterflooding and gas injection; only the injected phase and the injection rates are changed.

The producers are constrained via pressure production control. This allows setting up a certain pressure limit above bubble point pressure and ensuring to capture the reservoir's potential without restraining any rates manually. The injection rates are different for every model and will be discussed in more detail in the next chapter.

Chapter 4

Results and Discussion

Many different simulations with different production strategies and fracture sets were required to generate the results published in this work. This is the reason why a consistent naming convention was used all across the models. Most simulation cases use the following naming scheme, explained in an example case from the 3D cube: DK_sProd_MajMedMinFr_GD. “DK” indicates that the case runs in dual-permeability mode, alternatively “SP” for single-porosity and “DP” for dual-porosity exist. The second term, “sProd” stands for secondary production. This opposes the abbreviation “pProd”, which stands for primary production. The third term, “MajMedMinFr” indicates that major, medium, and minor fracture types are included into this case. Alternatively, “MajMedFr” refers to a case that considers major + medium fracture types. The abbreviation “MajFr” only includes major fractures. The last term, “GD” in this case, refers to the fact that gravity drainage is enabled to capture the required effects for gas injection for this specific case. These are general statements about the naming convention used. More detailed descriptions are provided within the description for every case.

The Prototype model is designed to handle fractures utilizing Discrete Fracture Networks (DFN). In order to match results from the synthetic model with the Prototype, all the synthetic models were also designed to use DFN’s. It was found that if simulation models using the dual-porosity continuum model, issues arise in combination with DFN’s. If more than one fracture type is used, the connection problems between grid cells representing matrix and fractures occur. A reason for that might be the way Petrel handles dual-continuum modeling such as dual-porosity. This problem was solved by running dual-permeability cases, which allow for a seamless implementation of DFN’s, regardless of the number of fracture sets used.

4.1 2D horizontal slice

The 2D horizontal slice model is the first synthetic model created. It aims to match the results published by Gong and Rossen (Gong & Rossen, 2018). Figure 8 shows the permeability in the Z direction and the location of the wells. This model was primarily used as the initial model to test fractures' impact on primary production and waterflooding.

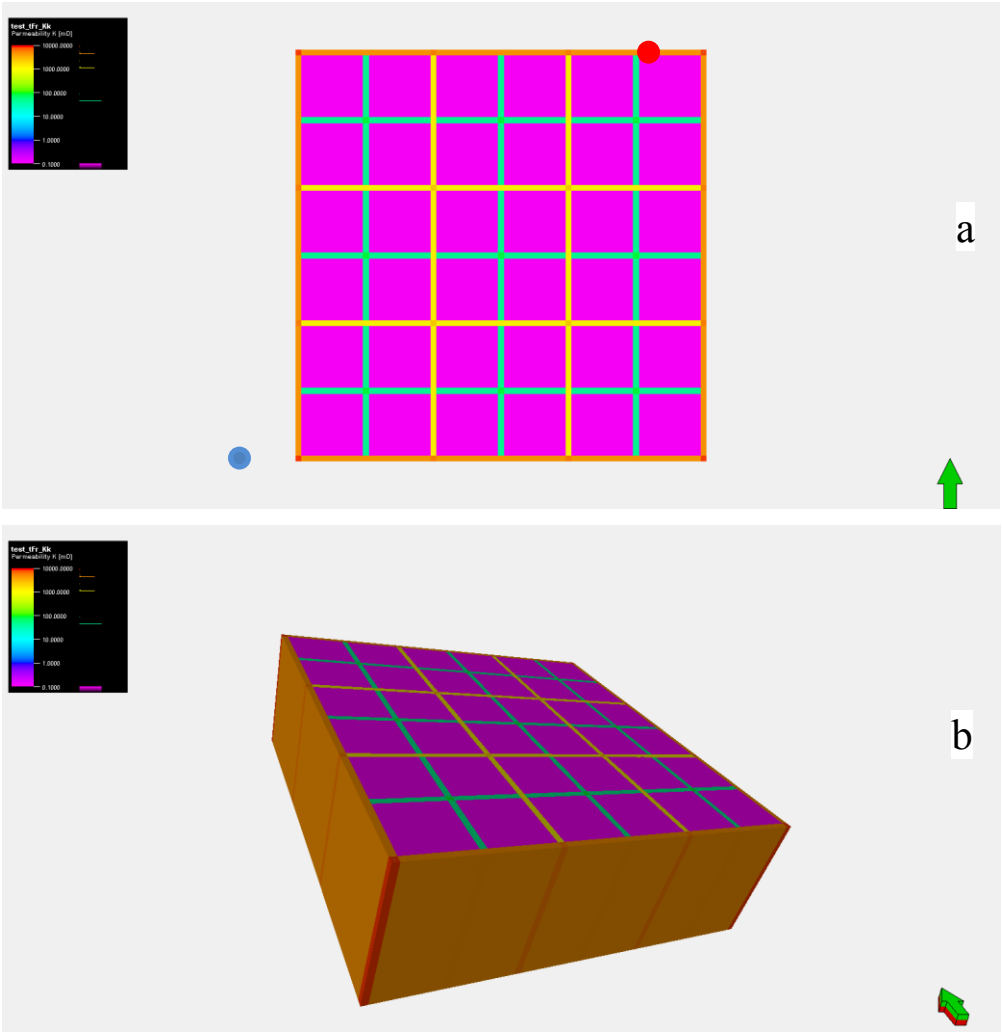

Figure 8: 2D horizontal slice with its permeability in the Z direction (a) injecting well in the left bottom corner (blue dot) and producing well in the right upper corner (red dot)

4.1.1 Primary production

The 2D synthetic horizontal model uses properties presented in Table 3. This model is designed to match Gong and Rossen's (Gong & Rossen, 2018) results based on their estimation of the Peclet number.

Table 3: 2D horizontal primary production parameters

model	2D horizontal	
dimension XZY	15x15x1	m
cell count XYZ	67x67x1	
recovery process	primary production	
SCAL	GH	
fluid model	Dead Oil	
injection rate	-	m^3/day
producer BHP	10	bar
well orientation	vertical	
production period	1	year

The grid properties used in order to get results for Pe=1000 are shown in Table 4. The fracture properties such as porosity, permeability, and the shape factor sigma are generated by upscaling the DFN. The DFN is created with an aperture of the major fractures of 1mm, 0.5mm for the medium fractures, and 0.1mm for the minor fractures. These properties were used for every other synthetic model in this work, if not stated differently.

Table 4: 2D horizontal slice grid properties for primary production

Property	**Value**	**Unit**
Porosity	20	%
Permeability	0.000375	mD
Major fracture porosity	0.45	%
Medium fracture porosity	0.22	%
Minor fracture porosity	0.04	%
Major fracture permeability	4.5	D
Medium fracture permeability	1.1	D
Minor fracture permeability	0.044	D
Shape factor sigma	80	$1/m^2$

Based on the deterministically distributed fractures showed in Figure 4, the following results were conducted with fractures (a) being the major fractures, (b) the medium fractures, and (c) the minor fractures.

This model uses a vertical producer well with a bottom hole pressure limit of 10bar, which is slightly over the bubble point pressure of the Dead Oil fluid model. Due to the dimensionless Peclet number published in Gong and Rossen's work (Gong & Rossen, 2018), this model has an extremely low matrix permeability of 0.000375md. This low value is required to tune the model for Peclet number of 1000 to compare with their published work directly.

The influence of each fracture type can be studied once their recoveries are put together into one plot. Figure 9, Figure 10, Figure 11, and Figure 12 represent these results. As expected, the more fractures are introduced, the better the oil recovery turned out to be and the faster the pressure dropped in the reservoir model. Fractures enhance production significantly. An increase in oil recovery of 42% could be observed if medium and major fractures are considered together compared to major fractures alone. A further increase of 13% in oil recovery could be observed if major, medium, and minor fractures are considered compared to only major and medium. This indicates that medium fractures comprehend more to the oil production than minor fractures. To prove the general importance of fractures, another case was run that had no fractures at all; Figure 9 called the SP_PPROD_BASE_CASE. Without any fractures introduced, this BASE_CASE resembles the pure matrix governed production. The result shows how much fractures contribute to oil production in this model because the fracture-less BASE_CASE produced approximately 3% of the oil produced with the major fracture case.

The pressure drop is as expected corresponding to the observed recovery efficiency, showing for the case with all the fractures the highest pressure drops, as shown in Figure 13.

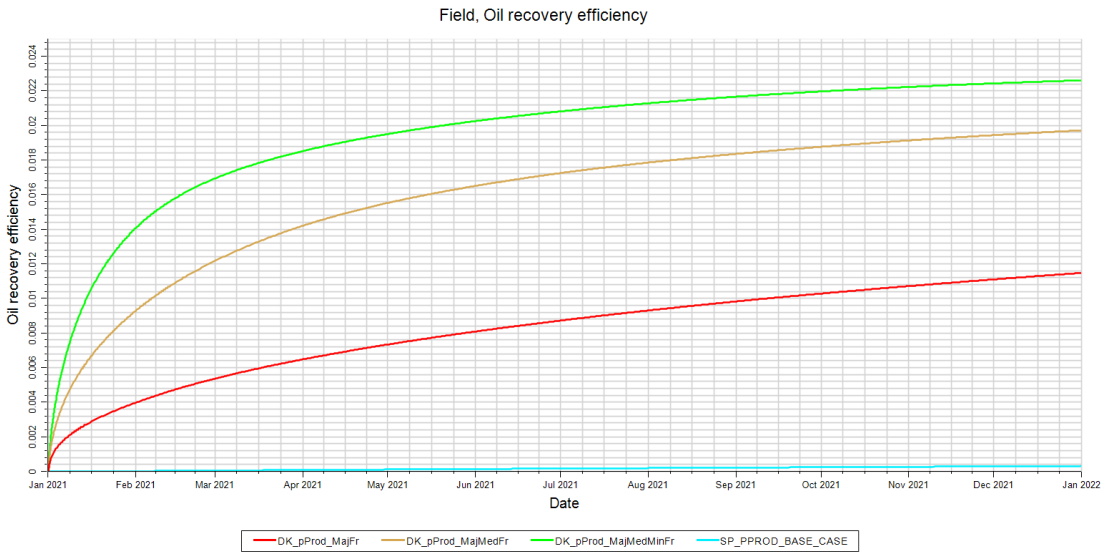

Figure 9: Primary production for all fracture types.

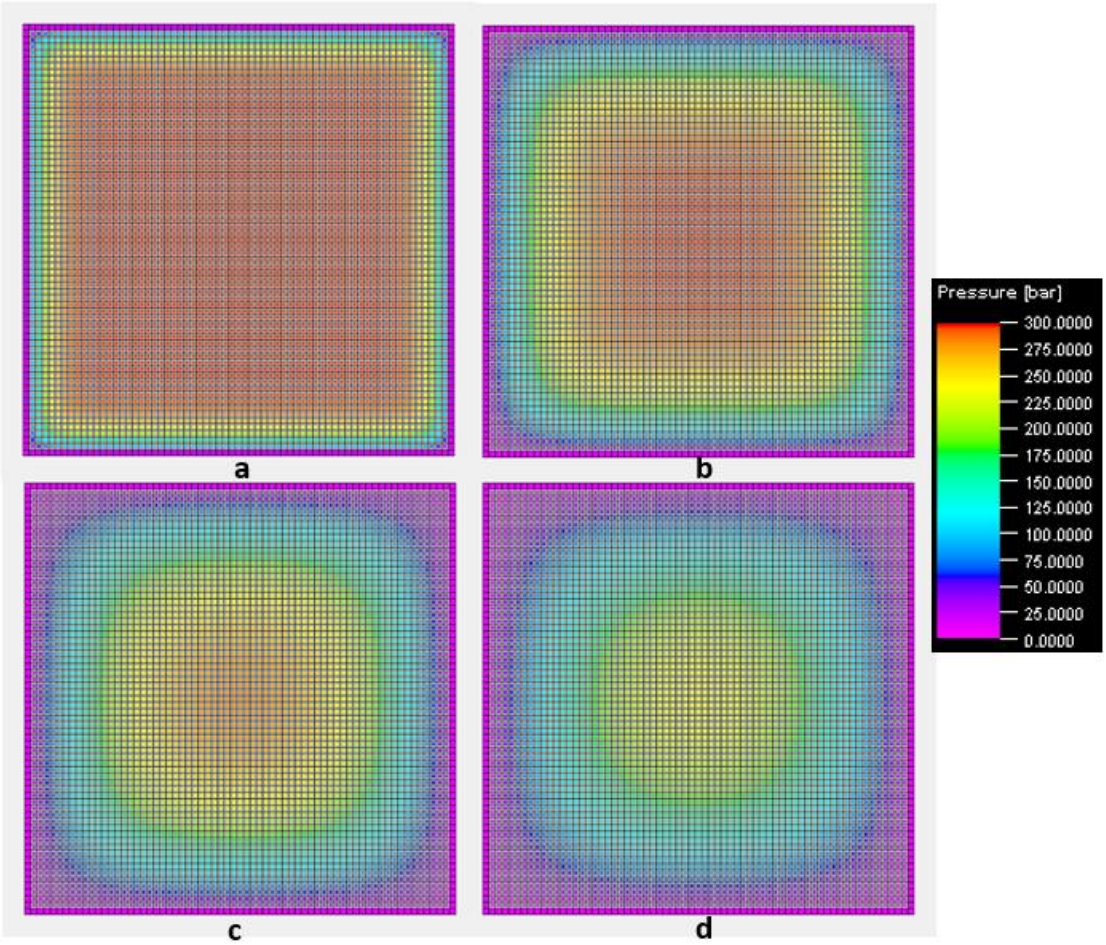

Figure 10: Pressure distribution for primary production for major fractures after a) 14 days b) 4 months c) 8 months d) 12 months

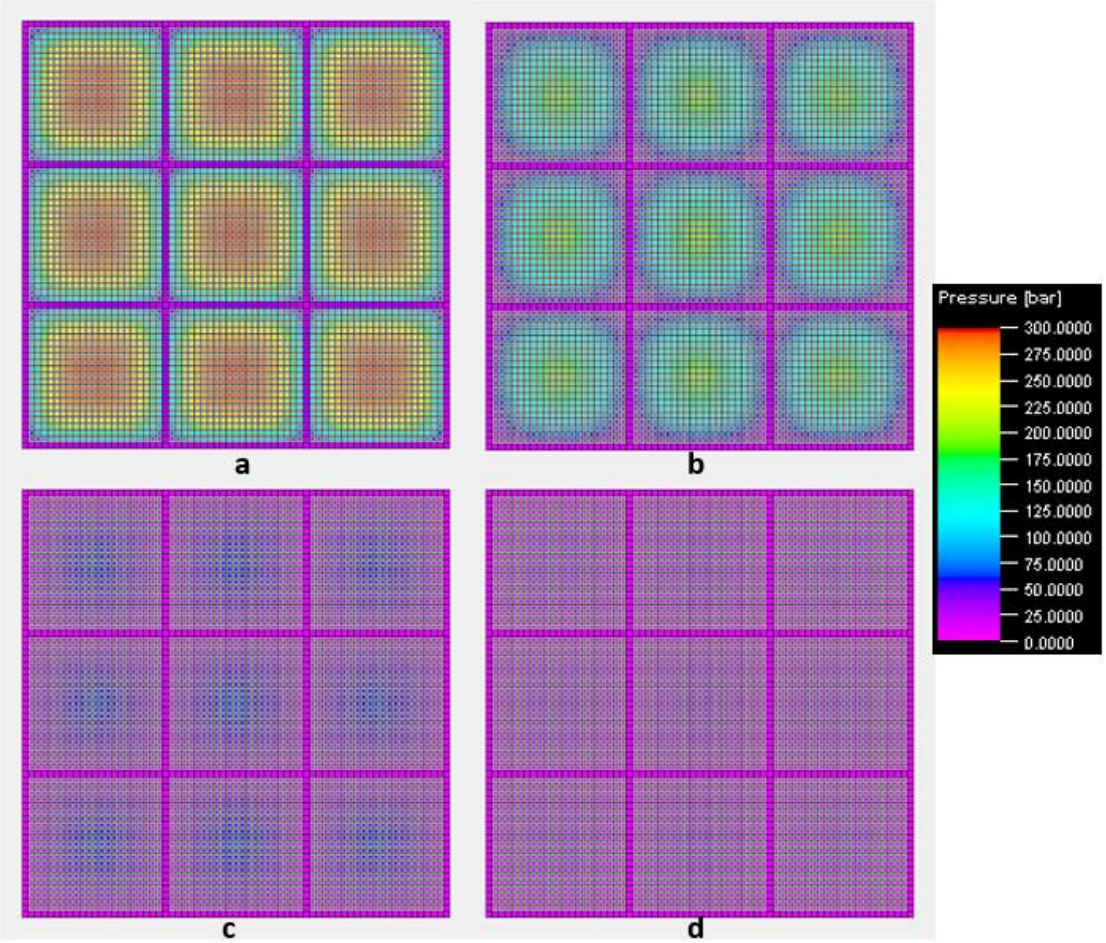

Figure 11: Pressure distribution for primary production for major and medium fractures after a) 14 days b) 3 months c) 6 months d) 9 months.

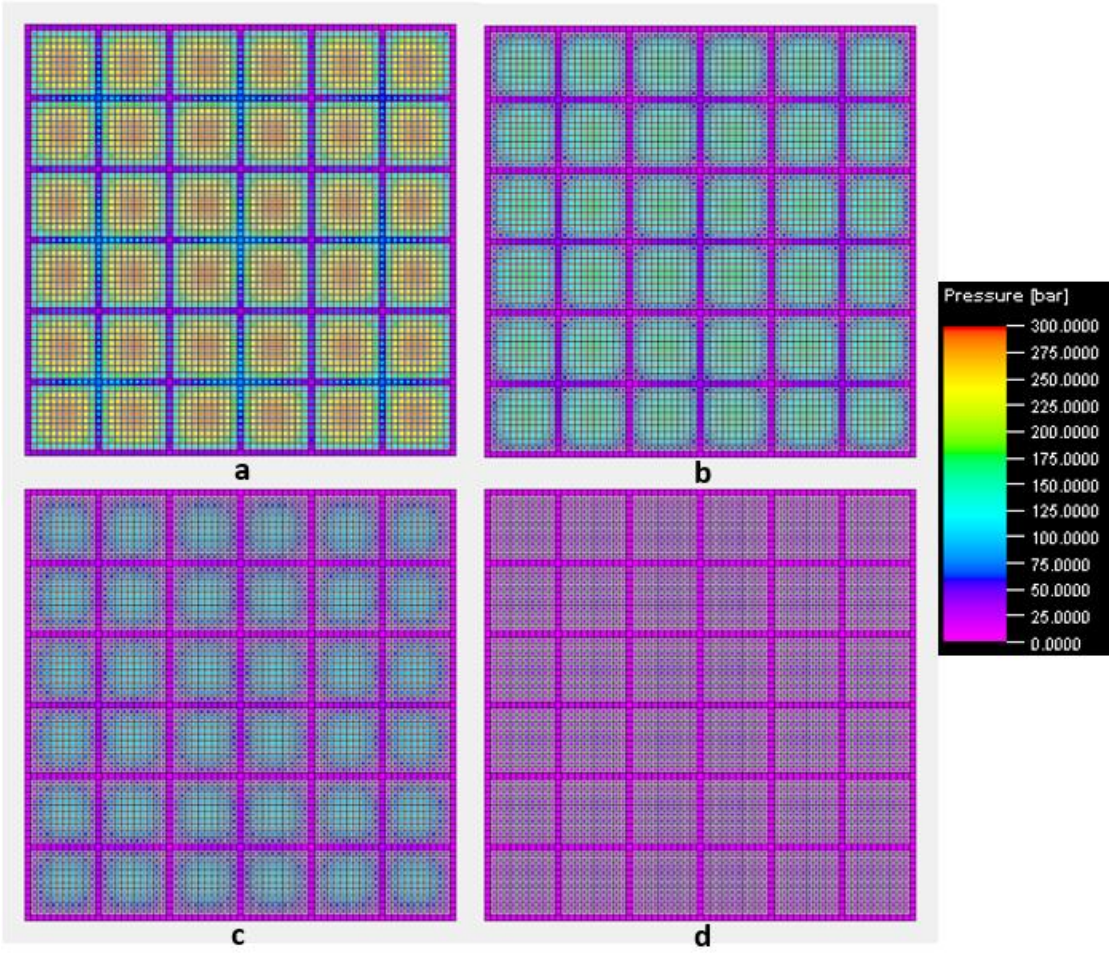

Figure 12: Pressure distribution for primary production for major, medium, and minor fractures after a) 7 days b) 21 days c) 2 months d) 3 months.

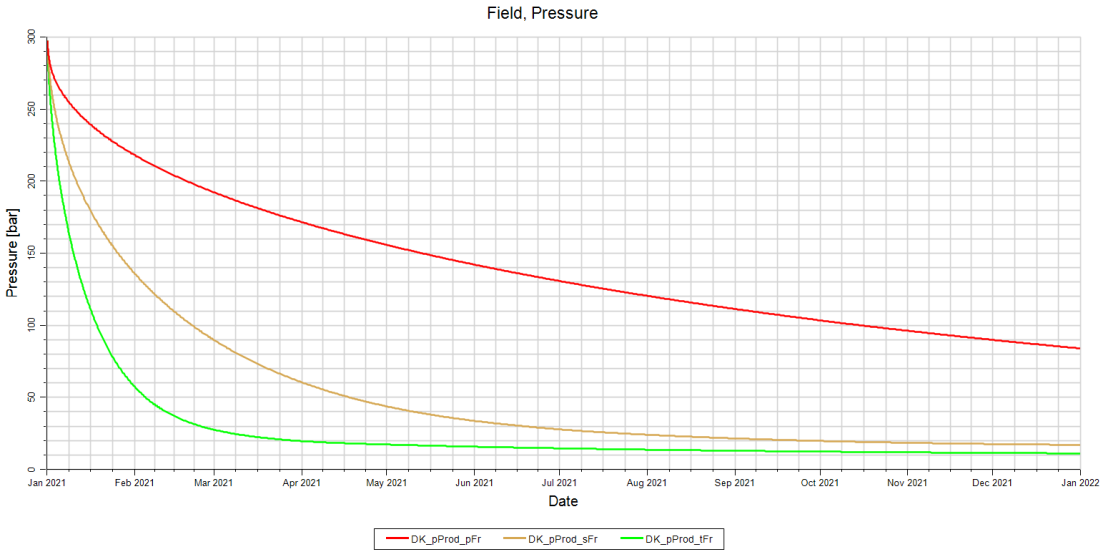

Figure 13: Pressure drop during primary production in the 2D horizontal slice

The observation that fractures can enhance oil recovery is known for many decades already in the literature (Saidi, 1987; Golf-Racht, 1982; another step has to be concluded to ensure that the published results are valid. All cases so far and most cases in this work are conducted under the dual-porosity and dual-permeability regime. To ensure that the results published so far for the 2D horizontal model are valid and not the result of some simulation error, the same model with the same cases was run under a single porosity regime. A direct comparison between dual-permeability and single porosity was not made, but the general trend and especially the impact of each fracture type can be verified. As shown in Figure 14, the major and medium fractures increased the oil production by 42% compared to the major fractures alone. This is exactly the same increase in production as was already discussed in the dual-permeability cases. The introduction of minor fractures brought a similar increase in the single porosity cases and the dual porosity. 18% oil recovery increase for the major, medium, and minor fractures compared to the major and medium fracture cases. That is not the same result as observed for the dual-permeability, but close enough to prove the validity of the simulation run. The future models, especially the cases in the 3D cube, will be conducted in the dual-porosity and dual-permeability regime.

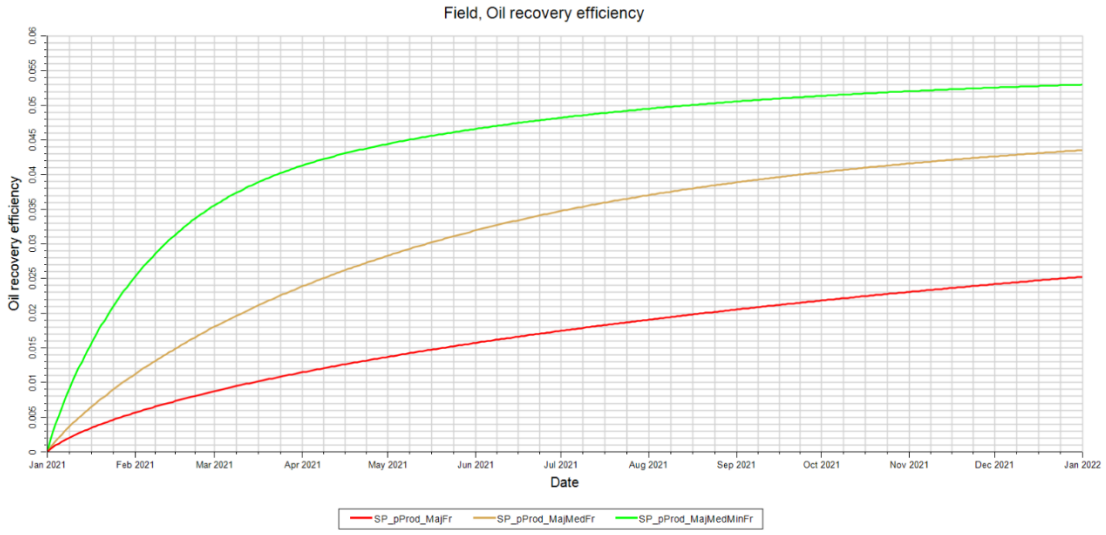

Figure 14: Single porosity runs for primary production in the 2D horizontal slice

4.1.2 Secondary production - Waterflooding

The secondary production period in the 2D horizontal slice was studied based on a waterflooding scheme. The location of the wells is the same as shown in Figure 8 (a); wells are cased over the whole length and perforated over the whole reservoir. The injector injects water with a constant rate of 0.24m^3/day, which equals approximately two pore volumes over a period of one year. The producer is once more only pressure constrained, with a minimum bottom-

hole pressure of 100bar. Other parameters used are shown in Table 5 and the grid properties used are presented in Table 6.

Table 5: 2D horizontal waterflooding parameters

model	2D horizontal	
dimension XZY	15x15x1	m
cell count XYZ	67x67x1	
recovery process	waterflooding	
SCAL	GH	
fluid model	GH	
injection rate	0.24	m^3/day
producer BHP	100	bar
well orientation	vertical	
production period	1	year

Table 6: 2D horizontal slice grid properties for secondary production

Property	**Value**	**Unit**
Porosity	20	%
Permeability	1	mD
Major fracture porosity	0.45	%
Medium fracture porosity	0.22	%
Minor fracture porosity	0.04	%
Major fracture permeability	4.5	D
Medium fracture permeability	1.1	D
Minor fracture permeability	0.044	D
Shape factor sigma	80	$1/m^2$

As can be seen in Figure 15, the first observation is that the trend is more complex than previous simulation results. Two trends appear; it is believed that this result is related to the production behavior of such a system where the oil is drained first from fractures faster, and then it starts to be drained from the matrix. Further investigation is needed to confirm this thesis with the 3D cube and wettability sensitivity. Another observation that can be noted from this result is that the type of fracture network impacts recovery in the early period. Almost all the fractures networks performed similarly, but the major only fractures network performed the worst at later

times. No difference between the two other major + medium and major + medium + minor fractures networks indicates that minor fractures hardly contribute to the recovery.

Regarding the pressure response, as shown in Figure 16, severe decline at early times related to the fast production from fractures after that, the pressure remains constant, indicating a matrix governed flow is occurring. Moreover, the water cut behavior correlates with other plots confirming the physical mechanism happening in such a production scheme (imbibition). Especially with the high spike in the beginning because of fractures production, and after that, the water cut dropped as the matrix-based flow got more activated (Figure 17).

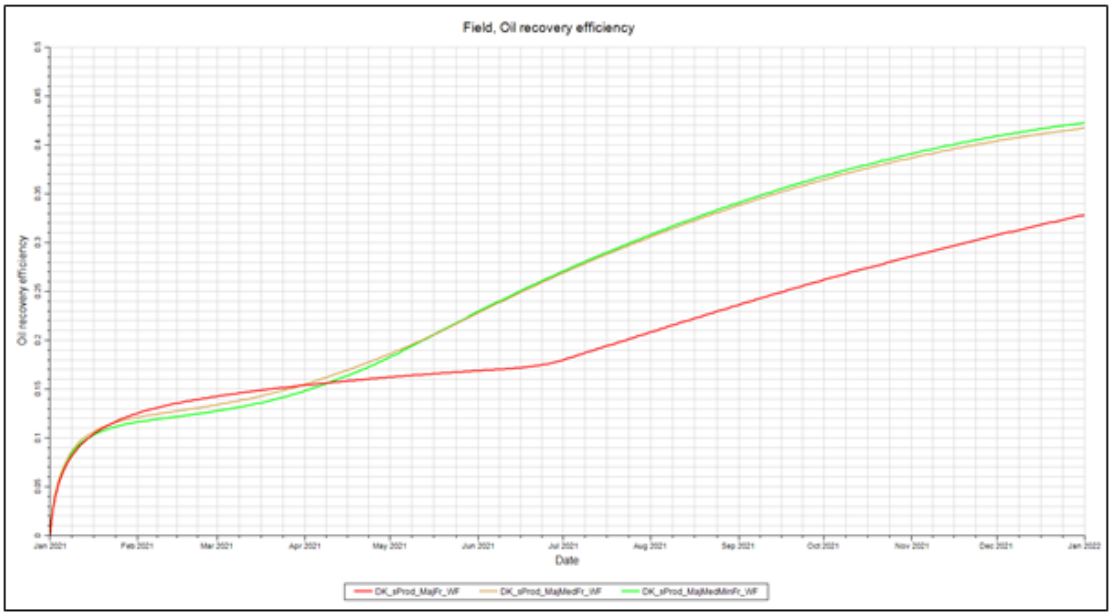

Figure 15: Waterflooding in the 2D horizontal slice

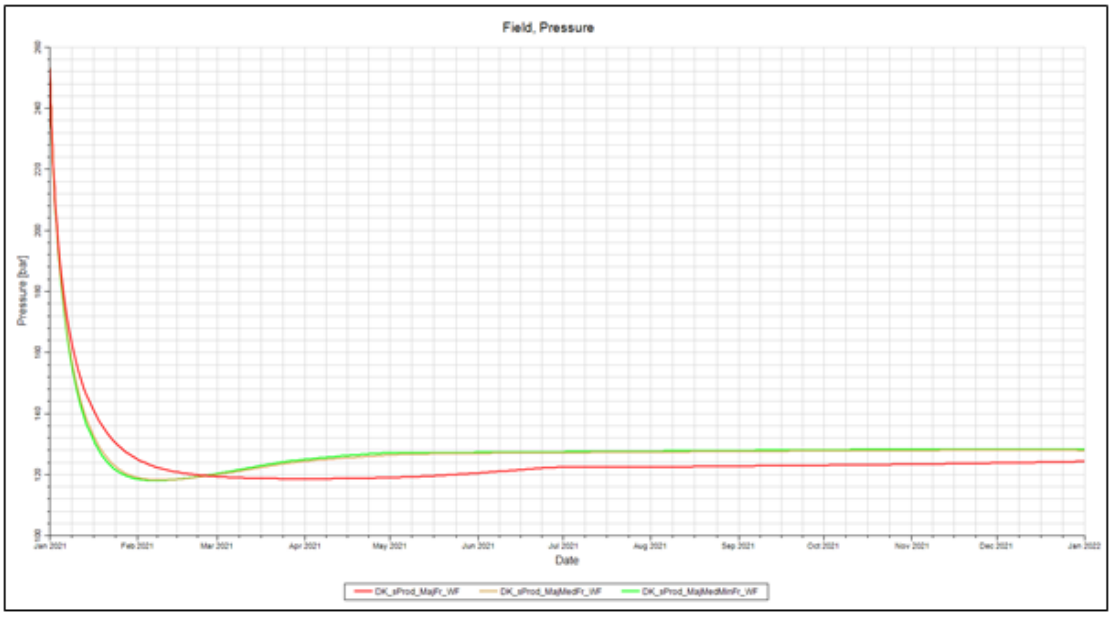

Figure 16: Pressure drop in 2D horizontal slice with water injection

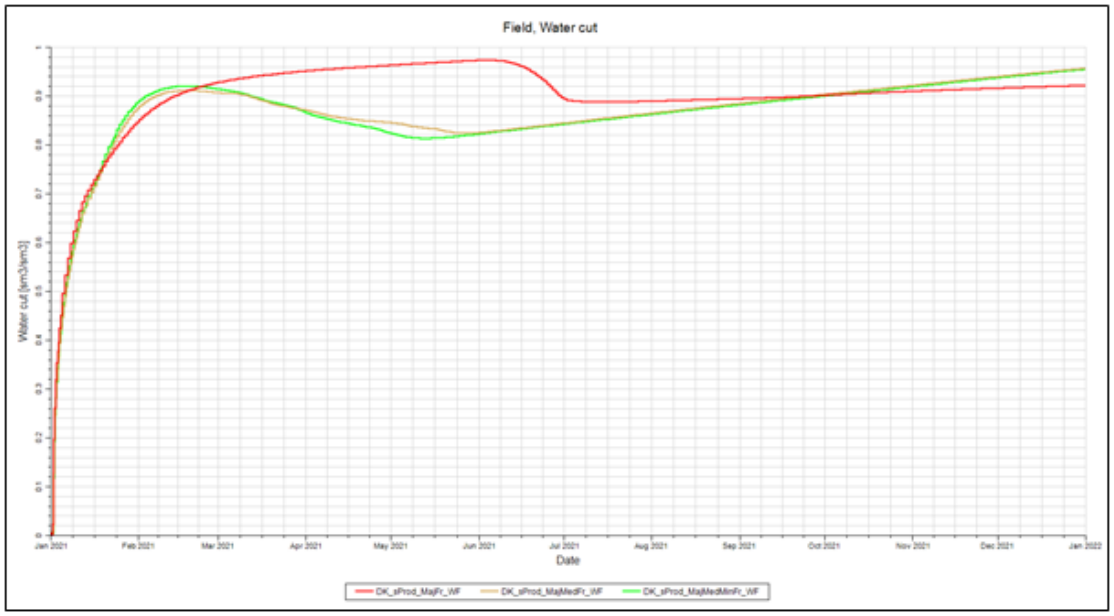

Figure 17: Water Cut for the secondary production (Water flooding)

Saturation profiles are shown in Figure 18, Figure 19, and Figure 20 at two different time steps to visualize how the front advances for different combinations of fracture types. The obtained results match with the published results by Gong and Rossen (Gong & Rossen, 2018). Fractures contribution can easily be seen. All these cases were conducted for one year of simulation time to prove that longer run times do not introduce any changes; runs with extended periods of several years were run. No changes in trends could be observed from that.

Due to the reason that a 2D horizontal model cannot represent gravity effects, the gas injection was not studied in this model but the 2D vertical.

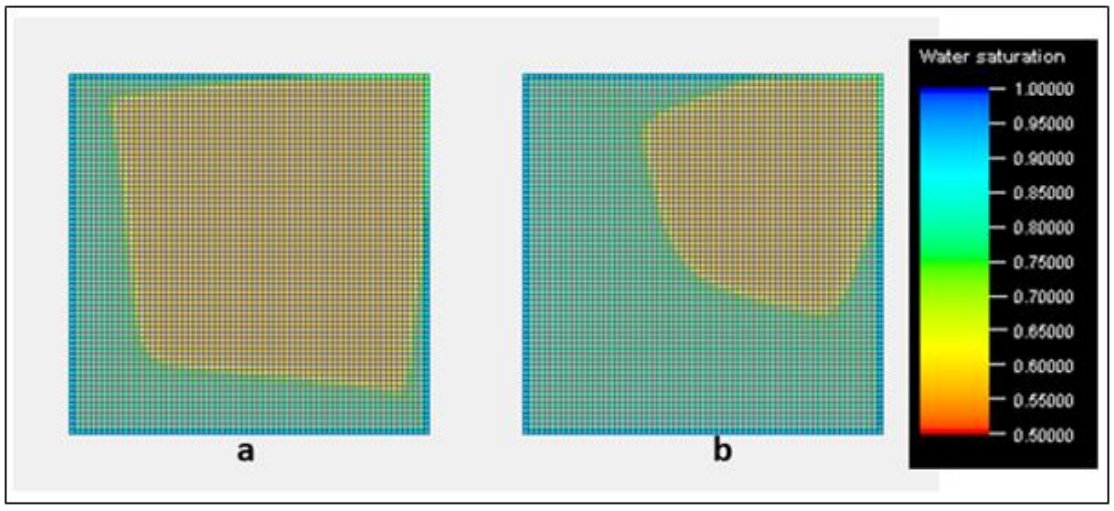

Figure 18: Water saturation distribution for the case with major fractures after a) 3 months b) 9months

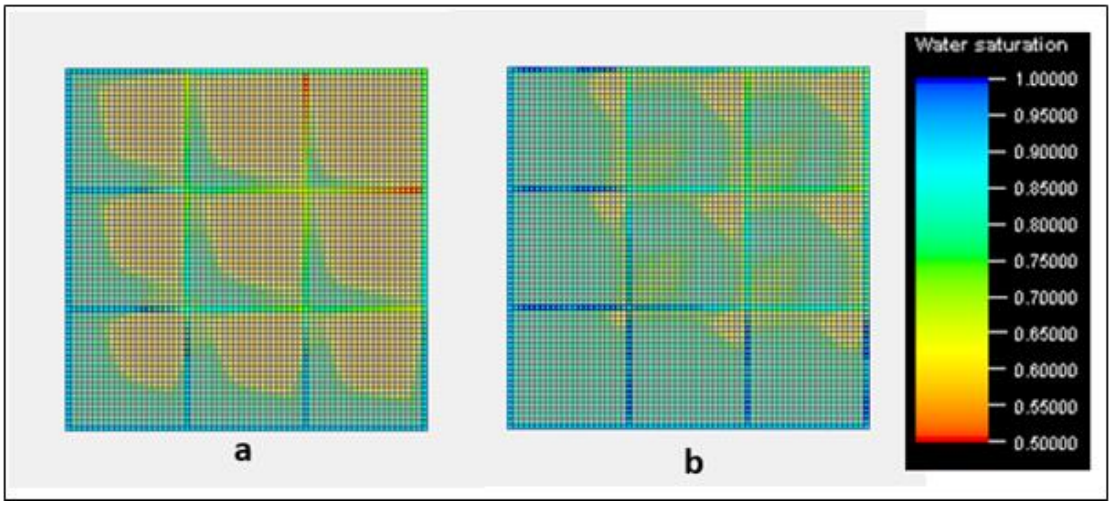

Figure 19: Water saturation distribution for the case with major and medium fractures after a) 3 months b) 9months

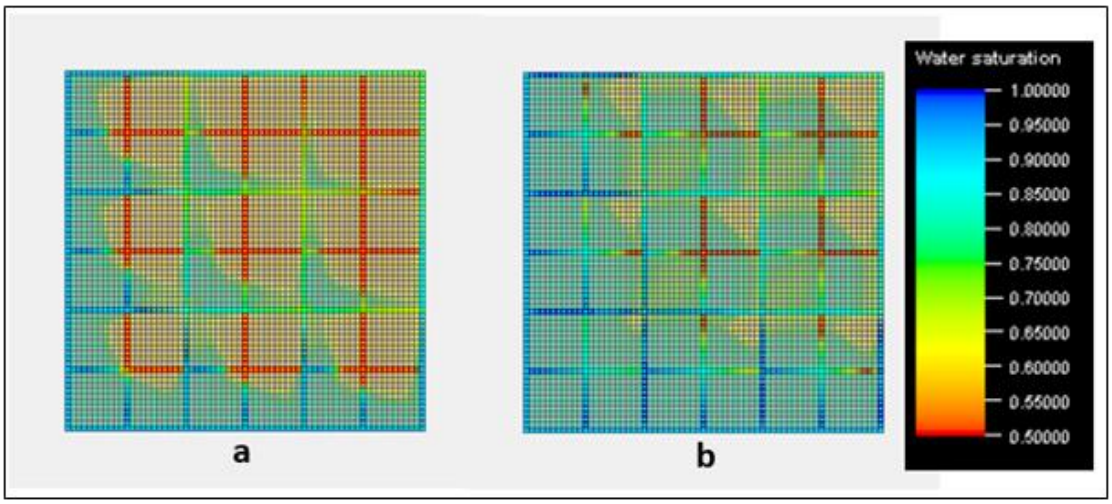

Figure 20: Water saturation distribution for the case with major, medium, and minor fractures after a) 3 months b) 9months

4.2 2D vertical slice

The 2D vertical slice is geometrically the same model as the 2D horizontal slice, only 90 degrees rotated over the Y-axis. It was used to match the work published by Gong and Rossen (Gong & Rossen, 2018) for the primary recovery and to study the effects of gas injection for the secondary recovery. The results from the gas injection process were used to verify the approach for the 3D cube model.

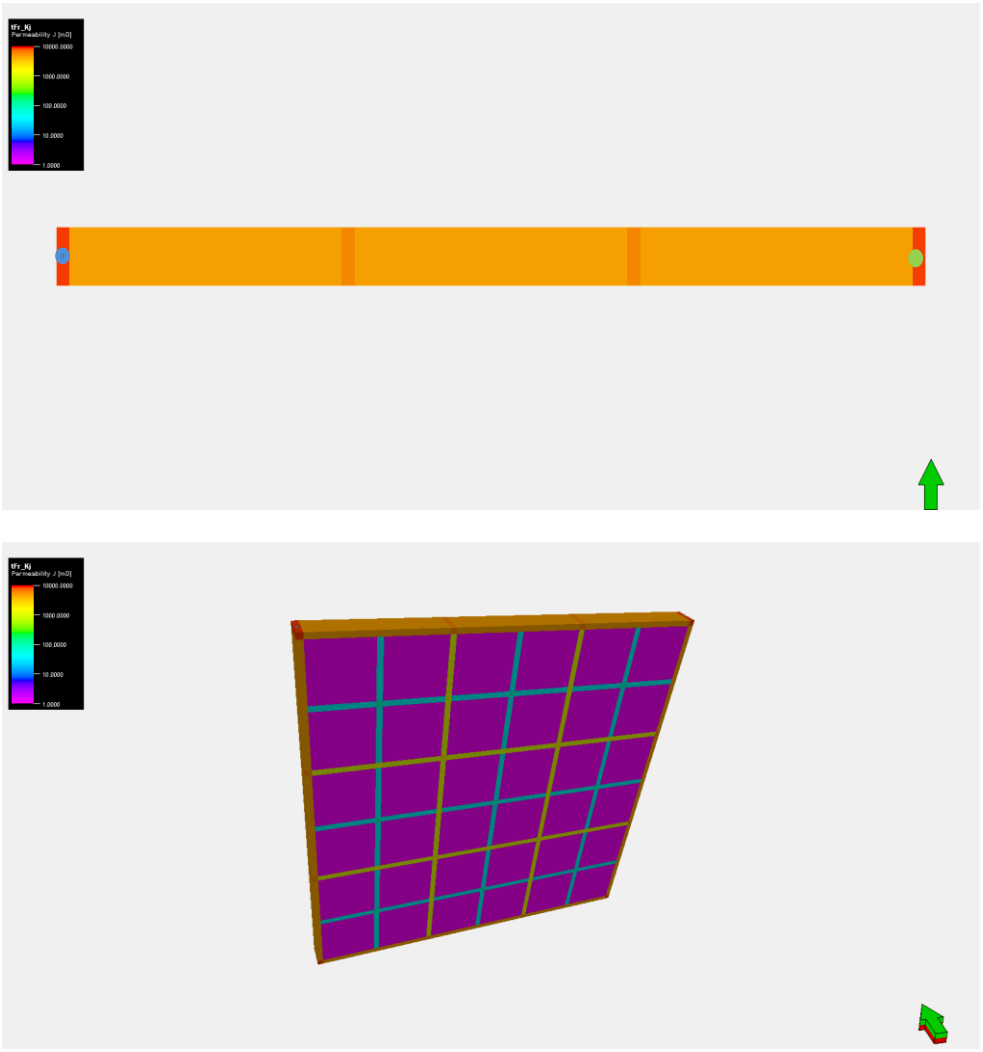

Figure 21: 2D vertical slice model (a) left blue dot represents injector and right green dot producer

4.2.1 Primary production

For the primary recovery, the vertical producer shown in Figure 21 (a) has been used. The properties used for the simulation are the same model as the 2D horizontal slice. The 2D vertical slice is also tuned for Peclet number 1000. The results for the primary recovery are shown in Figure 22. The observed trend is similar to the already discussed results from the 2D horizontal. Slightly higher ultimate recovery could be reached for the vertical domain than for the horizontal. That might be because, in the vertical slice, the well has more contact with the reservoir than the horizontal slice. The single porosity base case is by far the least effective simulation case. Including the major fractures alone brought a recovery increase of 77%. By adding medium fractures again, recovery efficiency could be doubled up to 4.6% of oil recovery efficiency. Minor fractures also increase recovery, but as observed with all 2D model, slightly

less than the medium fractures. Analog to the recovery efficiency curves, the pressure response illustrated in Figure 23 shows the highest pressure drop for the case with all three fracture types combined.

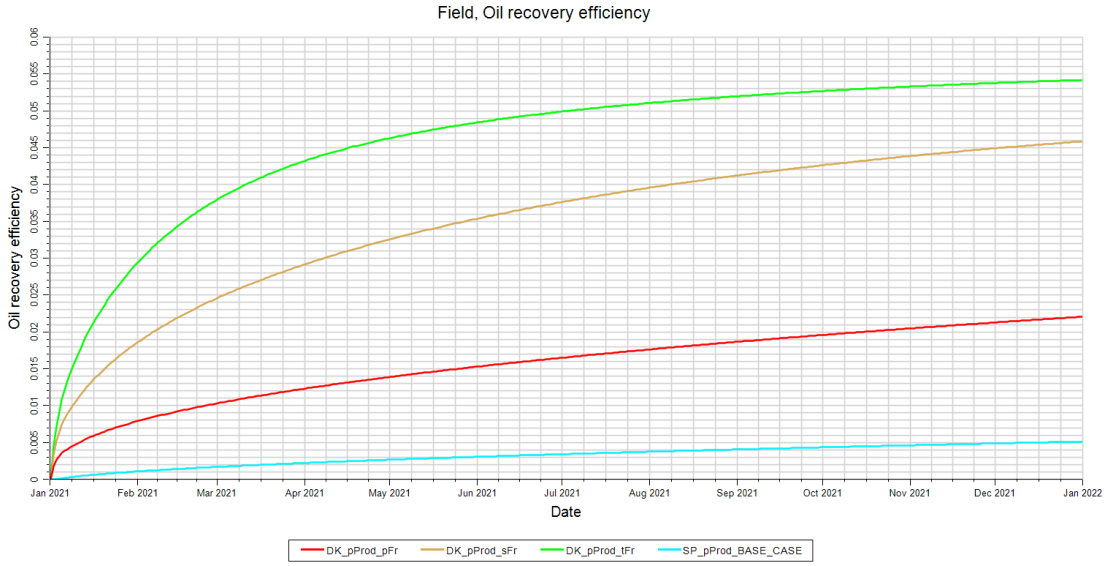

Figure 22: 2D vertical slice primary production comparison

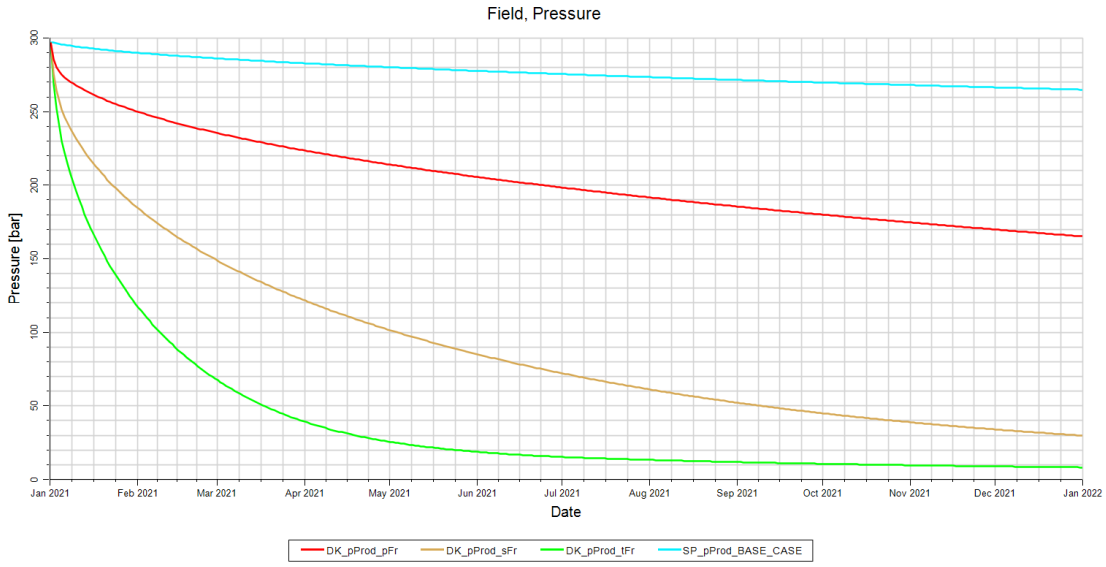

Figure 23: Pressure drop for the 2D vertical slice during primary recovery

4.2.2 Secondary production – Gas injection

Two additional horizontal wells were placed into the model to observe better gravity-related effects and the impact of fractures on gas injection. The two horizontal wells are cased over the whole length and perforated over the length in contact with the reservoir.

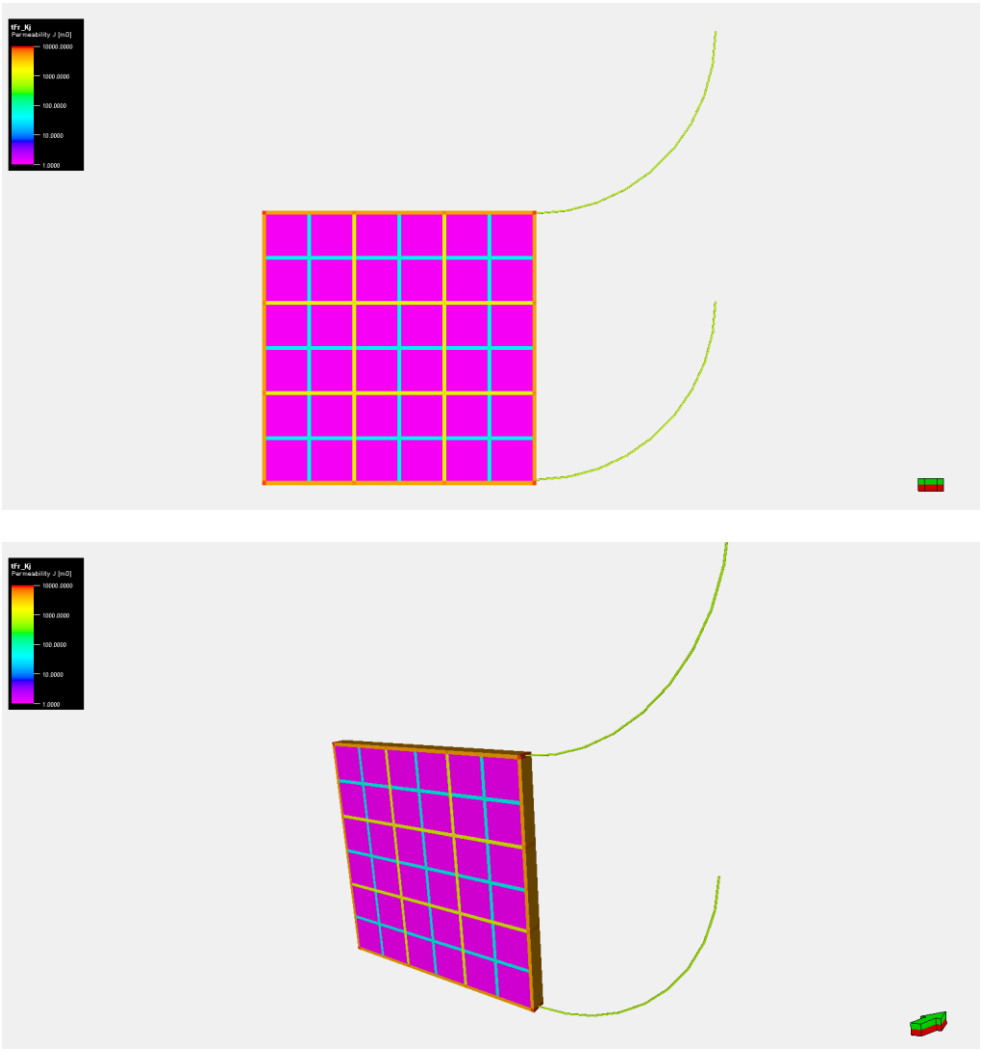

Figure 24: Horizontal wells in the 2D vertical slice. The top well serves as the injector and the bottom well as the producer

In Table 7, the parameters of the model are shown. The development strategy is conducted via two schemes: vertical wells and horizontal wells separately to compare the effects of both well orientations on all the fracture sets. However, the injection rate and the producer bottom hole pressure were selected to prevent too high a drawdown and to allow for the gravity effects to be active. Moreover, the injection rate was selected to maintain the pressure, as can be seen in Figure 26. The pressure response is very similar for all the cases, regardless of the fracture type or well orientation used. Over the period of 5 years, 2 pore volumes of gas were injected.

Table 7: 2D vertical primary production parameters

model	2D vertical	
dimension XZY	15x1x15	m
cell count XYZ	67x1x67	
recovery process	gas injection	
SCAL	GH	
fluid model	GH	
injection rate	0.05	m^3/day
producer BHP	249	bar
well orientation	horizontal + vertical	
production period	5	year

Simulation results for cases with vertical and horizontal wells were obtained. The gas injection takes place with 0.05m^3/day under reservoir conditions, regardless of whether vertical or horizontal wells are used. Over the period of 5 years, 2 pore volumes of gas were injected. The differences can be observed in Figure 25. Horizontal wells perform better compared to vertical wells, which is mostly related to enhanced gravity effects. Thus, horizontal wells are implemented in the 3D cube model for future studies. Moreover, the results obtained show the inverse trend for the fracture effect. Due to the matrix size reduction, simulation cases with only major fractures perform better than cases with major + medium or major + medium + minor fractures. More studies will follow in this work to verify this inversed trend using an extended vertical model and the 3D cube.

Figure 25: Comparison between horizontal and vertical wells for all fracture types during gas injection

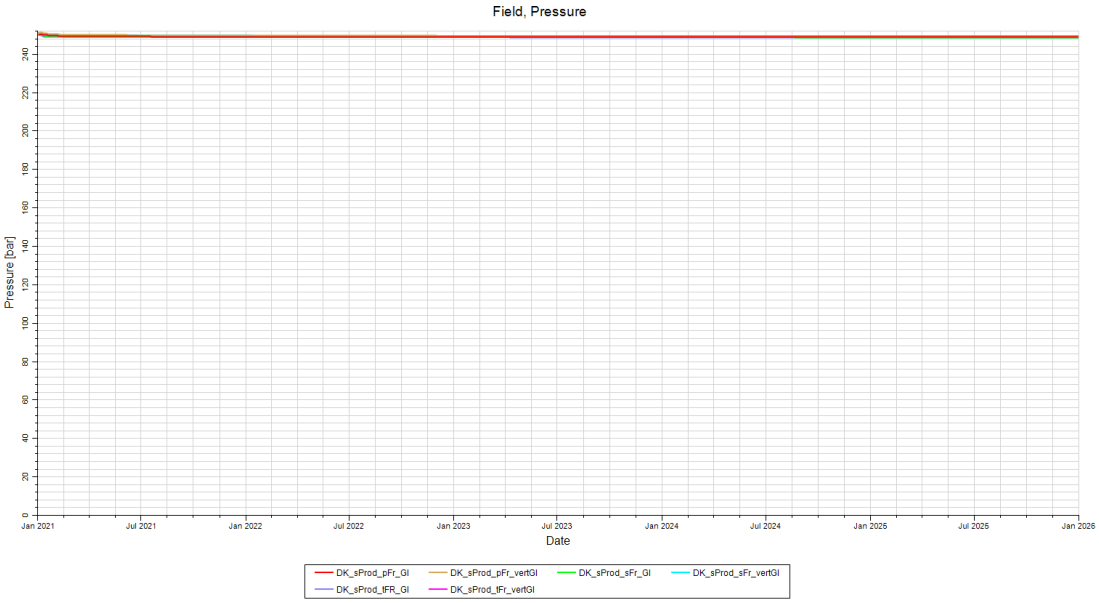

Figure 26: Pressure response for the secondary production (Gas injection) for horizontal and vertical wells

Figure 27, Figure 28, and Figure 29 represent the gas saturation for all the fracture types with vertical wells, whereas Figure 30, Figure 31, and Figure 32 do so for horizontal wells. Regardless of well orientation, fractures distribute the gas faster than the matrix.

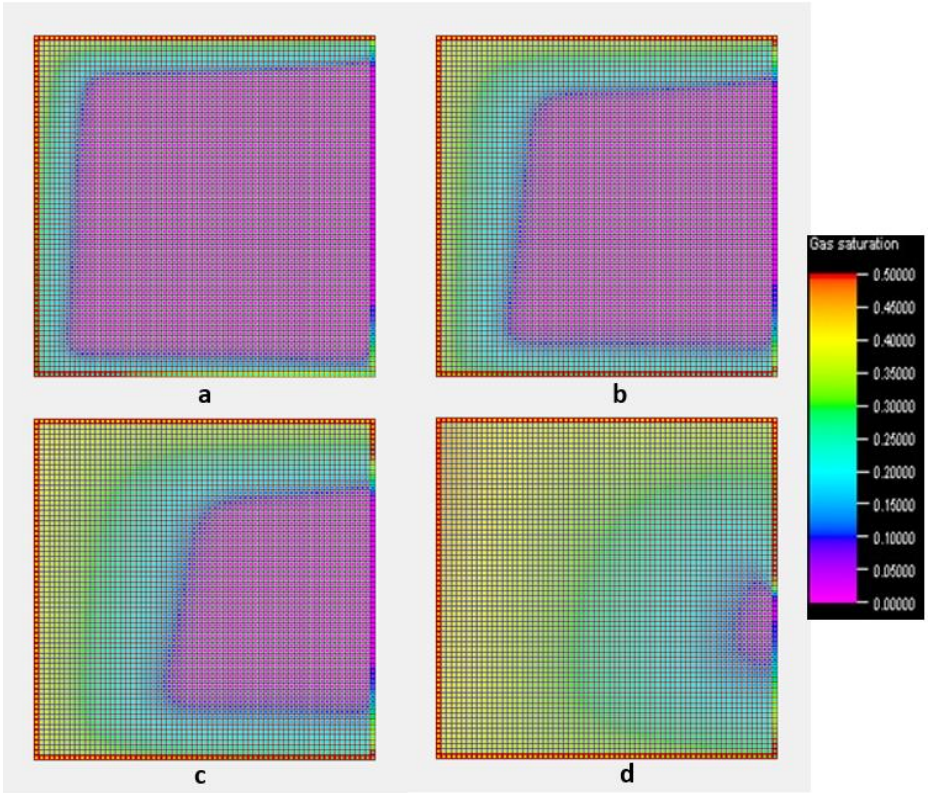

Figure 27: Gas saturation distribution in the vertical slice (Major fractures) with vertical wells after a) 5 months b) 1 year c) 2 years d) 5 years

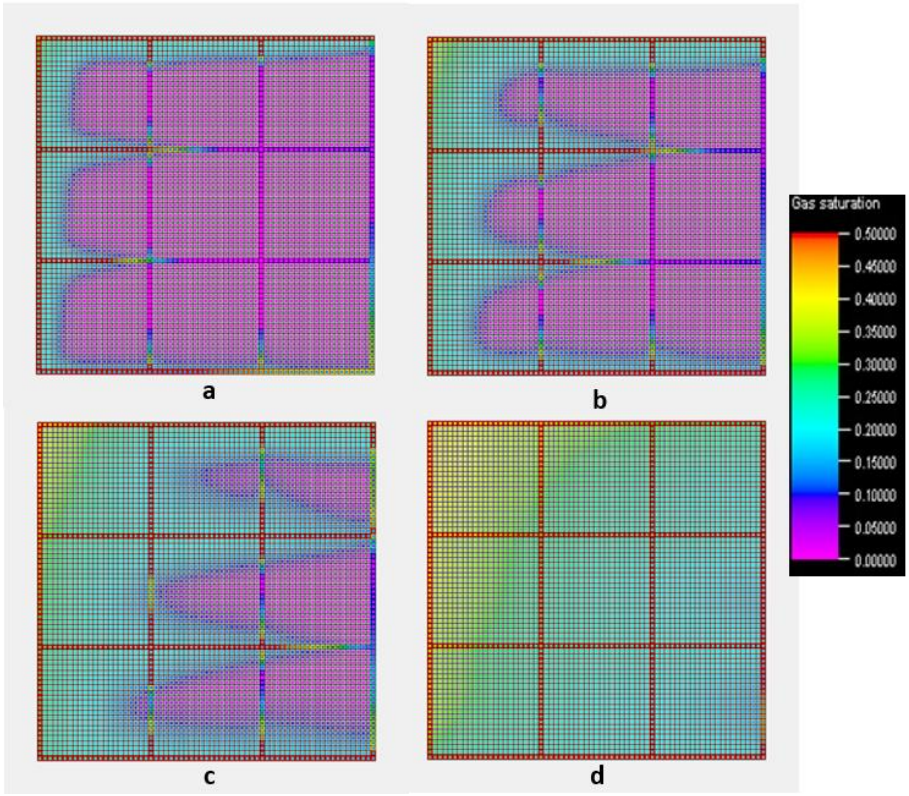

Figure 28: Gas saturation distribution in the vertical slice (major and medium fractures) with vertical wells after a) 5 months b) 1 year c) 2 years d) 5 years

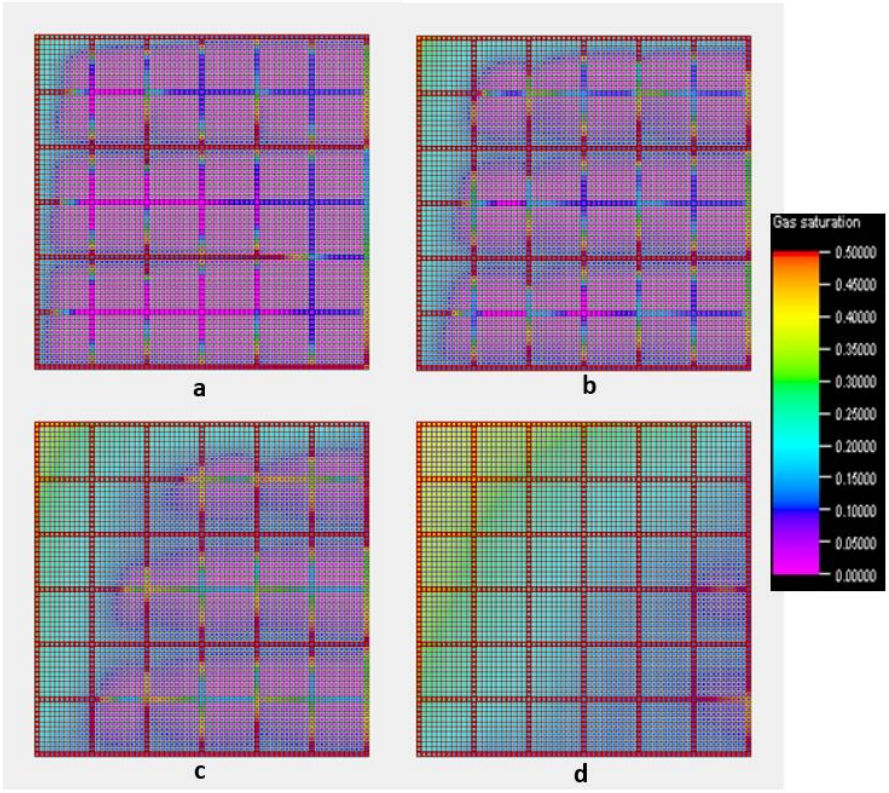

Figure 29: Gas saturation distribution in the vertical slice (major, medium, and minor fractures) with vertical wells after a) 5 months b) 1 year c) 2 years d) 5 years

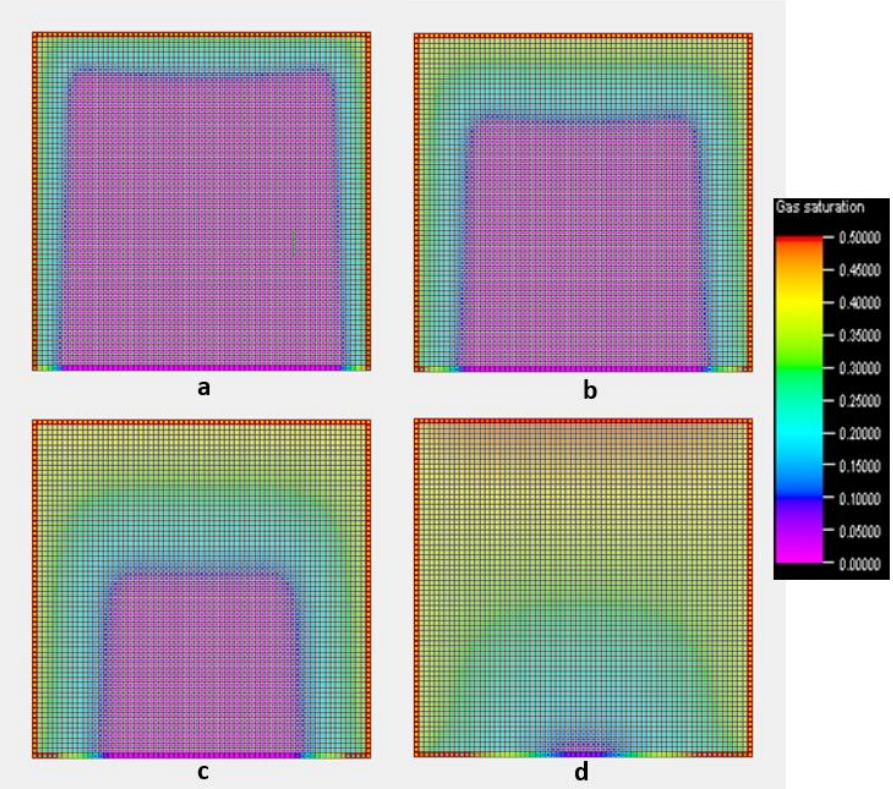

Figure 30: Gas saturation distribution in the vertical slice (major fractures) with horizontal wells after a) 5 months b) 1 year c) 2 years d) 5 years

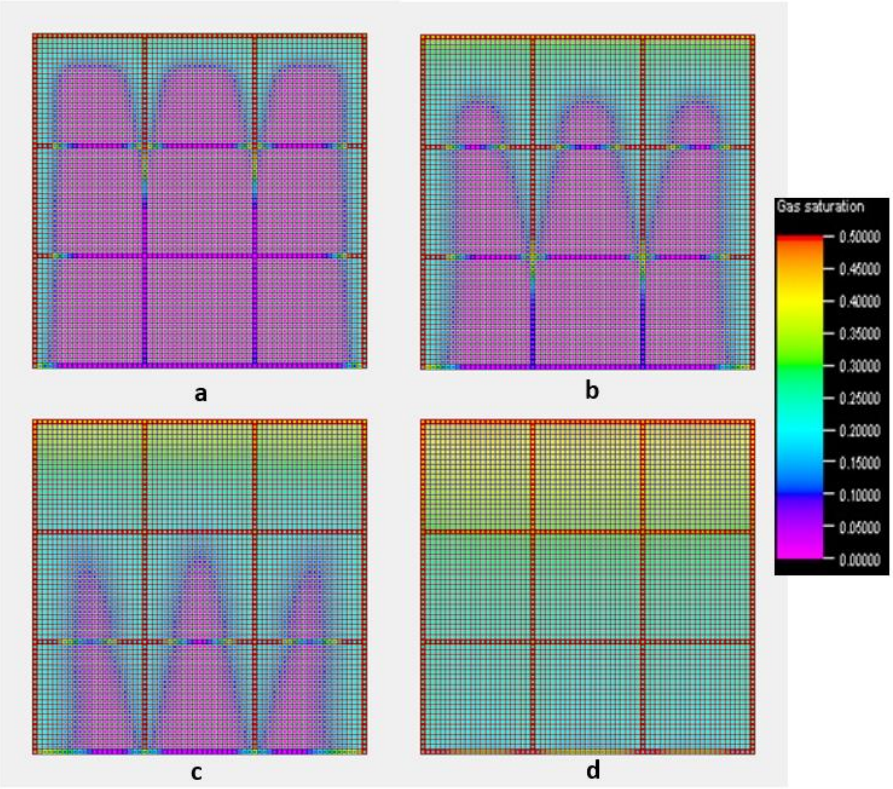

Figure 31: Gas saturation distribution in the vertical slice (major and medium fractures) with horizontal wells after a) 5 months b) 1 year c) 2 years d) 5 years

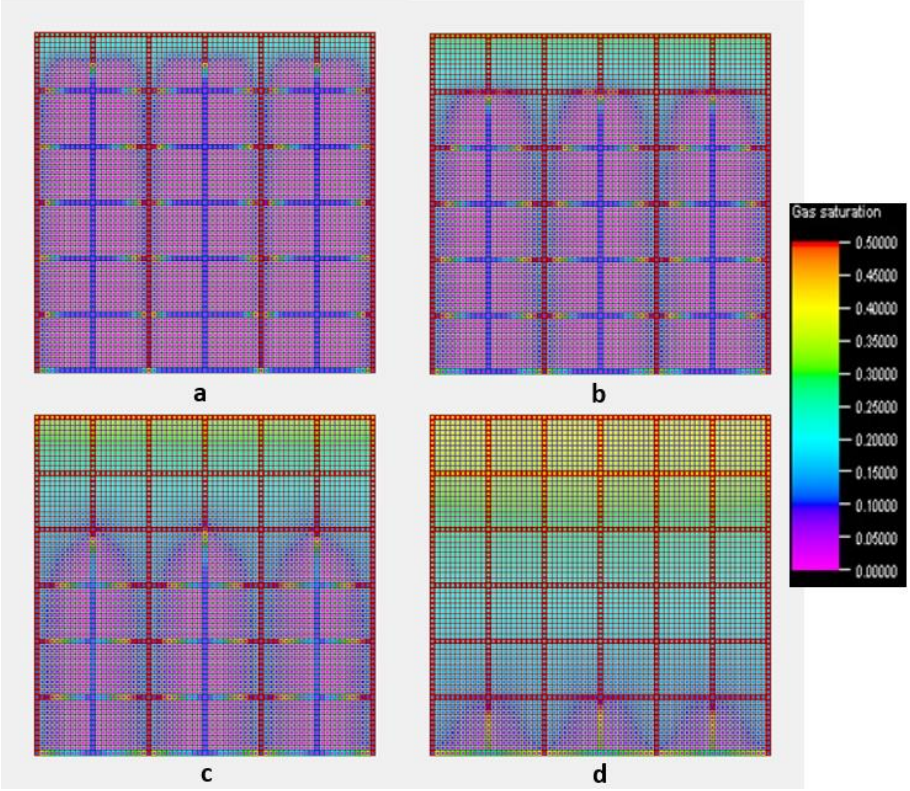

Figure 32: Gas saturation distribution in the vertical slice (major, medium, and minor fractures) with horizontal wells after a) 5 months b) 1 year c) 2 years d) 5 years

To verify the capability of our model in capturing all the gravity-related effects, another model was created with doubled size in vertical length. This extended 2D vertical slice model resembles the normal 2D vertical, but with double height, as shown in Table 8. With its larger height in Y-direction, it allows finding evidence that the observed results from the 2D vertical slice are not due to limited height and eventually limited gravitational effects.

Table 8: Parameters of the 2D extended vertical model

model	2D vertical	
dimension XZY	15x1x30	m
cell count XYZ	67x1x134	
recovery process	gas injection	
SCAL	GH	
fluid model	GH	
injection rate	0,08	m^3/day
producer BHP	250	bar
well orientation	horizontal	
production period	5	year

As shown in Figure 33, the extended vertical slice model demonstrates the same behavior as the shorter vertical model. The case with only the major fracture type surrounding the model has the largest matrix block, resulting in the highest ultimate recovery. The gas breakthrough occurs very fast in the major fracture case and even faster in the cases which feature more fracture types. However, the major fracture case has the lowest GOR throughout injecting 2 PV (Figure 34), indicating that the higher matrix block allowed more oil to be displaced. The gas saturation distribution resembles exactly the findings from the shorter vertical slice.

Figure 33: The recovery efficiency for secondary production gas injection in the extended vertical slice

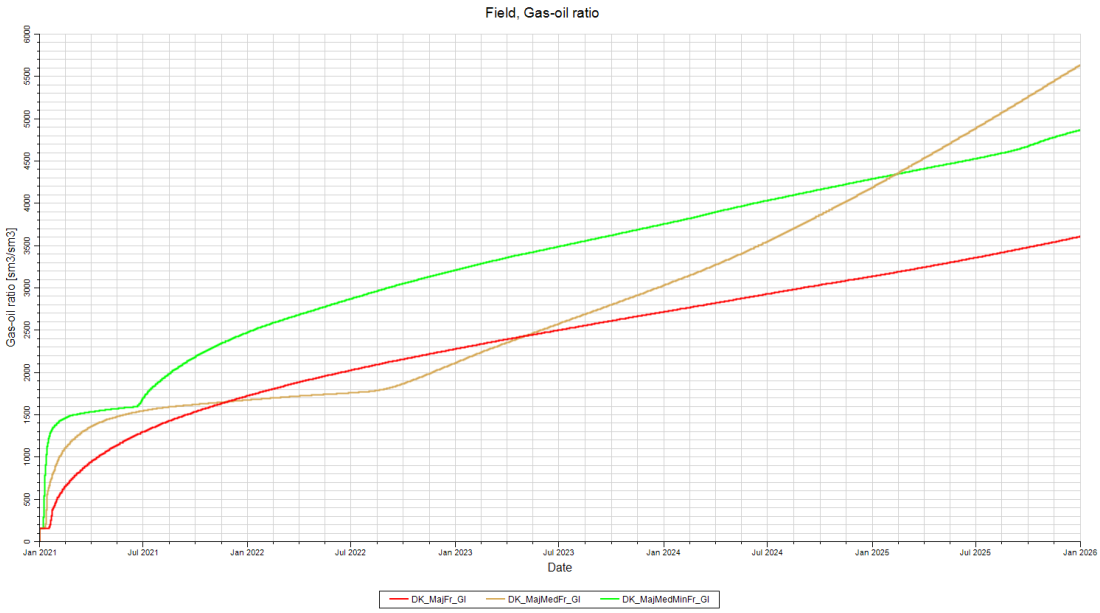

Figure 34: GOR for the extended vertical slice

4.3 3D cube

The 3D cube combines methods from the two 2D models and aims to verify results. Additionally, dimensionless numbers such as gravity, capillary, and bond numbers are calculated to give insight into the forces dominating the flow through the fractured reservoir.

This model was built with 15x15x15 m dimensions (37x37x37 grid cells) and two sets of wells. The injector and producer are on opposite edges of the model cube. The first set of wells consists out of vertical wells for the primary and water flooding simulation. The second set of wells considers horizontal wells for the gas injection case to promote the different gravity related mechanisms. In Figure 35, the 3D cube with major, medium, and minor fractures is represented. The upper (blue) well is the horizontal injector, whereas the bottom (red) well is the horizontal producer. The first layer is removed on purpose in order to reveal the distribution of the fractures within. For the simulation the whole block was surrounded from all sides by fractures.

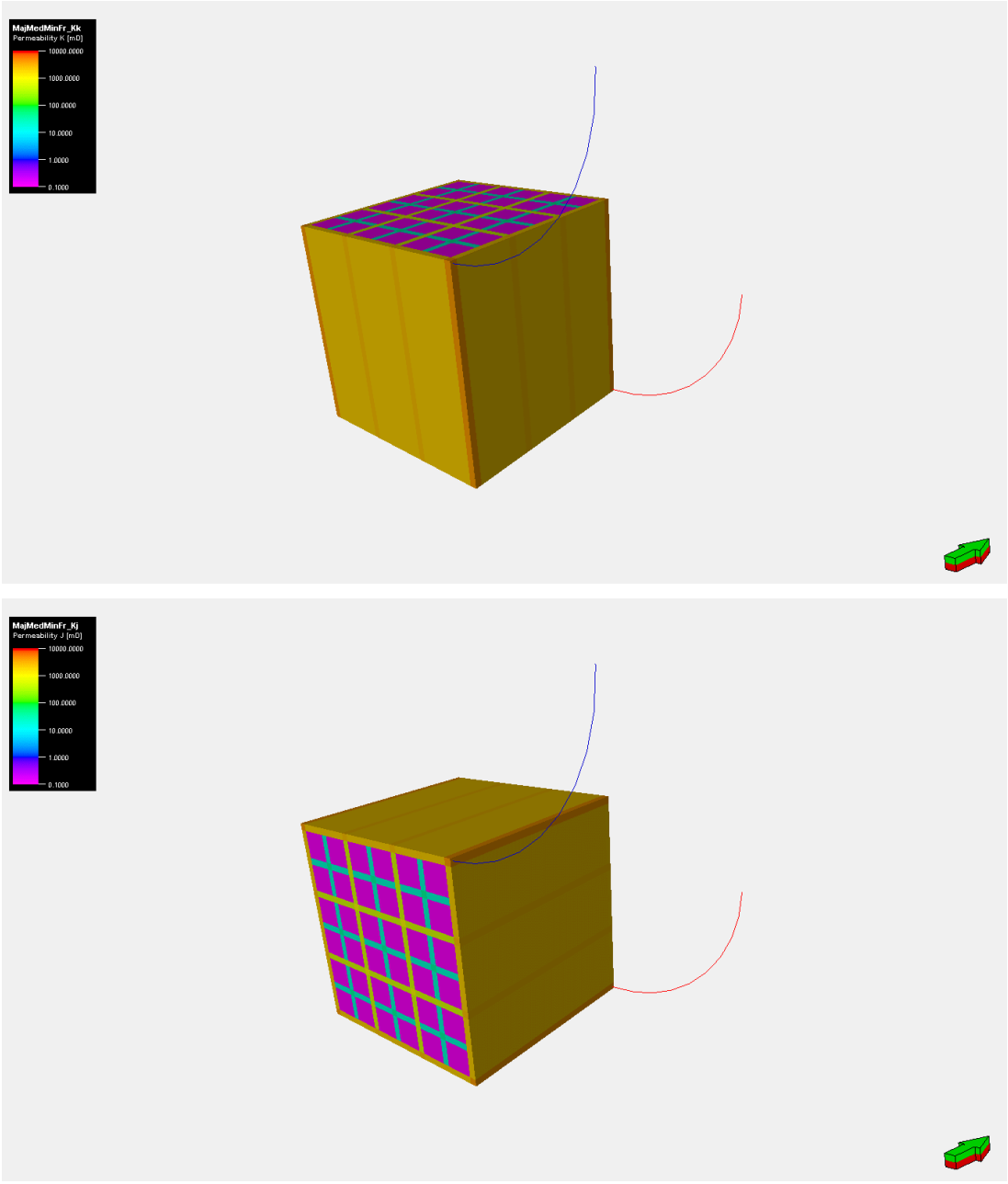

Figure 35: Fracture distribution of the 3D cube

4.3.1 Primary recovery

The general parameters used in the 3D cube under the primary production stage are summarized in Table 9.

Table 9: 3D cube primary production parameters

model	3D cube	
dimension XZY	15x15x15	m
cell count XYZ	37x37x37	
recovery process	primary production	
SCAL	GH	
fluid model	Dead Oil	
injection rate	-	m^3/day
producer BHP	5	bar
well orientation	vertical	
production period	1	year

The maximum recovery efficiency was reached with all fractures included (major + medium + minor fractures), as shown in Figure 36. This result indicates that fractures can have beneficial effects on oil recovery, corresponding with the literature (Gong & Rossen, 2018). The lowest recovery efficiency was achieved with only the major fractures included; an increase of 32% can be observed when medium fractures are added to the existing major fractures. If major, medium, and minor fractures are considered, the increase is around 40% compared to the only major fracture case.

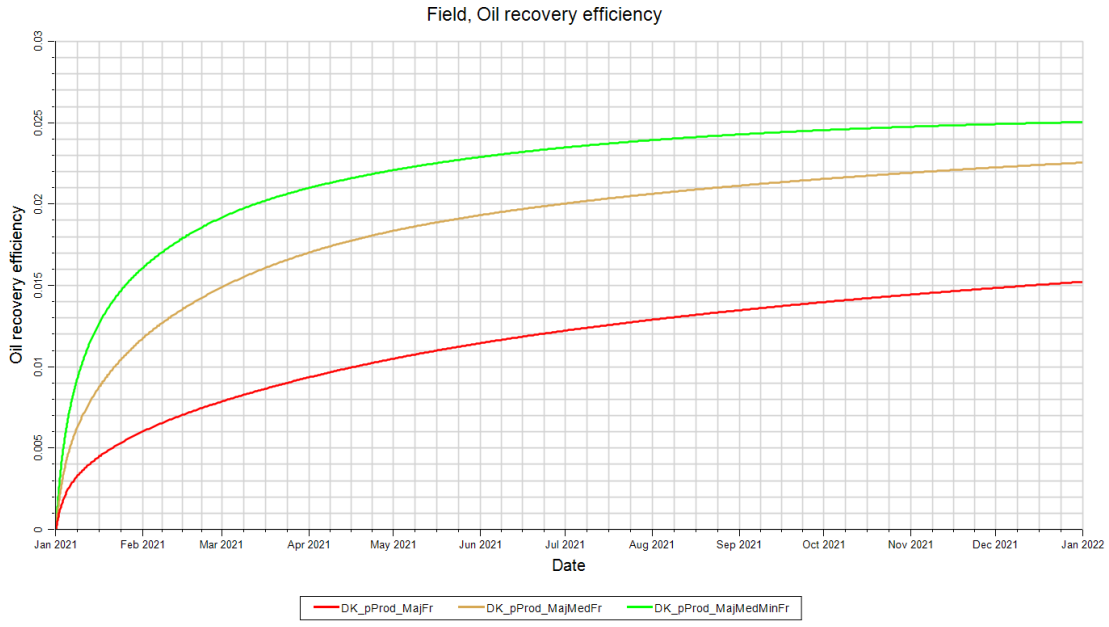

Figure 36: Recovery efficiency for all three fracture sets under primary production

The pressure response was consistent with the recovery results (Figure 37). The more recovery acquired, the more severe the pressure drop because no pressure support is supplied in this case. The pressure distributions are shown in Figure 38, Figure 39, and Figure 40, taken from a central slab of the 3D cube over various time steps. The slab is parallel with the vertical producer well. It shows how fractures enhance flow and thus pressure drop.

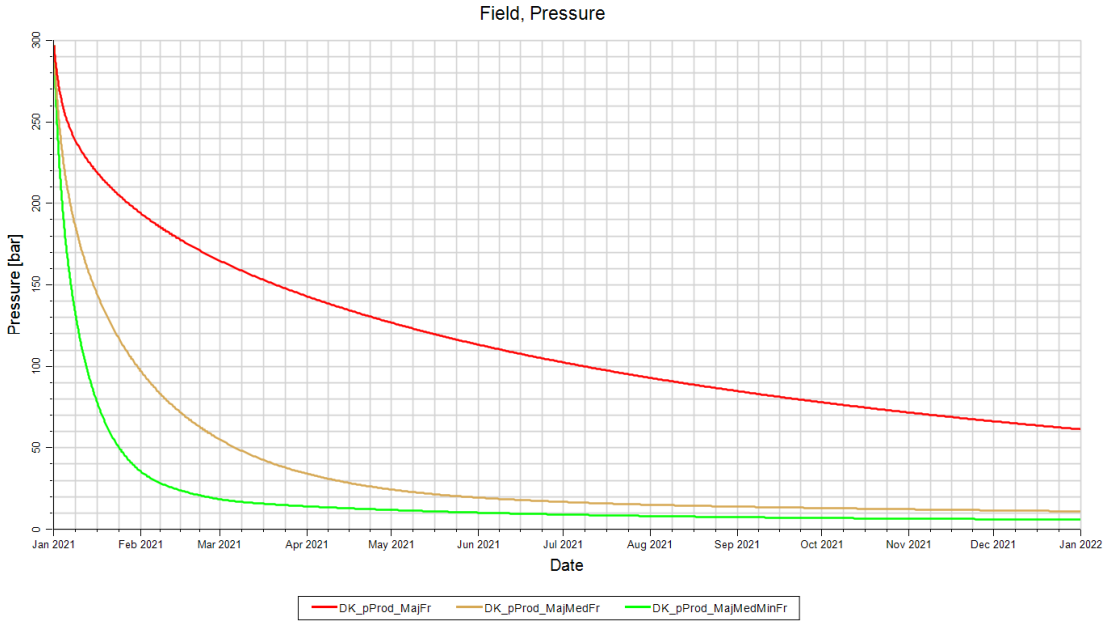

Figure 37: Pressure response for primary production

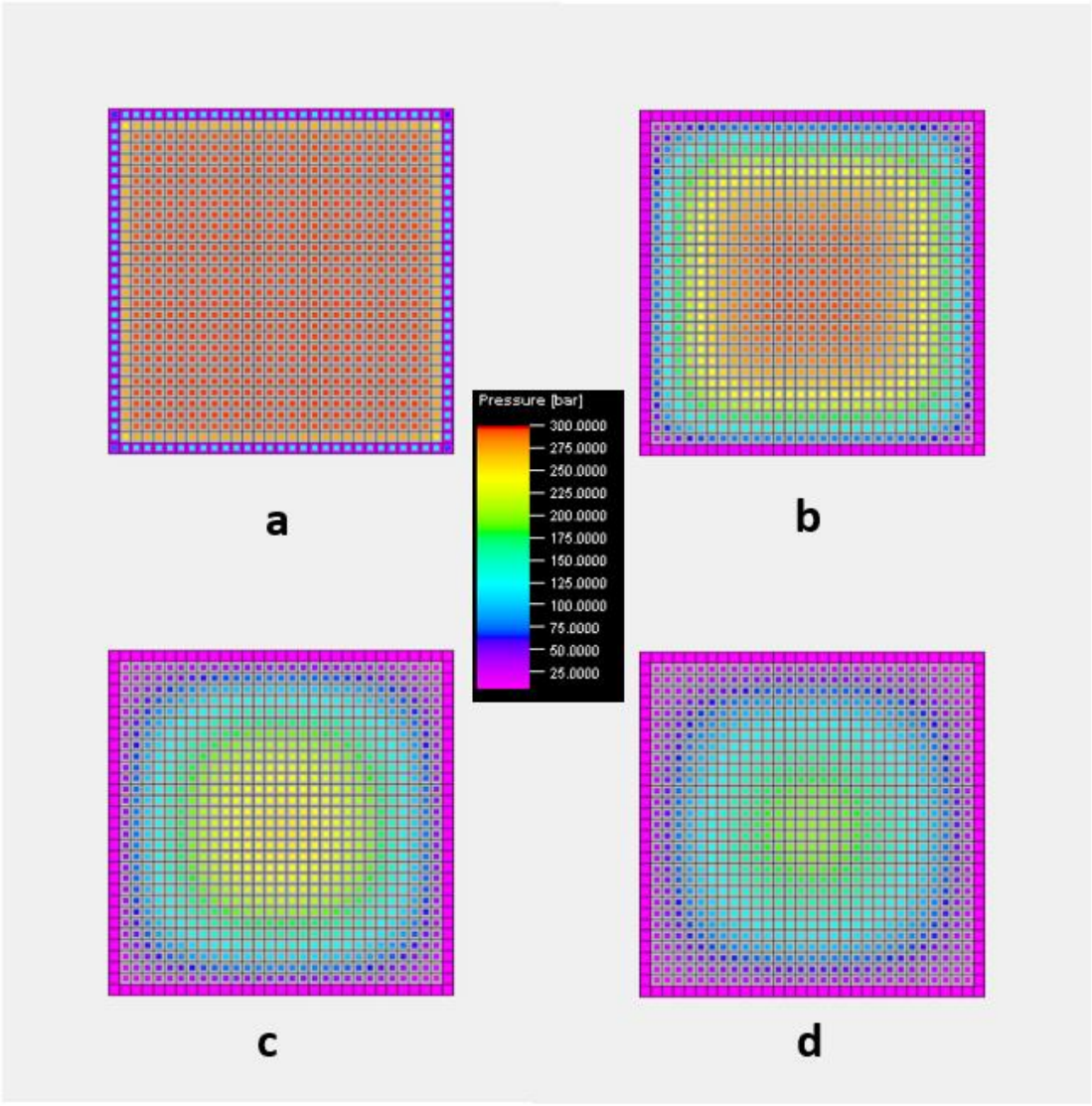

Figure 38: Pressure distribution in the center of the 3D cube for major fractures at different times (a) 4 days (b) 5 months (c) 9 months (d) 12 months

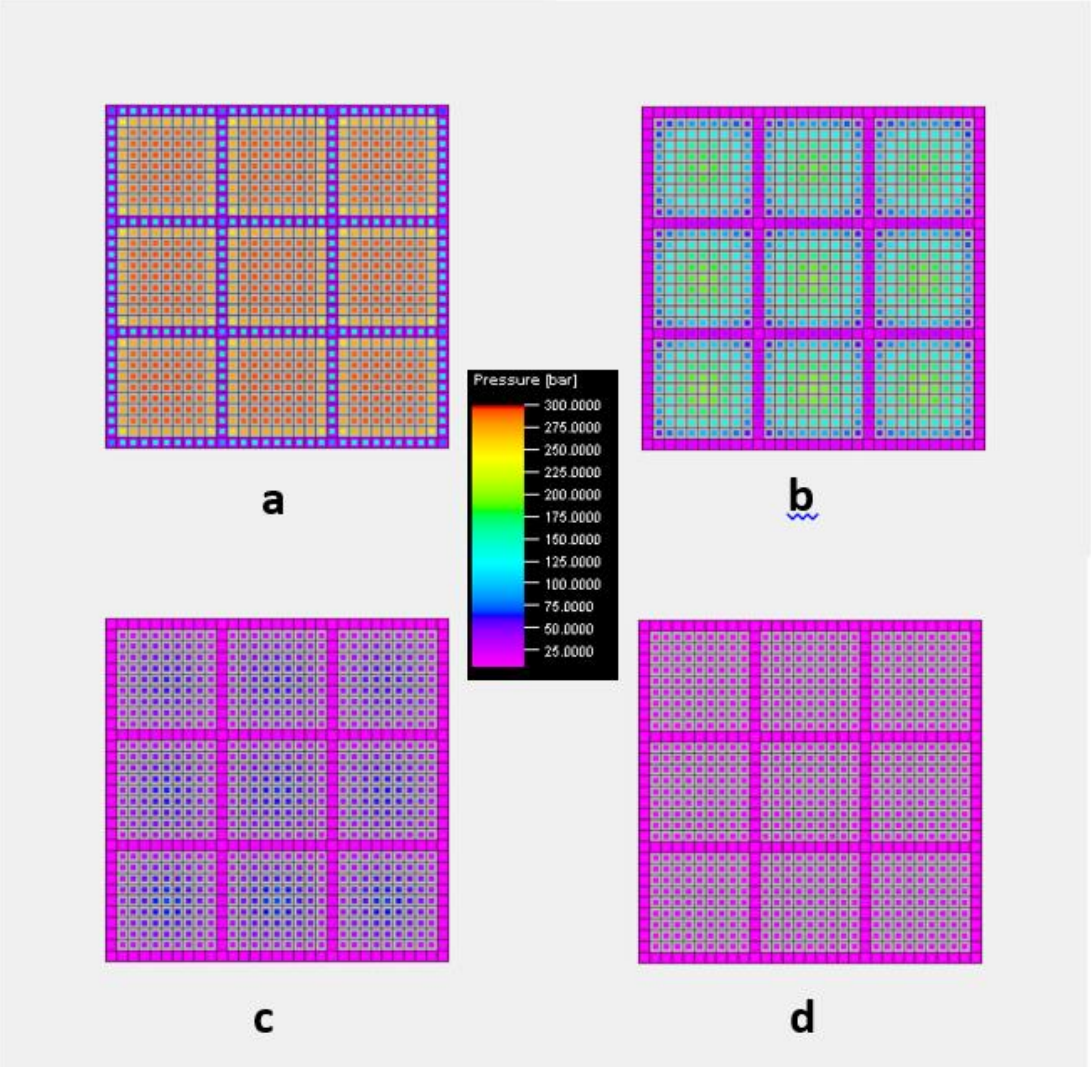

Figure 39: Pressure distribution in the center of the 3D cube for major and medium fractures at different times (a) 4 days (b) 2 months (c) 5 months (d) 9 months

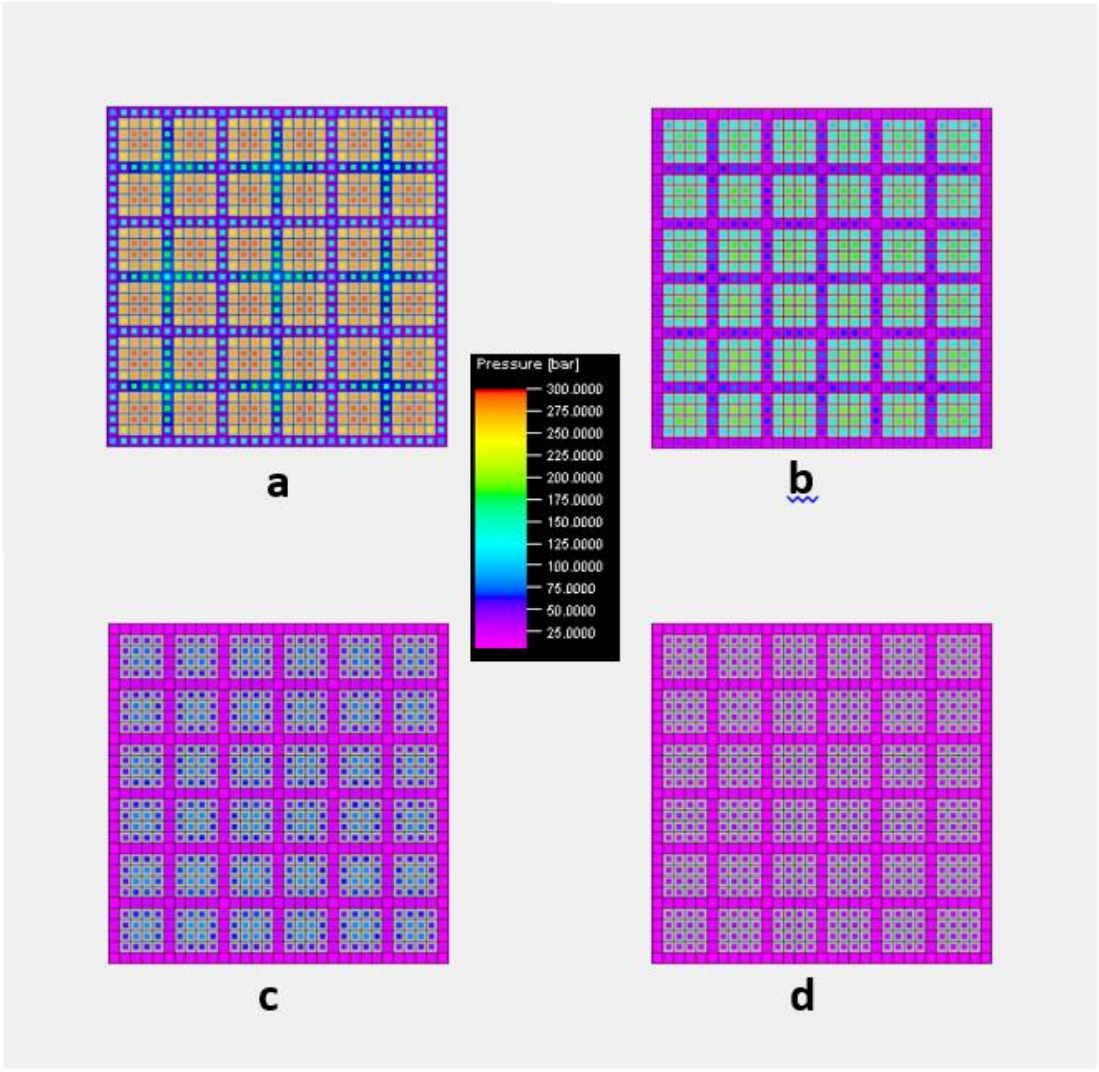

Figure 40: Pressure distribution in the center of the 3D cube for major, medium, and minor fractures at different times (a) 4 days (b) 15 days (c) 2 months (d) 2.5 months

4.3.2 Secondary Production – Gas Injection

In Table 10, the parameters used in this section are summarized. The horizontal well scheme was used to promote the gravitational drainage mechanism for the gas injection. The horizontal producer is constrained with a pressure limit of 250bar in order to avoid too high drawdown. The initial reservoir pressure is also 250bar at the top of the reservoir. The reservoir pressure at the bottom is naturally higher due to hydrostatics. So basically, the idea is to keep the pressure as constant as possible during the simulation run.

Table 10: 3D cube gas injection parameters

model	3D cube	
dimension XYZ	15x15x15	m
cell count XYZ	37x37x37	
recovery process	gas injection	
SCAL	GH	
fluid model	GH	
injection rate	0.247	m^3/day
producer BHP	250	bar
well orientation	horizontal	
production period	15	year

The main observation is that the three cases show the opposite order compared to the primary production. When only major fractures are included, the highest recovery is obtained, which might be related to the size (height) of the matrix block. On the other hand, when more fractures are included, the matrix blocks become smaller, leading to disconnected oil clusters and lower the total mobility of the oil phase. This statement is based on results generated with different vertical matrix block sizes. Higher recoveries can be reached with larger matrix block sizes, as presented in Figure 41. However, once additional fracture types are added to the model, the matrix block sizes decrease, decreasing recovery efficiency. Larger matrix block sizes allow for smoother displacement of oil by gas. Table 11 contains the matrix dimensions for cases with only major fractures, major + medium fractures, and major + medium + minor fractures.

Table 11: Matrix block dimension of different fracture combination

	Matrix dimension
MajFr	15x15x15m
MajMedFr	5x5x5m
MajMedMinFr	2.5x2.5x2.5m

The results in Figure 41 indicate that a 16% lower oil recovery was observed when medium fractures were included in the existing major fractures. This trend is even more prominent if minor fractures are considered along with the other two types. Another 6% decrease in oil recovery is observed if major, medium, and minor fracture cases are compared to the only major fracture case.

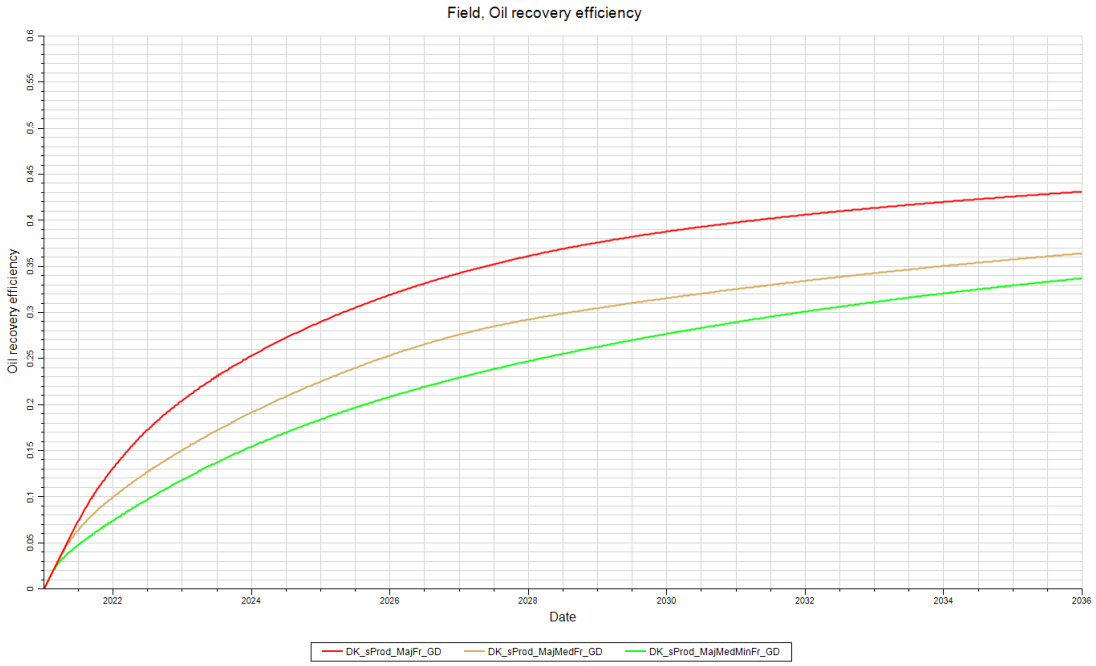

Figure 41: The recovery efficiency with gas injection in the 3D cube

The gas saturation for these cases is shown in Figure 42, Figure 43, and Figure 44. The gravity encroachment of the injected gas can be observed for all the cases. The smoothest displacement occurs for the case with the major fractures. Other additional fractures in the other cases enhance gas breakthrough and mitigate the ultimate recovery. The snapshots are taken perpendicular to the horizontal wells from a layer in X-direction from the center of the cube.

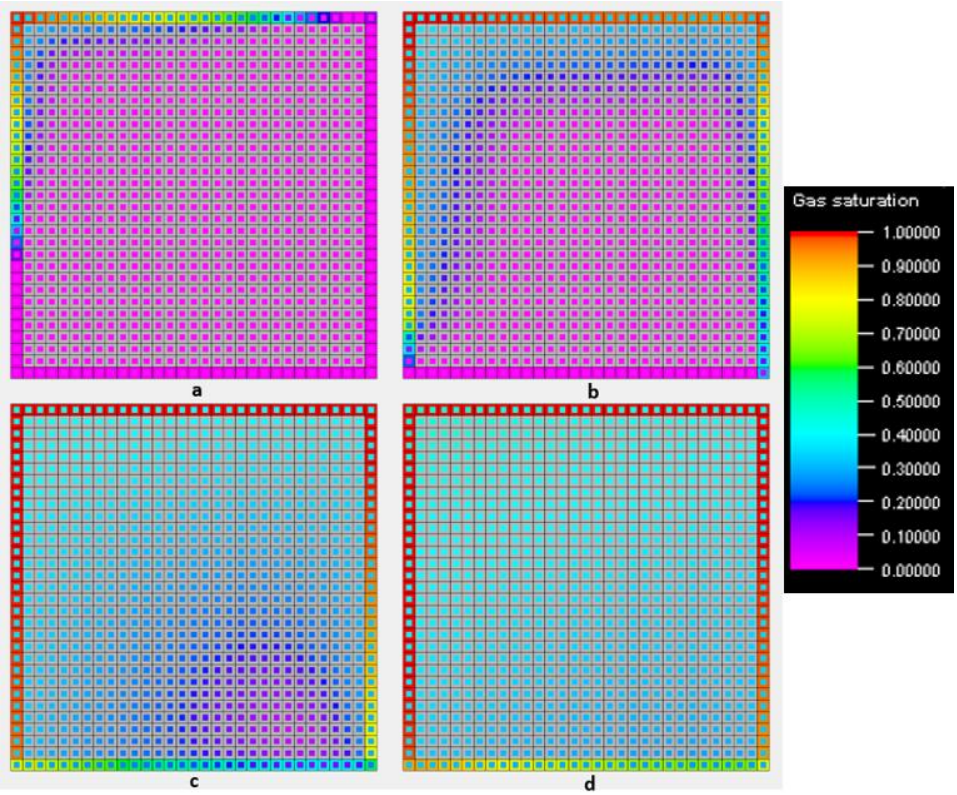

Figure 42: Gas saturation for the 3D cube with major fractures after a) 4months b) 18 months c) 7 years d) 13 years

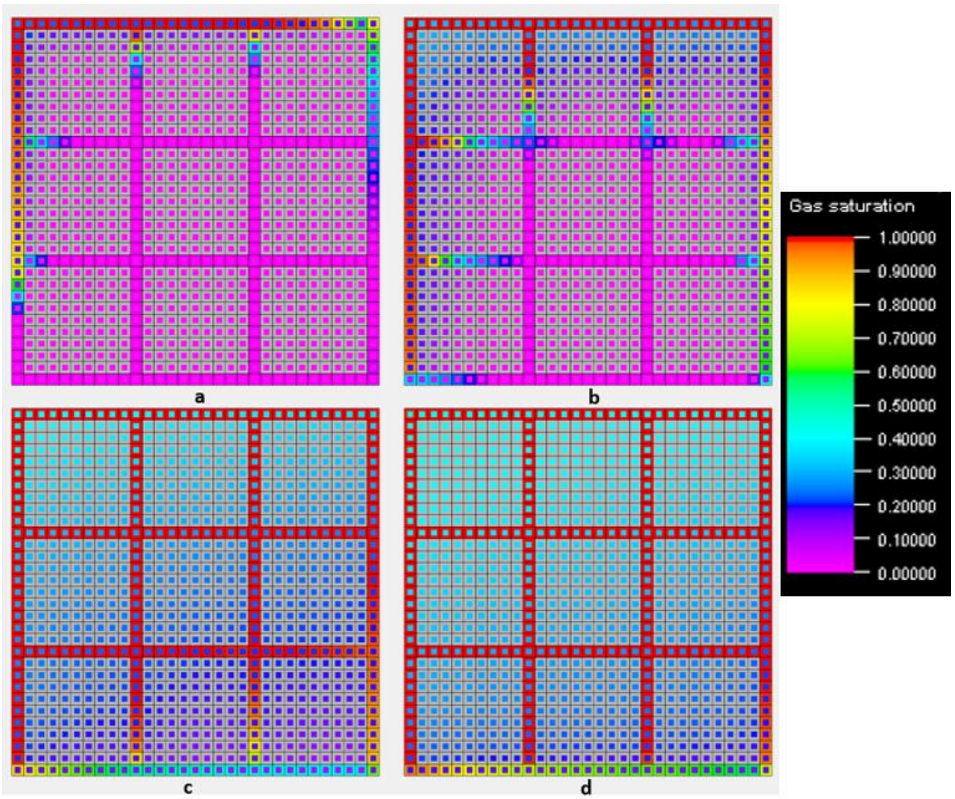

Figure 43: Gas saturation for the 3D cube with major and medium fractures after a) 4months b) 18 months c) 7 years d) 13 years

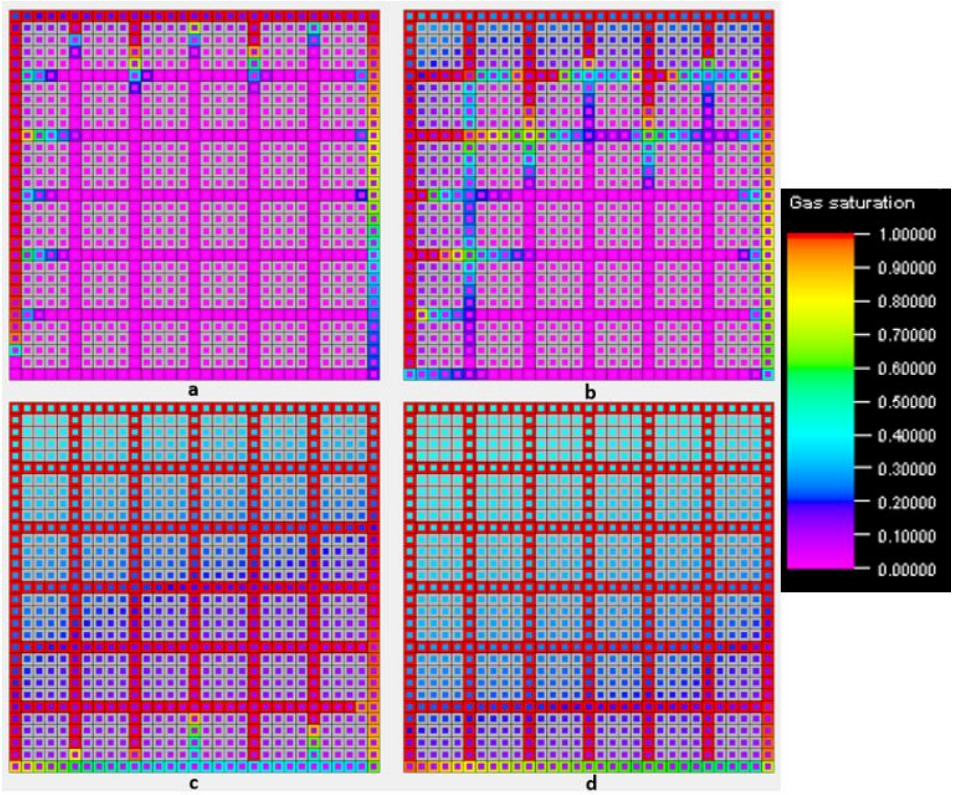

Figure 44: Gas saturation for the 3D cube with major, medium, and minor fractures after a) 4months b) 18 months c) 7 years d) 13 years

Almost identical pressure response (Figure 45) was observed in the three cases, although small differences can be noticed at the beginning of the runs. Cases with more fractures had a steeper decline in pressure, especially the case with major, medium, and minor fractures. In Figure 46, the gas rates correspond to the observed trend. The highest gas production is observed for the case with major, medium, and minor fractures, compared to the least gas produced for the major fracture case. This might be another indication that better displacement is reached if the matrix block is larger and breakthrough is delayed.

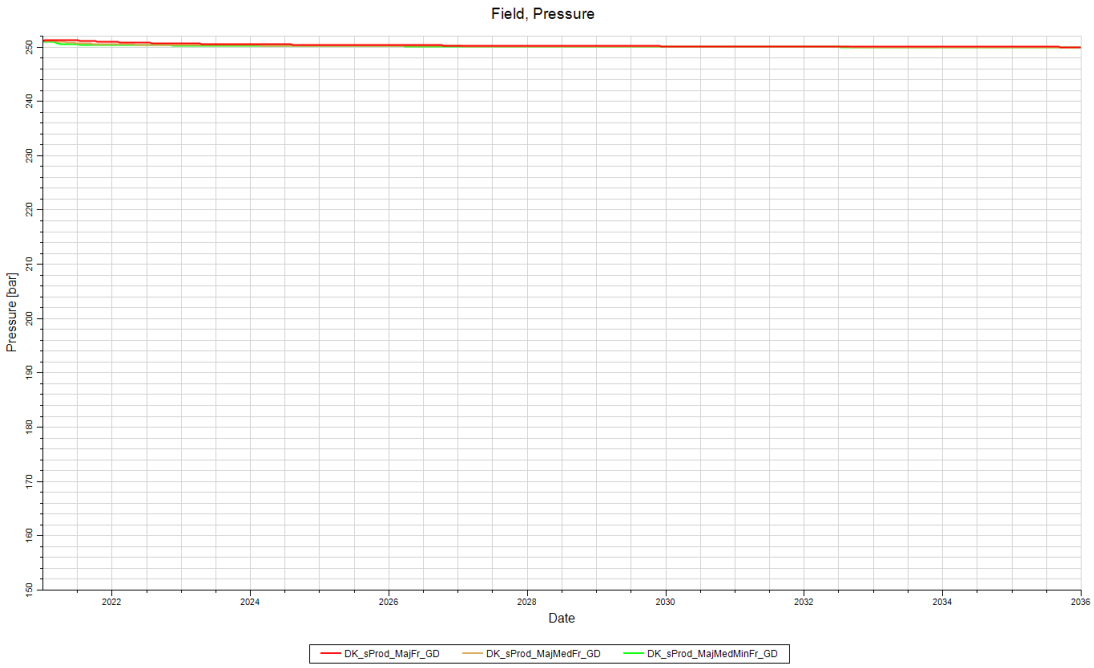

Figure 45: Pressure response for secondary production (Gas injection)

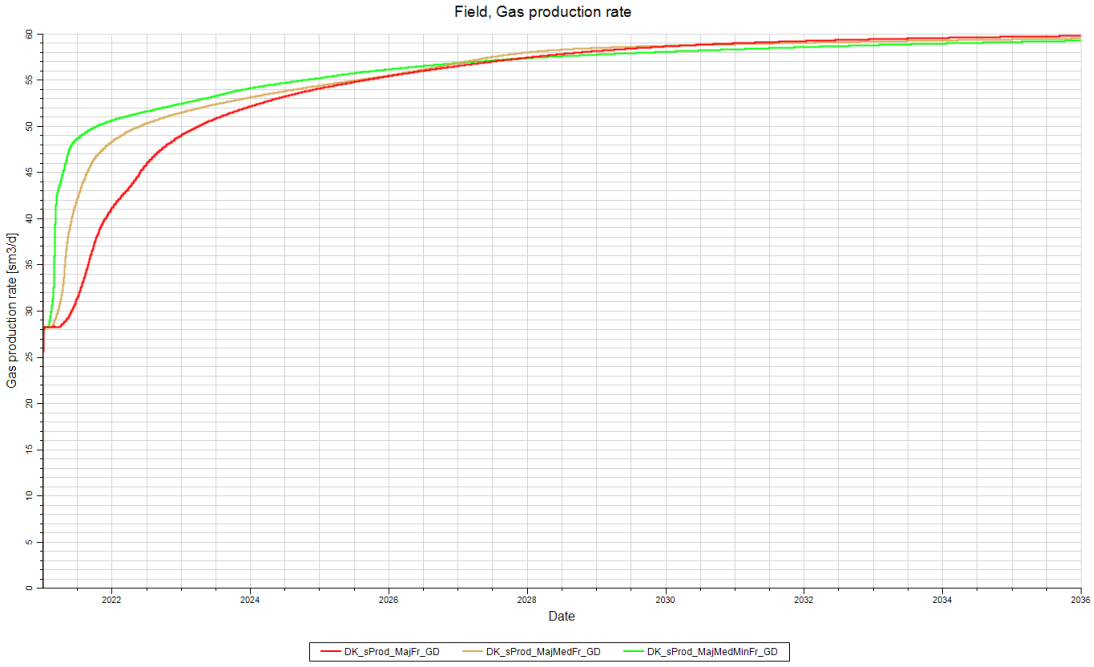

Figure 46: Gas production rate for the gas injection cases

4.3.2.1 Sensitivity

Different sets of fractures were placed at different locations to check whether the fracture types' distribution plays a role in production. For example, considering Figure 47, the “standard” case uses the following scheme: (a) major fractures, (b) medium fractures, and (c) minor fractures. Two additional distributions were tested, called Set 3, which consists of (a) minor, (b) medium, and (c) major fractures, and Set 5, which consists out of (a) minor, (b) major, and (c) medium fractures. The differences between differently distributed fracture sets can be observed in Figure 48. Interestingly, all sets performed similarly, with the biggest differences at the beginning and end of the simulation run. The best performance was observed with our “standard” case.

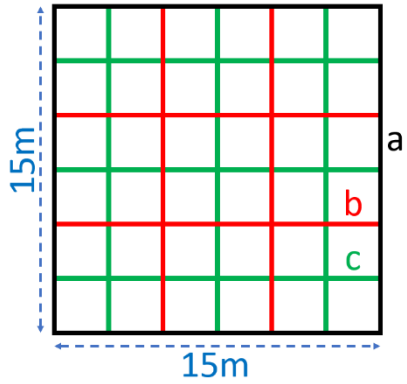

Figure 47: Distribution of fractures

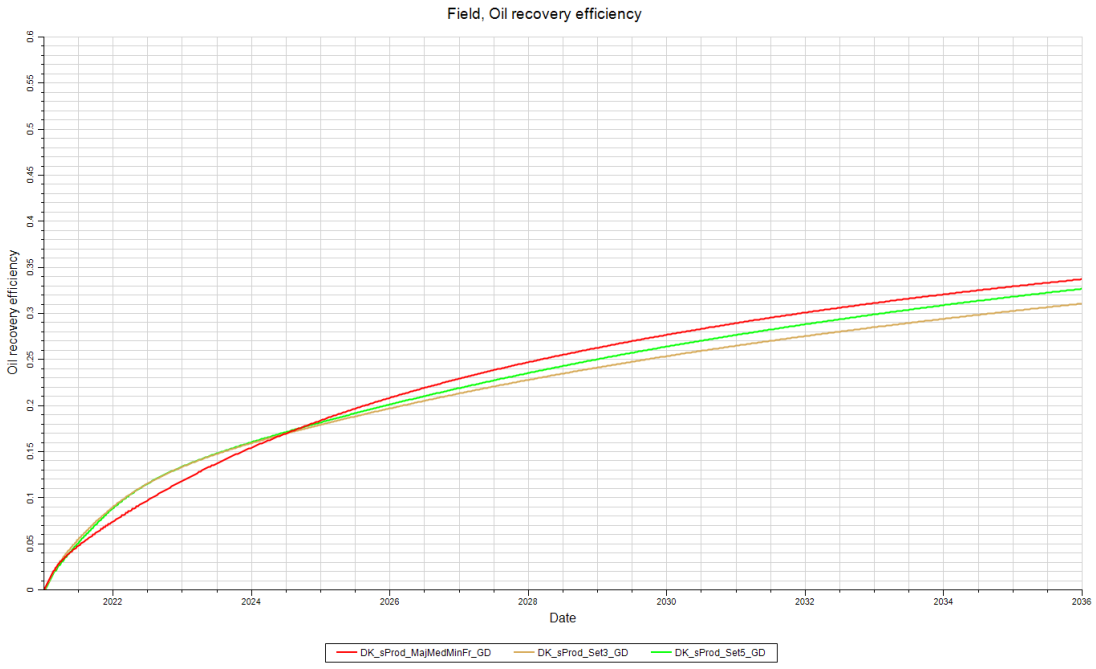

Figure 48: Fracture distribution sensitivity for gas injection case

In addition to the differently distributed fracture set, two more cases were generated - one case consists only of major fractures and the other only of minor fractures. Results were obtained for pressure constraint of the producer of 250 bar and a gas injection rate of 0.247m^3/day. As shown in Figure 49, performance is similar for the "standard" case (major + medium + minor fractures) and the case having all fractures as major fractures. The largest difference between these two cases is at the beginning of the simulation run. The case's significantly higher average fracture permeability creates a steeper slope, with all fractures being major. This is as expected because fractures are depleted faster than the matrix. Although all three cases shown in this figure have the same matrix block size, the case with all minor fractures performed the best. This might be related to the fact that the minor fractures are similar to a single porosity matrix system. The all-minor fracture case has more matrix dominant production than the case with all major fractures. This delays gas breakthrough and increases production efficiency considerably. In the first couple of years, the gas production rate was lower for the all-minor fracture case compared to the other two cases. Figure 50 shows the constant GOR for the first 2 years for the all-minor fracture case, indicating that breakthrough is delayed and displacement efficiency is promoted relative to the other two cases. On the other hand, the case with all major fractures shows a sudden increase in GOR at the initial years of the simulation, indicating the fast breakthrough of gas through the fractures.

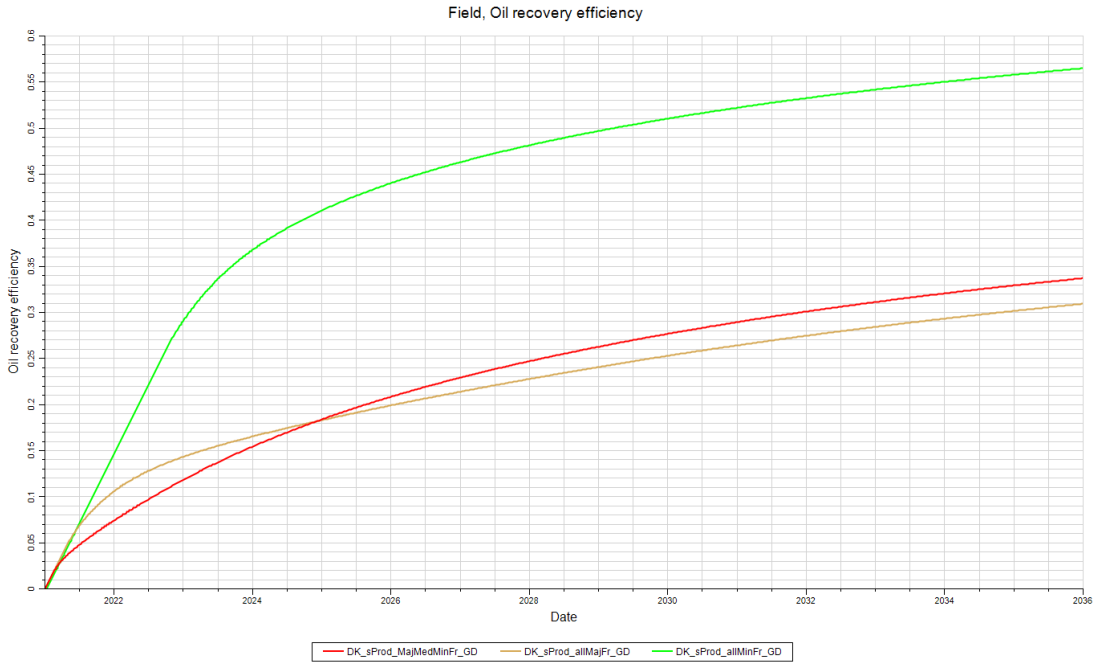

Figure 49: Comparison in recovery efficiency in case of all major and all minor fractures

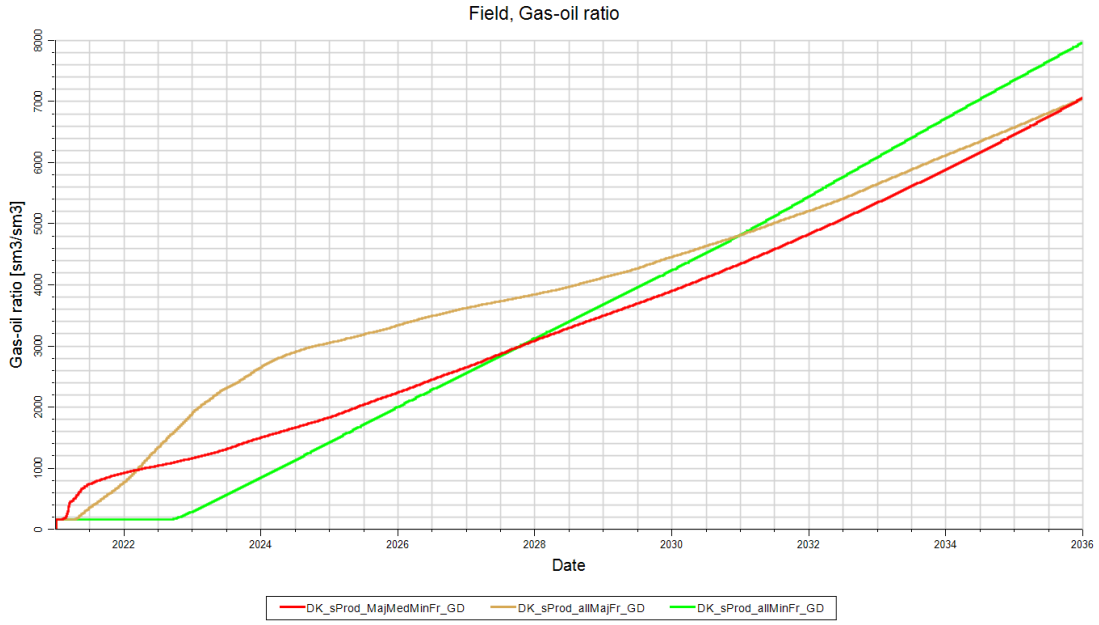

Figure 50: Comparison in GOR in the case for all major and all minor fractures

Following the studies of different fracture types and distributions, the next step was to study the oil's bottom hole pressure, wettability, and viscosity. The bottom hole pressure (BHP) was found to impact the recovery significantly. It represents the minimum limit of the pressure that can be reached at the producer and thus governs the drawdown pressure at the producer well. Table 12 summarizes the selected BHP values for the sensitivity study. The results are illustrated in Figure 51, Figure 52, and Figure 53 for different fracture type combinations. Steep slopes at the beginning can be observed for all fracture types, indicating that fractures are depleted very fast at the initial time steps. But very soon, a crossing point is reached, and going from there on, the results are as expected so far. Too high drawdown pressure mitigates the recovery efficiency.

Table 12: Pressures used for the BHP study

Sensitivity case	BHP constraint of producer
BHP 1	145bar
BHP 2	165 bar
BHP 3	185 bar
BHP 4	205 bar
BHP 5	225 bar
BHP 6	245 bar

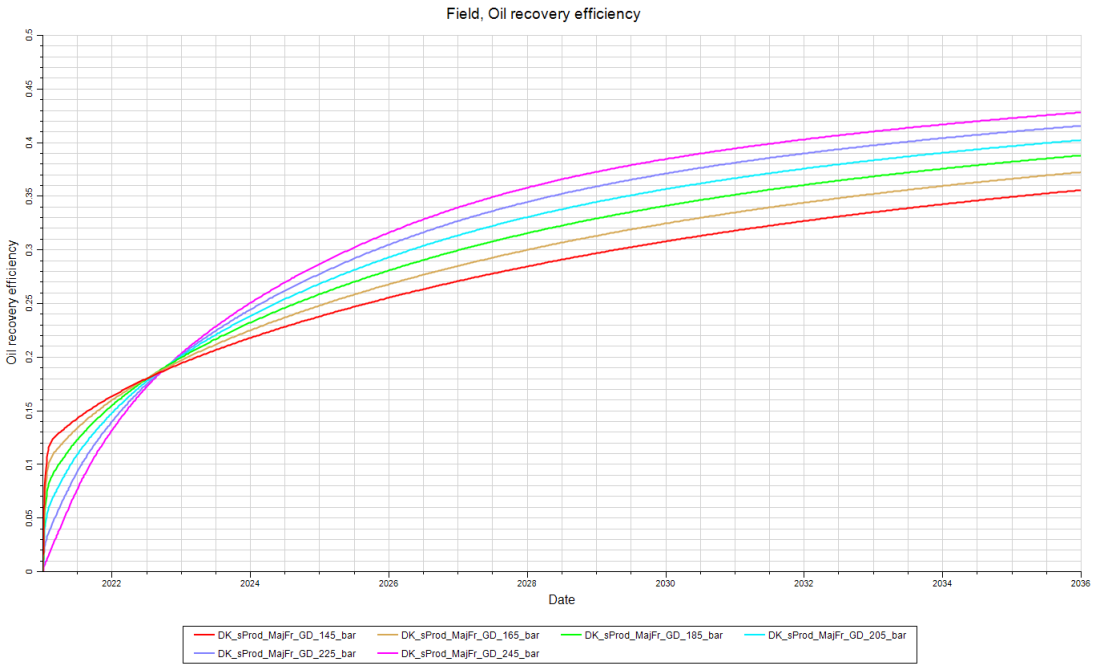

Figure 51: BHP sensitivity runs with major fractures included for gas injection

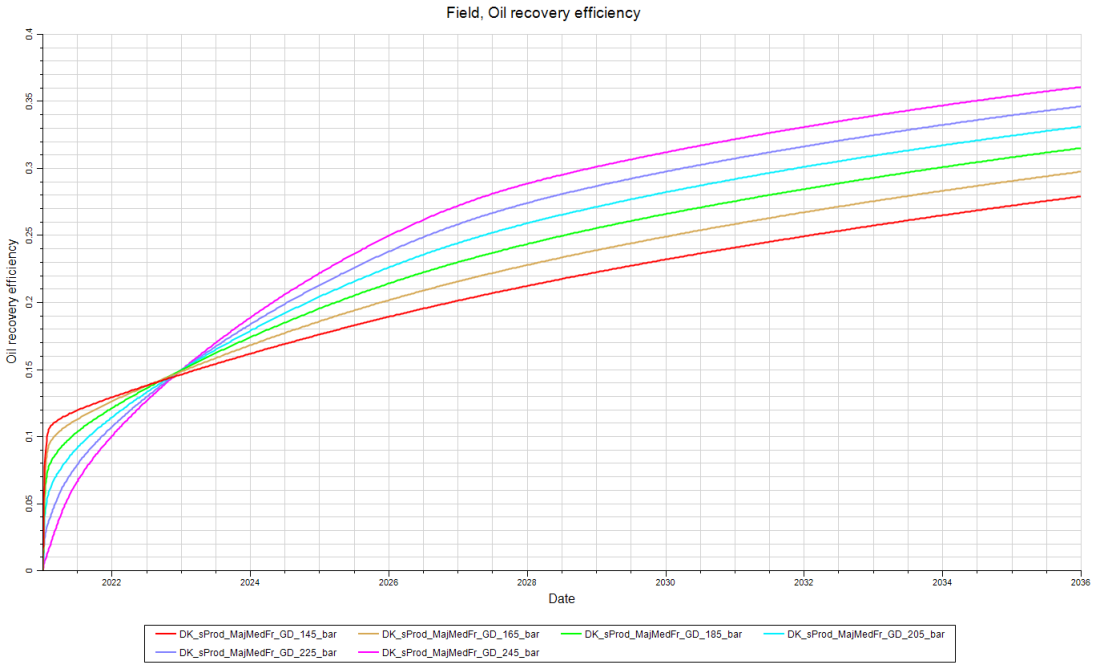

Figure 52: BHP sensitivity runs with major and medium fractures included for gas injection

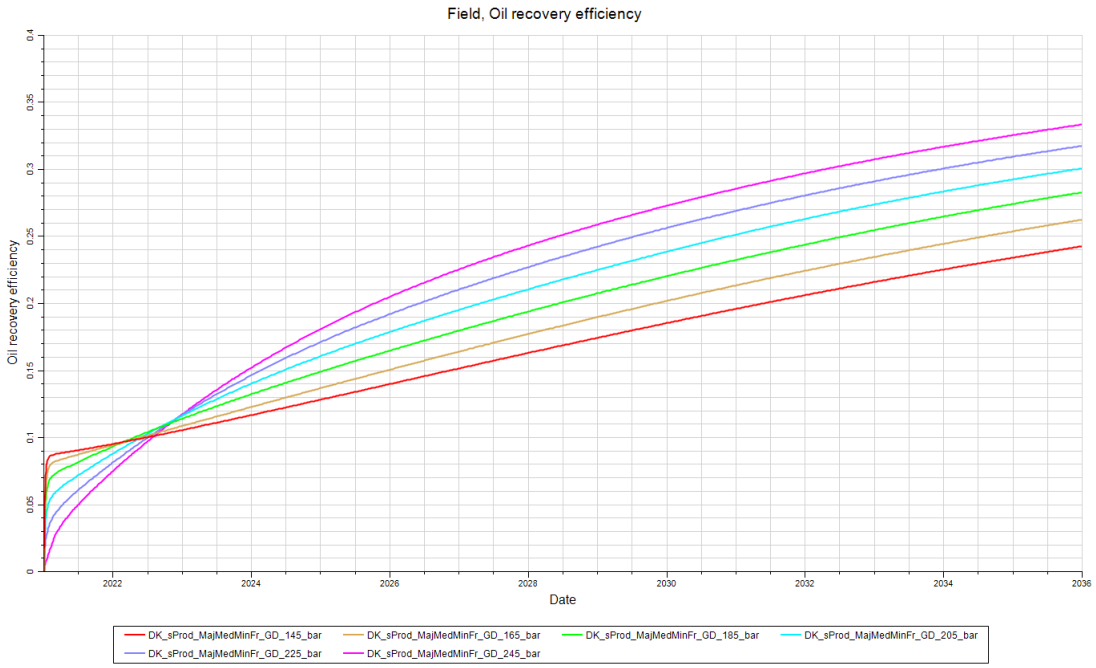

Figure 53: BHP sensitivity runs with major, medium, and minor fractures included for gas injection

To study the effects of different wettability conditions, new SCAL data was created. This synthetic data is different from the GH SCAL data, and thus direct comparison may not be that reasonable. Nevertheless, the effects of fractures can be studied, and results may be utilized for future dimensionless number calculations. In Figure 54, Figure 55, and Figure 56, the results of the wettability sensitivity for each fracture type combination are shown. Water-wet cases, in general, perform best at initial time steps, although on longer terms, their ultimate recovery is less than mixed-wet or oil-wet conditions.

Interestingly, the oil-wet cases reached approximately always 20% higher ultimate oil recovery than the water-wet cases. Regardless of how many fractures were introduced, the general trend between the different wettabilities is preserved. Between OW and WW cases, the mixed-wet case reached an intermediate ultimate oil recovery, maintaining pretty uniformly 9% higher recovery than the water-wet cases.

The relative permeability curves used to implement different wettability conditions are published in chapter 4.3.3.1.

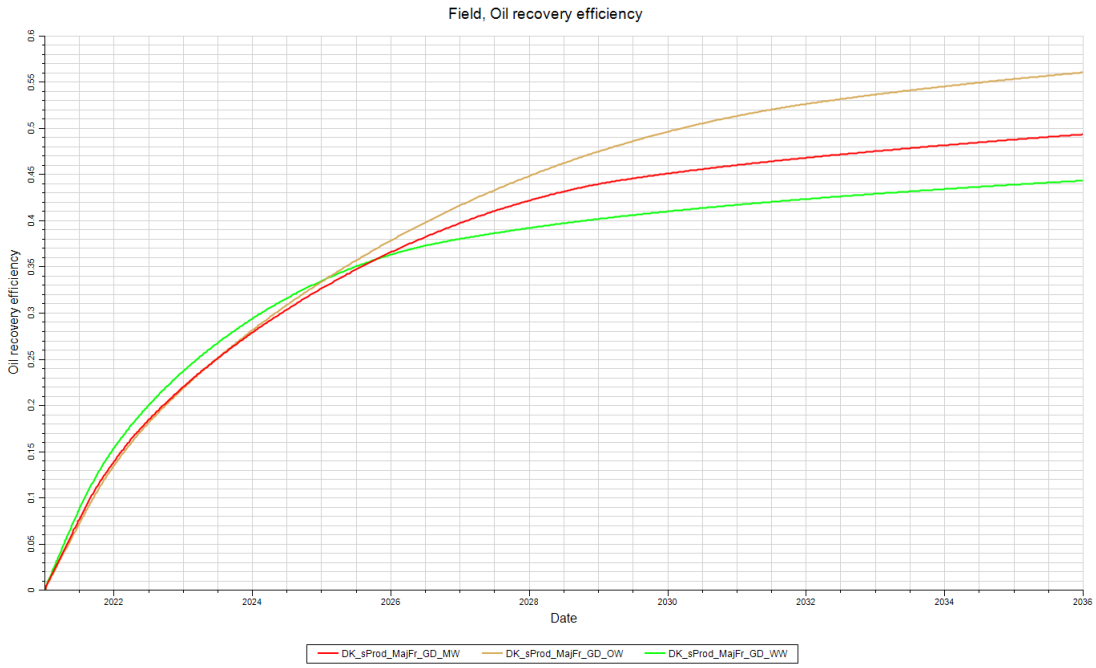

Figure 54: Wettability sensitivity runs with major fractures included for gas injection

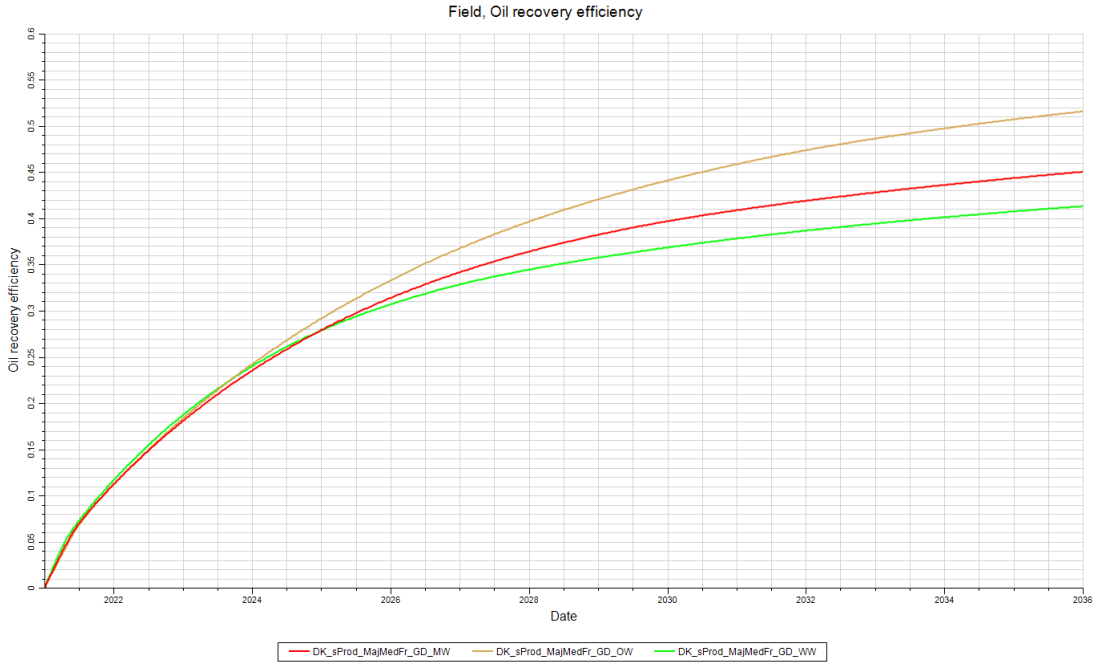

Figure 55: Wettability sensitivity runs with major and medium fractures included for gas injection

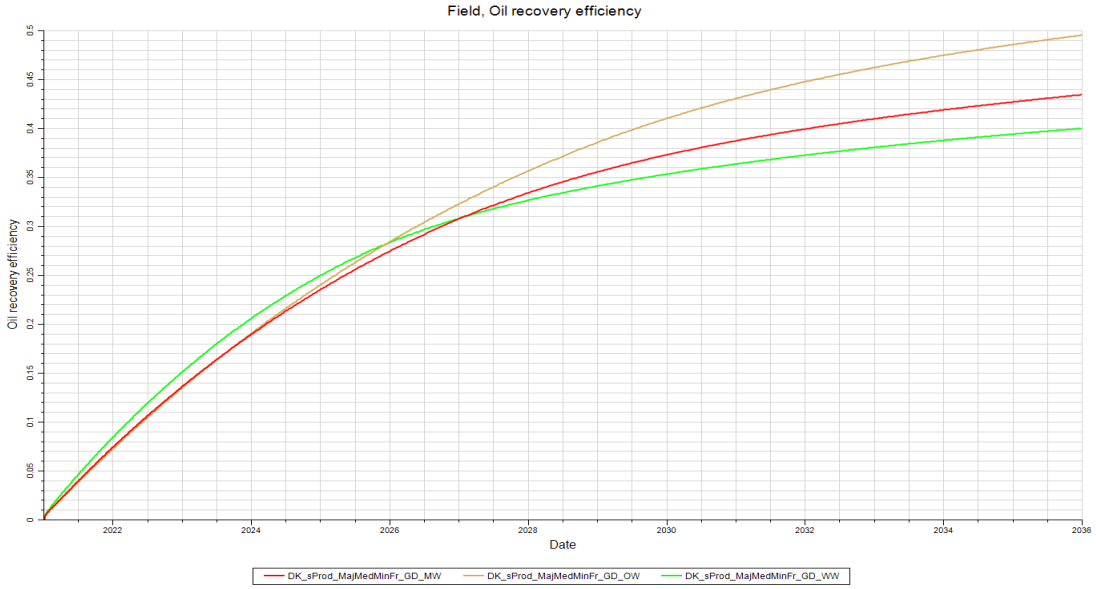

Figure 56: Wettability sensitivity runs with major, medium, and minor fractures included for gas injection

The last sensitivity parameter conducted in this work is the oil viscosity. Due to the fact that the viscosity of oil is a function of density and pressure, changes in the original GH fluid model were kept to a minimum. By changing the density of oil, the viscosity is correlated by Petrel. The original GH model features an oil density of 855kg/m^3 and an initial oil viscosity of 0.727cP. Viscosity changes that were conducted are summarized in Table 13.

Table 13: 3D cube sensitivity of the oil viscosity

Run	Parameter	Value	unit
visco0	Density	800	kg/m^3
	Viscosity	0.2377	cP
visco1	Density	847.5	kg/m^3
	Viscosity	0.46397	cP
visco2	Density	895	kg/m^3
	Viscosity	1.132	cP
visco3	Density	942.5	kg/m^3
	Viscosity	2.406	cP
visco4	Density	990	kg/m^3
	Viscosity	6.383	cP

Results are shown in Figure 57, Figure 58, and Figure 59 for different fracture type combinations. Cases with lighter oils reached higher recoveries as expected. For heavier oils, the mobility is less favorable, resulting in less ultimate recovery. Miscibility effects are not included in this work, as all cases are treated as immiscible floods.

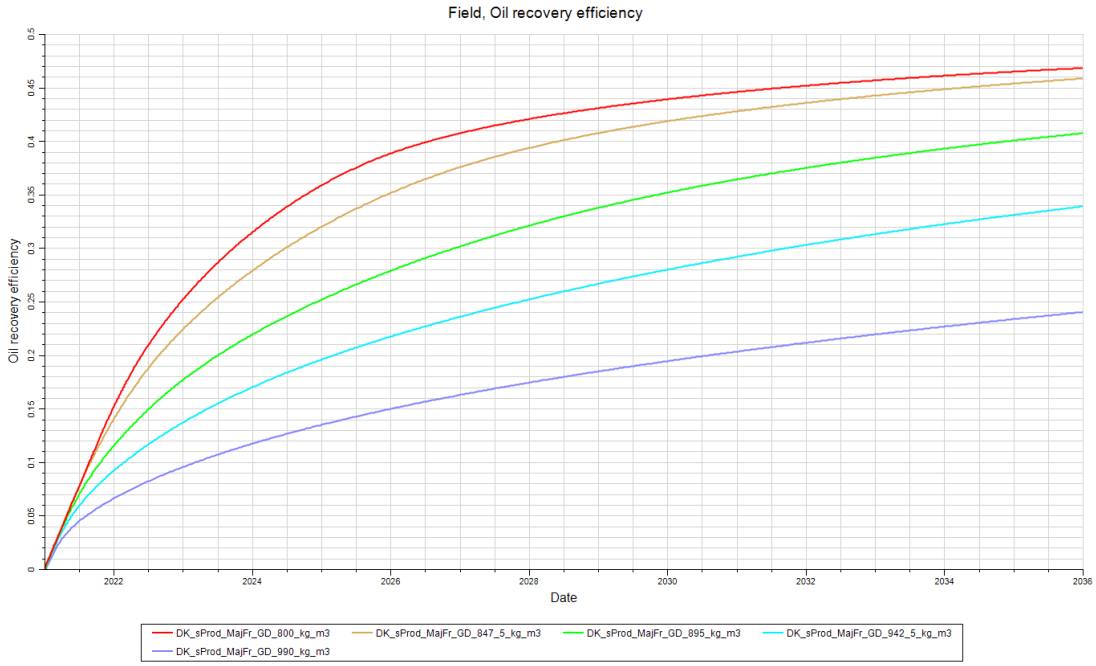

Figure 57: Gas injection viscosity sensitivity utilizing major fractures

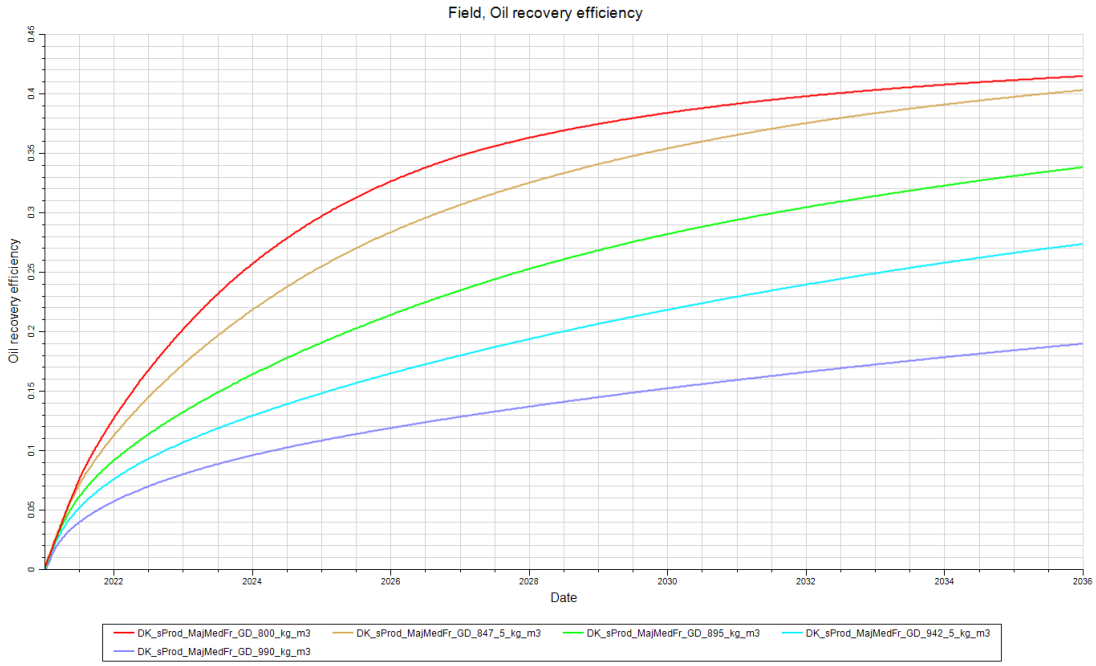

Figure 58: Gas injection viscosity sensitivity utilizing major and medium fractures

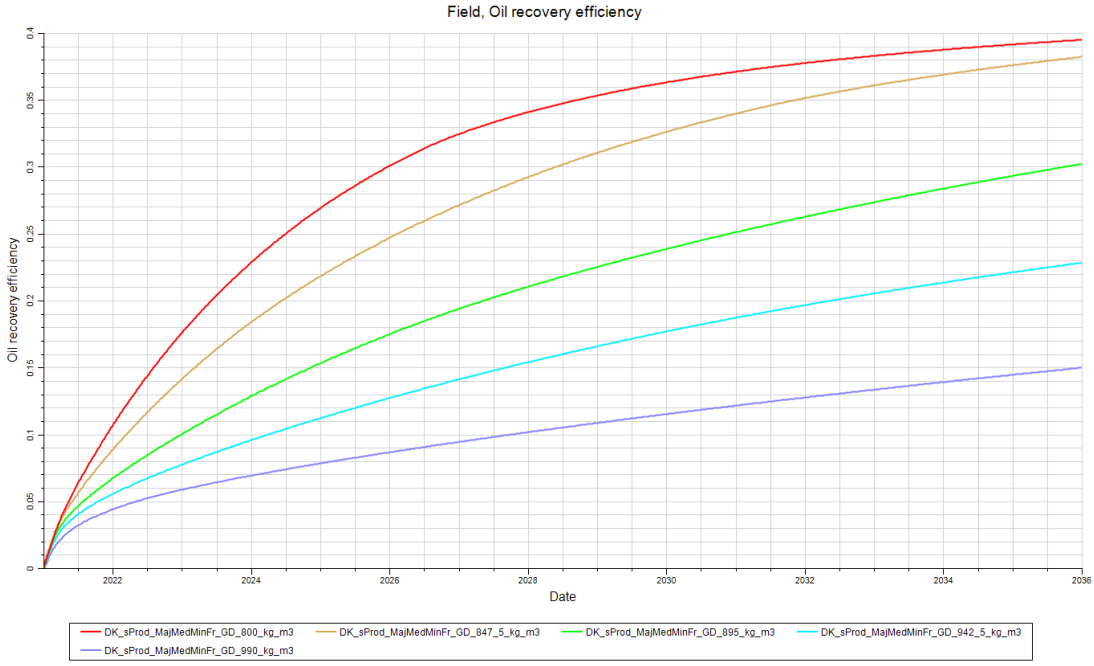

Figure 59: Gas injection viscosity sensitivity utilizing major, medium, and minor fractures

4.3.3 Secondary Production – Waterflooding

The waterflooding case was conducted by utilizing the vertical injector and producer well. The injector injects throughout 15 years approximately two pore volumes of water (0.246m^3/day), and a pressure limit of 245bar constrains the producer. The pressure limit is found after conducting sensitivity analysis and solving all non-convergence issues of the simulator.

Table 14: 3D cube waterflooding parameters

model	3D cube	
dimension XYZ	15x15x15	m
cell count XYZ	37x37x37	
recovery process	waterflooding	
SCAL	GH	
fluid model	GH	
injection rate	0.246	m^3/day
producer BHP	245	bar
well orientation	vertical	
production period	15	year

The main observation from Figure 60 is that the oil recovery curve is similar to the results from the 2D slice. The case with major, medium, and minor fractures performed best, although the difference between major and medium fractures is relatively small. This indicates that minor fractures do not affect oil production a lot. The case with major and medium fractures produced

around 10% more oil than the major fractures alone. Another increase in production is observed once the minor fractures are included, increasing the oil production by 4% compared to the case with only major and medium fractures. These results were obtained over 15 years with 2 pore volumes of water injected. Pressure is maintained to be constant, as can be seen in Figure 62. However, it is found that the waterflooding cases are more sensitive to very high drawdown pressures. For example, the same simulation cases were run for 2 years but with higher injection rates to honor the 2 pore volumes injected. The drawdown pressure was increased by reducing the bottom hole pressure limit of the producer down to 100 bar. This high drawdown pressure now results in high production rates, which enhance the fast depletion of fractures, allowing to distinguish two periods in the oil recovery curve (Figure 61). The first period consists of the steep rise of oil production at the beginning, which ends in a plateau due to the displacement of most of the oil in the fractures by water. After that, the effect of the matrix kicks in, and most recovery comes from the re-imbibition of oil from the matrix to the fractures. Another observation is that the re-imbibition is dependent on the fracture types present. The more fractures are present, the earlier the plateau starts and ends, indicating that oil is easier displaced from the matrix to the fractures. Analogically, the case with only the major fractures performed the least efficient. Once major and medium fractures are considered, the oil recovery increases by almost 10%, whereas minor fractures hardly contribute to the results. Less than 1% more ultimate recovery can be reached with major, medium, and minor fractures than with only major and medium fractures. Interestingly the numbers in percent are similar to the ones obtained with lower drawdown. This indicates that the effect introduced by the fracture types on ultimate recovery remains in a constant frame of values. For further study, the runs with 2 pore volumes over 15 years of injection were considered. Their drawdown is expected to be more reasonable for further sensitivity studies.

The water saturation for the 3 cases is shown in Figure 63, Figure 64, and Figure 65. The slices are taken from the middle layer of the 3D cube after different time steps. The injection occurs from left to right. The encroaching waterfront in the matrix blocks can be seen. The water basically utilizes the fractures to displace the oil more efficiently for the cases with more fractures introduced. The case with major, medium, and minor fractures, even after 13 years, had some oil left in the fractures, showing how the oil leaves the matrix and enters the fractures in order to be produced (Figure 65).

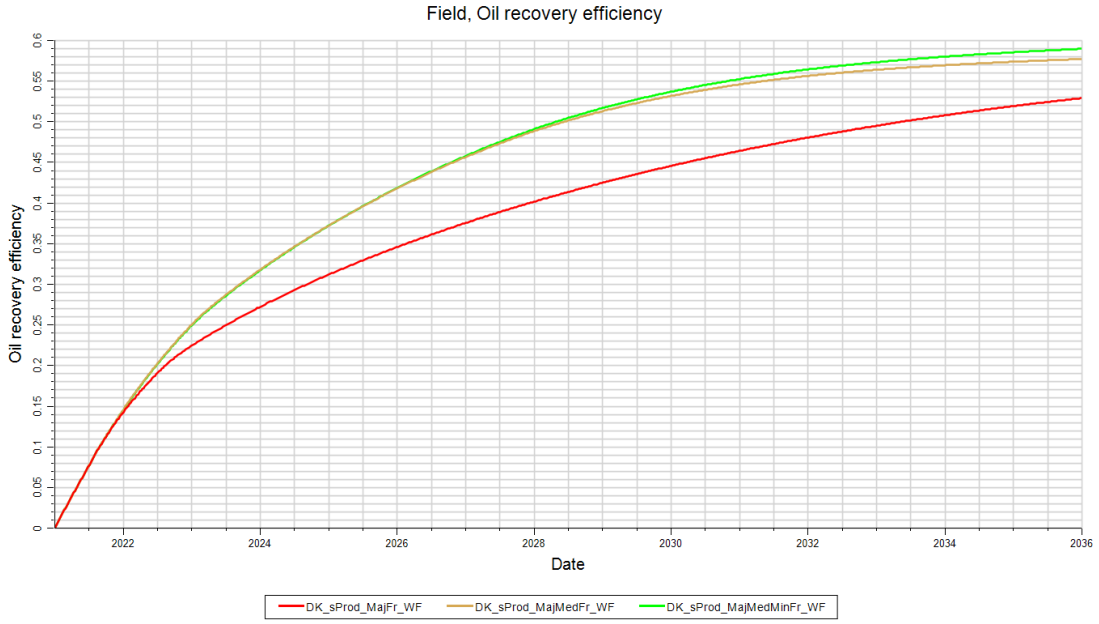

Figure 60: 3D cube after waterflooding for 15 years

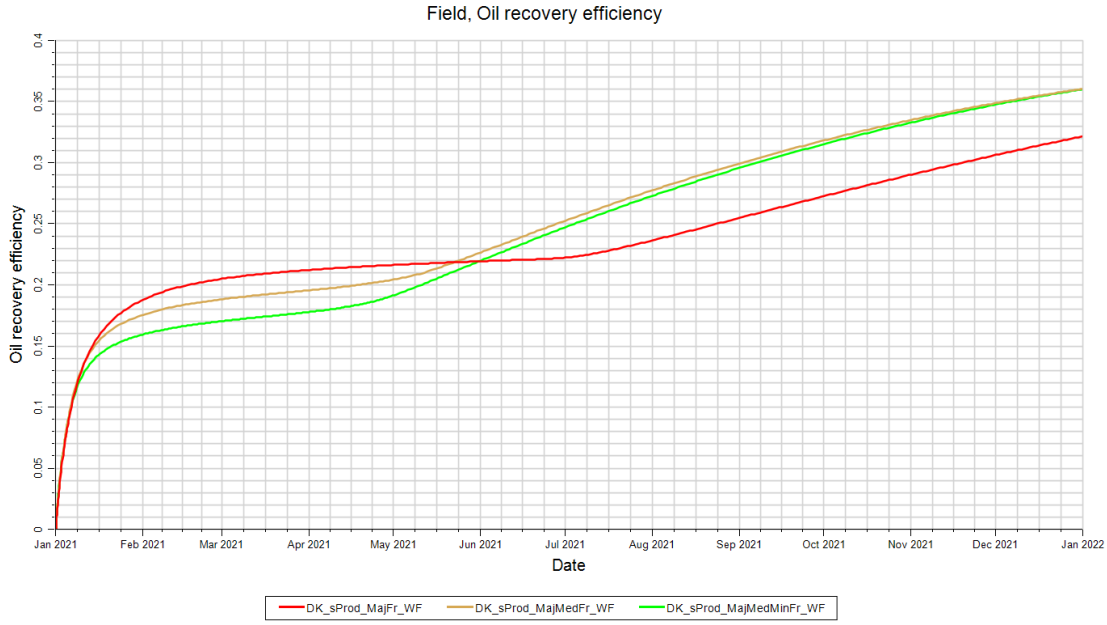

Figure 61: 3D cube after 2 years of production with very high drawdown pressure

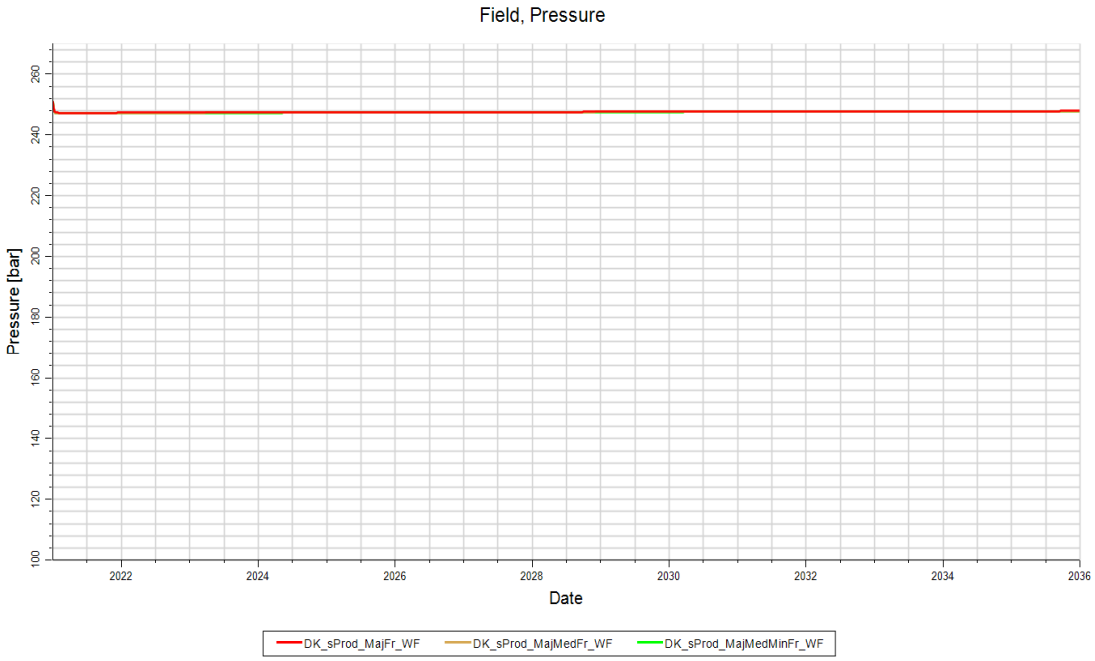

Figure 62: Constant pressure response for the three cases over 15 years

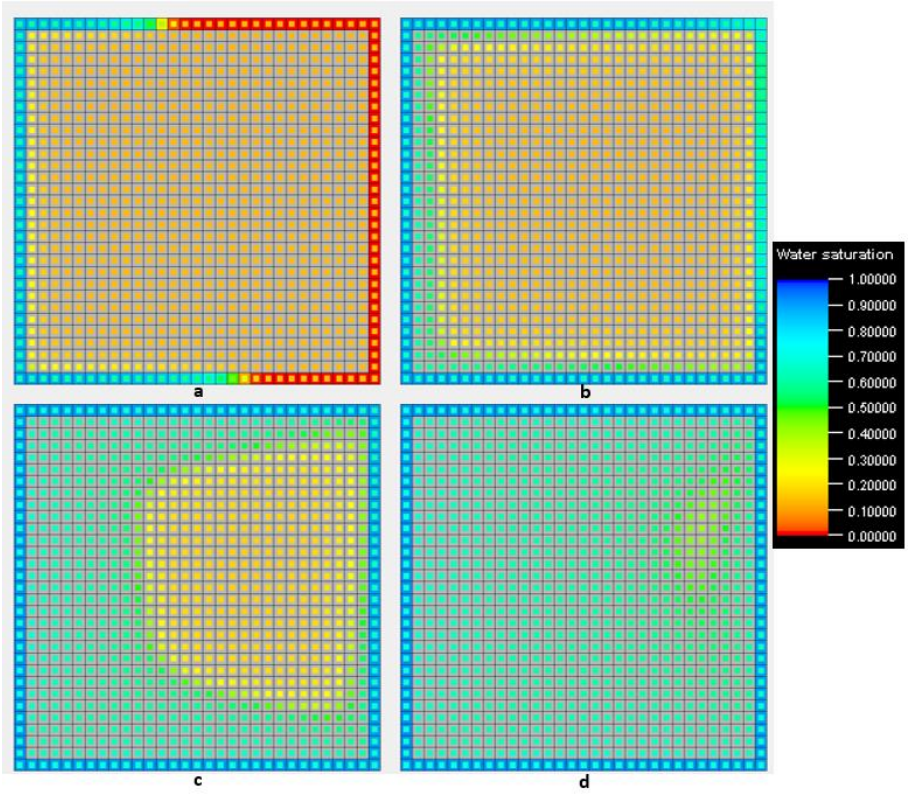

Figure 63: Water saturation for major fracture set after a) 4 months b) 18 months c) 7 years d) 13 years

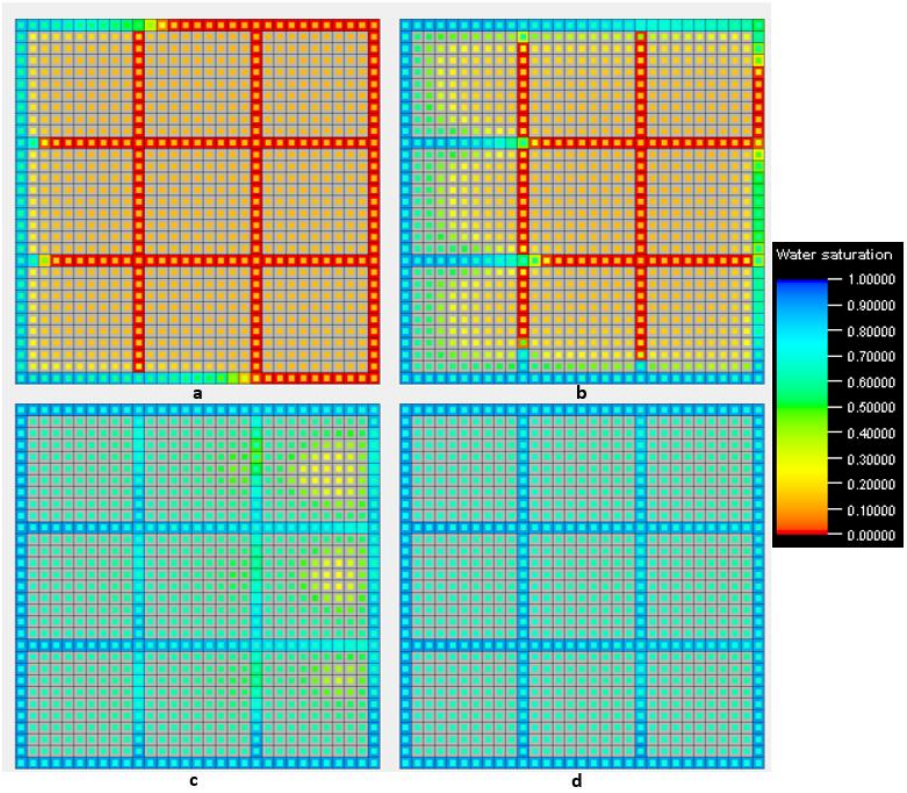

Figure 64: Water saturation for major and medium fracture set after a) 4 months b) 18 months c) 7 years d) 13 years

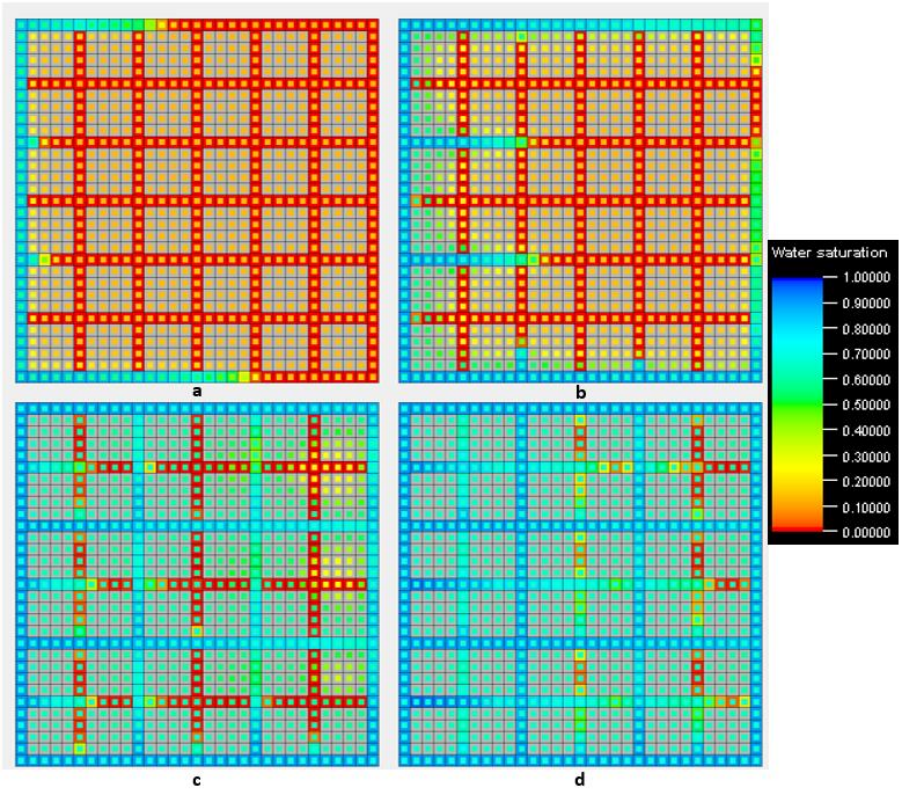

Figure 65: Water saturation for major, medium, and minor fracture set after a) 4 months b) 18 months c) 7 years d) 13 years

4.3.3.1 Sensitivity

Sensitivity runs such as fracture types, distribution of fracture types, bottom-hole pressure, wettability, and oil viscosity were obtained to study their effects on oil production.

The differences between differently distributed fracture types are more prominent during the waterflooding compared to the gas injection. The “standard” distribution performed the best (Figure 67), reaching the highest oil recovery. The “standard” distribution refers to the case where fractures from Figure 66 labeled as “a” are major fractures, “b” is medium, and “c” are minor fractures. In the case of Set 3 and Set 5, the two wells are not in direct contact with the major fractures since the major fractures are not the framing fracture type. Set 3 consists out of “a” minor, “b” medium, and “c” major fractures, whereas Set 5 is constructed as “a” minor, “b” major, and “c” medium fractures. For Set 3 and Set 5, the injector well is connected to the minor fractures, forcing the water to take the path through the matrix earlier than when the injector is directly connected to the major fracture. The displacement is much slower, promoting that the water will more likely enter the matrix. This promotes the matrix effects, resulting in better recovery at the start of production, but towards the end, the “standard” distributed fracture results in the highest ultimate recovery.

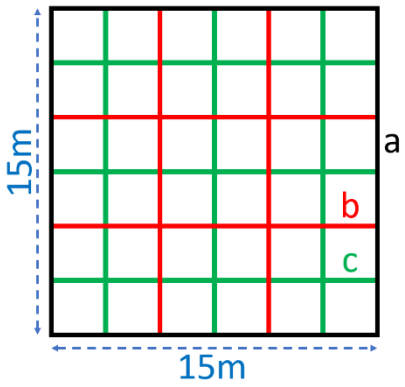

Figure 66: Distribution of fractures

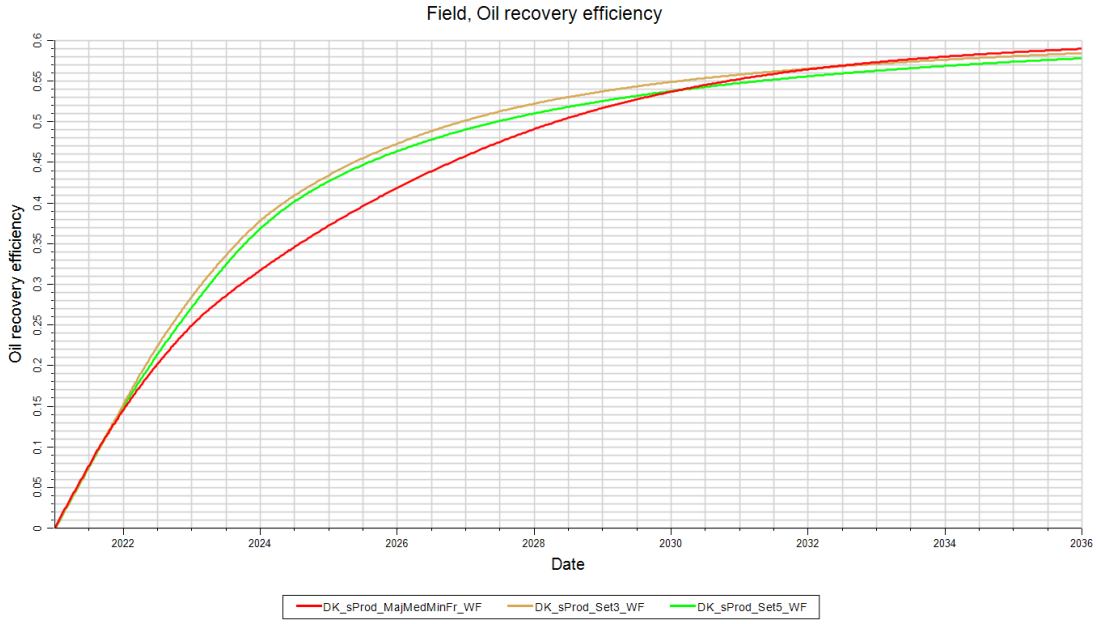

Figure 67: Differently distributed fracture sets in the 3D cube for waterflooding

To study the effects of what would happen if all fractures were major or minor, special cases for that were created. Also, different methods of running the cases were chosen, one with high production rates and high drawdown pressures, versus the other under more natural constraints (compared to the study in chapter 4.3.3 Figure 60 and Figure 61). The results from the case with high drawdown pressure and two pore volumes of water injected over a period of 2 years are shown in Figure 68. High drawdown pressure is created by lowering the minimum bottom hole pressure limit at the producer to 100 bar. The difference in behavior is significant for such high rates. In case all major fractures are considered, the displacement of the oil from the fracture is relatively fast. In nearly one month, all the oil is drained from the fractures. If more types of fractures are included, such as in the "standard" case (red color), then the plateau of production is delayed. This is interpreted as such that it took significantly longer to drain all the oil from the fractures and to activate the oil in the matrix if the plateau was delayed. However, the case with only minor fractures shows a notably slower displacement compared to the other two cases. This causes the water to fill the fractures around the matrix block but not go directly to the producer well, promoting the imbibition effects into the matrix. In Figure 69, the water saturation for these cases is shown from a middle layer from the 3D cube after 14 days of production and water injection. As already discussed, the case featuring major, medium, and minor fractures has to longest plateau in production, and at the same time, the reason for it can be seen now. The major fractures are flooded first, and then it takes some time to move the oil from the matrix towards the fractures, creating this distinctive plateau. Similarly, the case with all major fractures first flushes all the fractures, creating a steep increase in recovery followed

by a short plateau. However, because all the fractures, in this case, are major fractures, it flushes more fractures at the initial stage. The matrix oil is activated faster than the major, medium, and minor fracture cases, but not as fast as with only minor fractures. If only minor fractures are considered, then almost piston-like displacement is reached after 14 days of production. The minor fractures do not show the classical fracture-like fast decline of production. Minor fractures, in this case, almost behave like the matrix. For lower drawdown, the same case was run with a minimum pressure limit of the producer at 245bar for 15 years.

The injected pore volumes remain constant with 2 years. Now the injection and production rates are significantly lower, allowing the case with all minor fractures to perform the best. In Figure 70, the oil recovery efficiency of the three cases is shown. Figure 71 represents how effective the case with all minor fractures is. The displacement of the oil is almost perfectly piston-like. The two other cases produced similar amounts of oil after 15 years. However, a simulation case over a longer period of time would lead to all major fractures being the least efficient. All major fractures force the injected water to follow the fractures, leading to a breakthrough earlier than the other two cases.

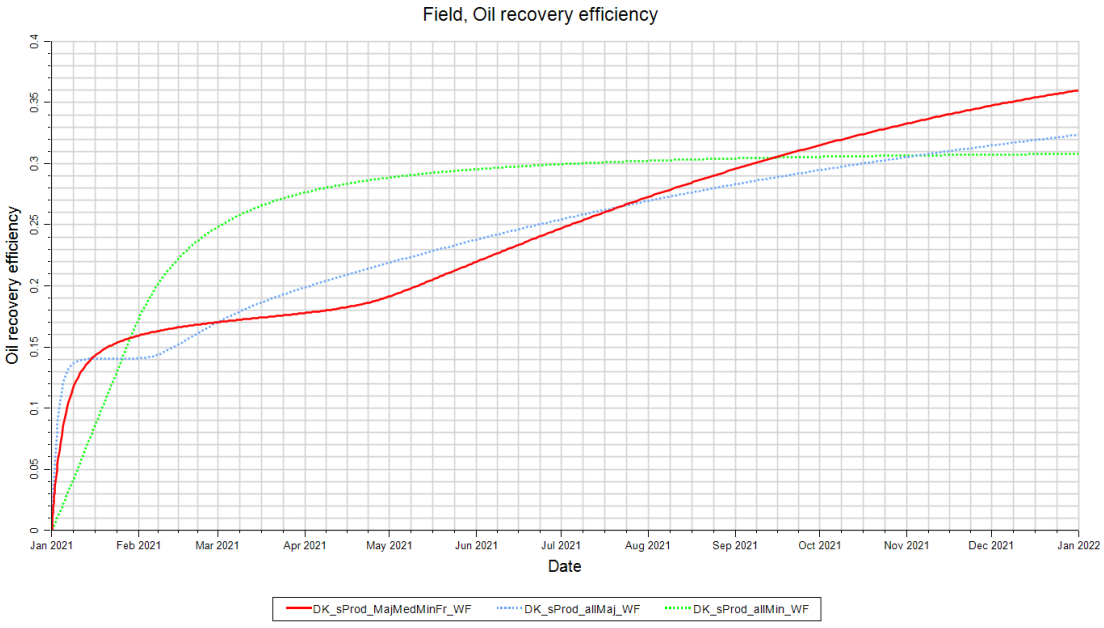

Figure 68: Oil recovery efficiency comparison between the standard case and all fractures minor/major over 2 years with high drawdown

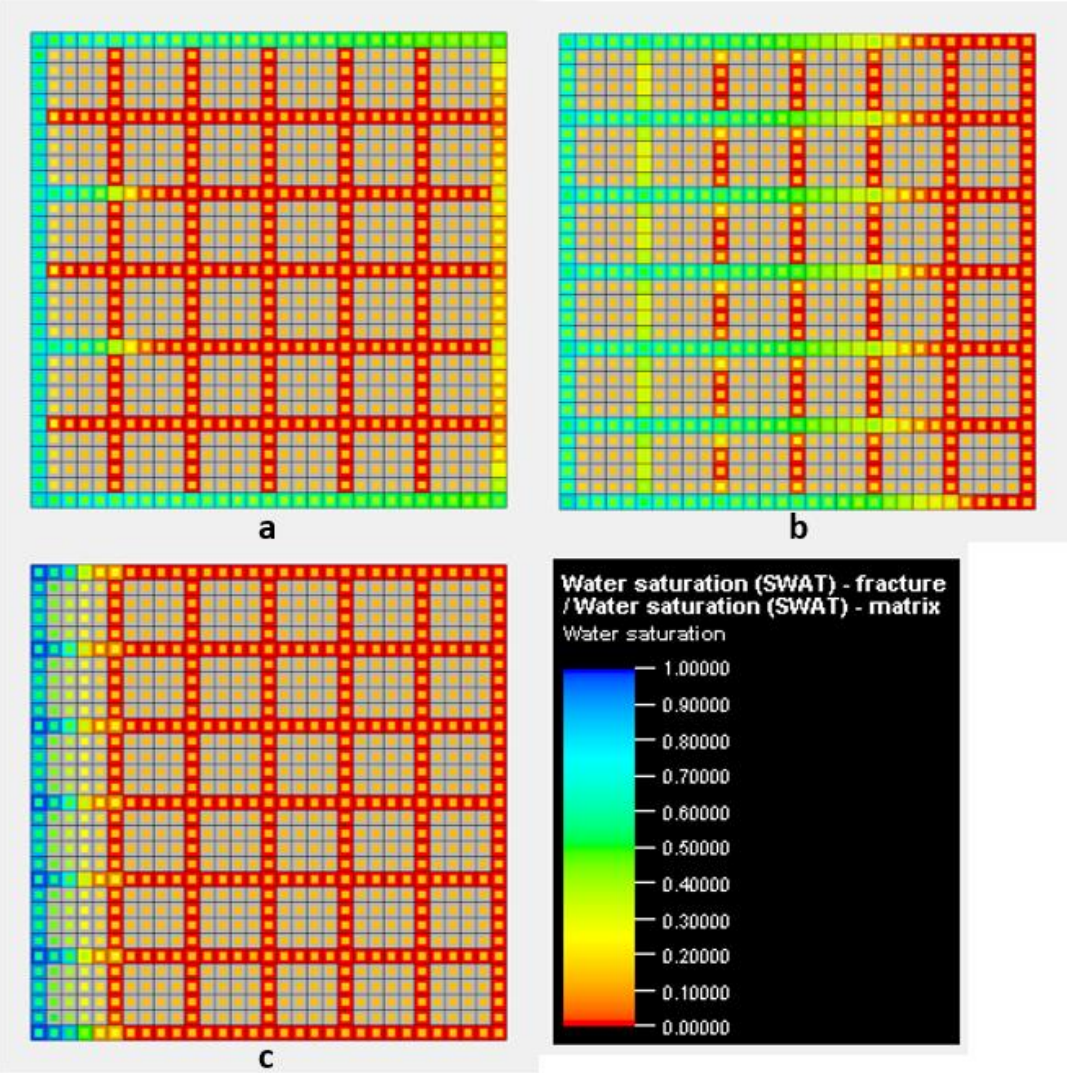

Figure 69: Water saturation in a middle layer from the 3D cube for different cases after 14 days of production (high drawdown): a) "standard" case with major, medium, and minor fractures b) all fractures major c) all fractures minor.

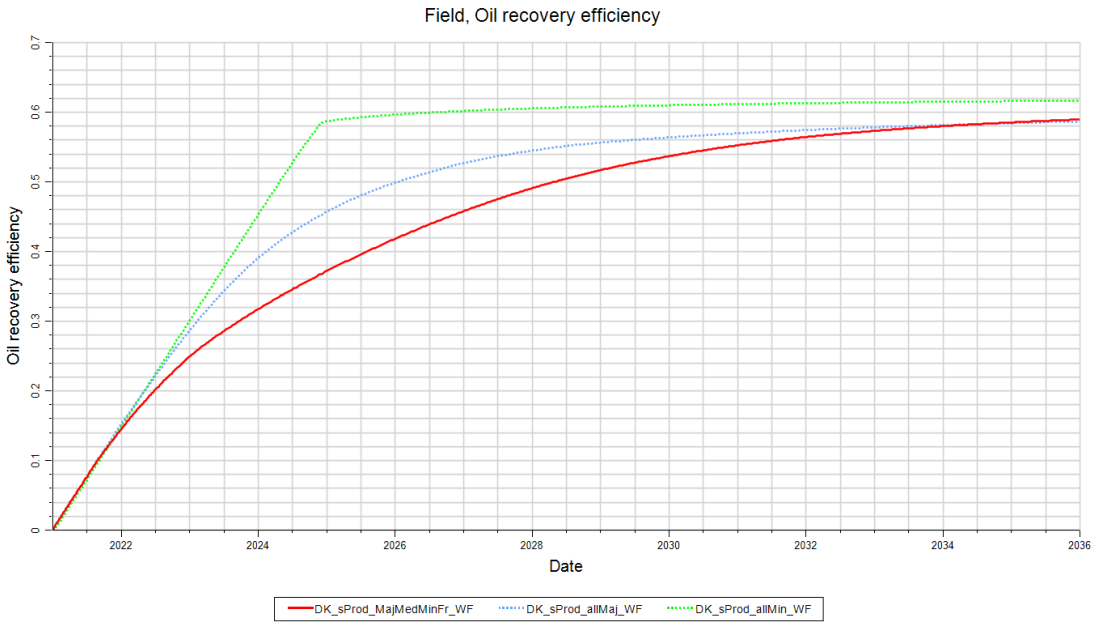

Figure 70: Oil recovery efficiency comparison between the standard case and all fractures minor/major over 15 years

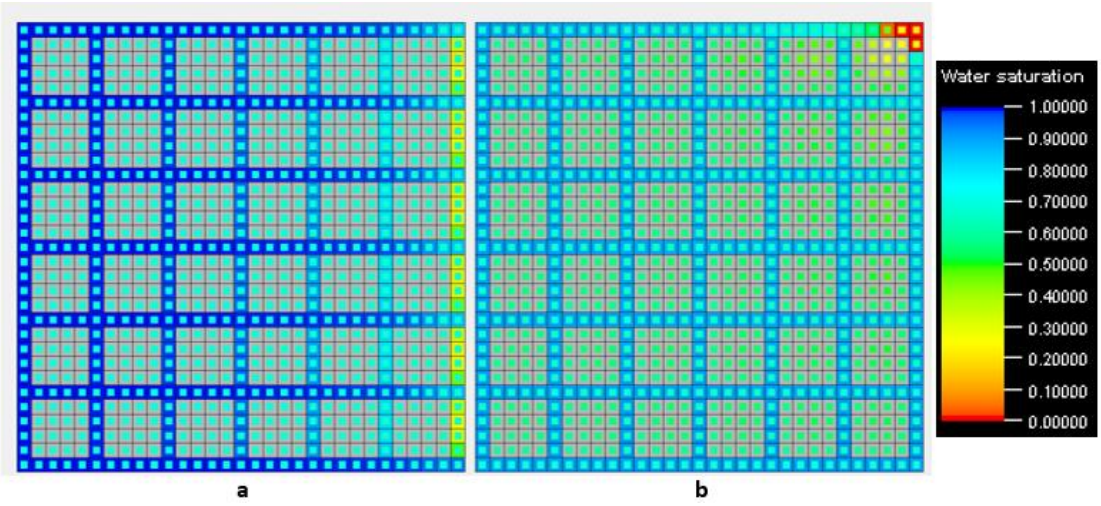

Figure 71: Water saturation after 7 years of waterflooding for a) all minor fractures b) all major fractures

In order to verify the observed trend of oil displacement through the matrix towards the fracture, a sensitivity run was conducted under different bottom hole pressure (BHP) limits of the producer. Changing the lower limit of the BHP for the producer well governs the production rate, which in turn impacts oil production. The following sensitivity study was conducted using the "standard" cases (chapter 4.3.3 Figure 60) for each fracture type as base cases for 5 different bottom hole pressures (BHP) ranging from 145bar up to 225bar (Table 15). In Figure 72, Figure 73, and Figure 74, the results of this sensitivity study are presented. Simulation cases with lower BHPs performed less good. This is expected because lower BHP means higher drawdown,

which enhances earlier breakthrough of water and less matrix governed flow. This can be seen for all fracture types; low BHPs resulted in steep slopes in the early years. These steep slopes indicate the displacement from oil from the fractures, after which a short plateau in production may follow, especially for the low BHP Case_1 in Figure 74. For direct comparison of the BHP sensitivity results, the red dotted curve in each figure represents the corresponding "standard" case from chapter 4.3.3, Figure 60. These obtained results from the BHP sensitivity runs were used for the dimensionless number calculation.

Table 15: 3D cube waterflooding sensitivity of the BHP for the producer

Sensitivity case	BHP constraint of producer
[…]_Case_1	145bar
[…]_Case_2	165 bar
[…]_Case_3	185 bar
[…]_Case_4	205 bar
[…]_Case_5	225 bar

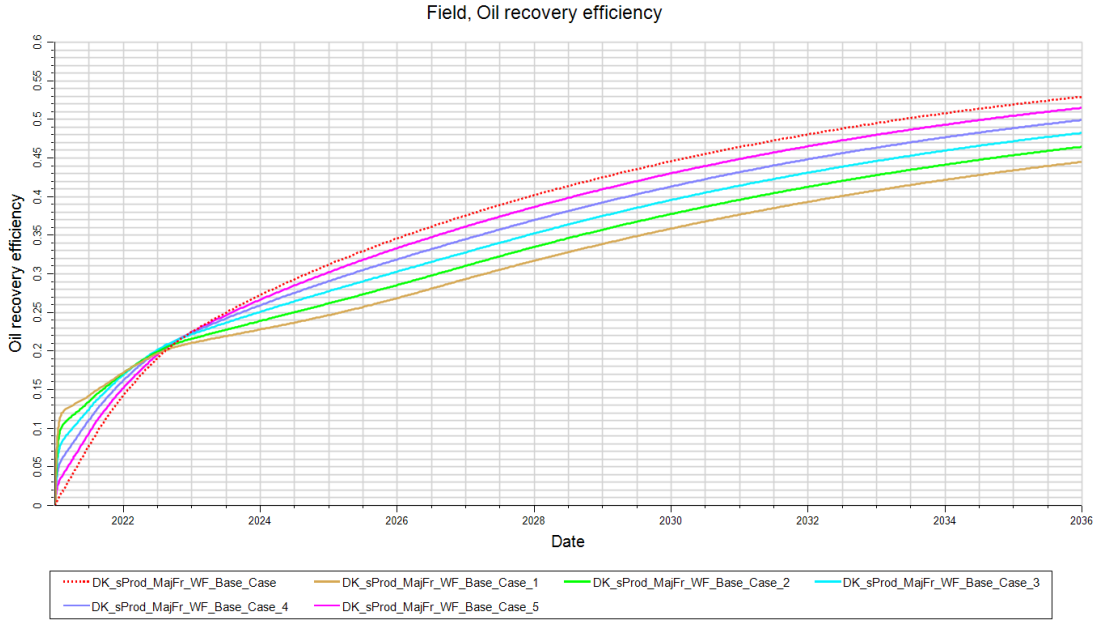

Figure 72: BHP sensitivity runs with major fractures included

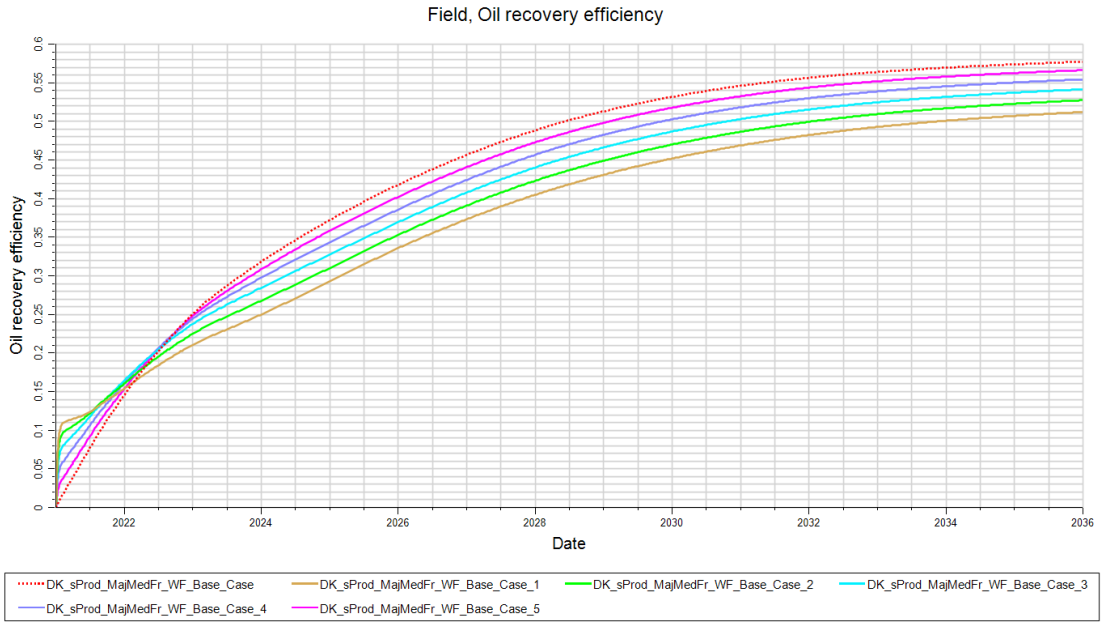

Figure 73: BHP sensitivity runs with major and medium fractures included

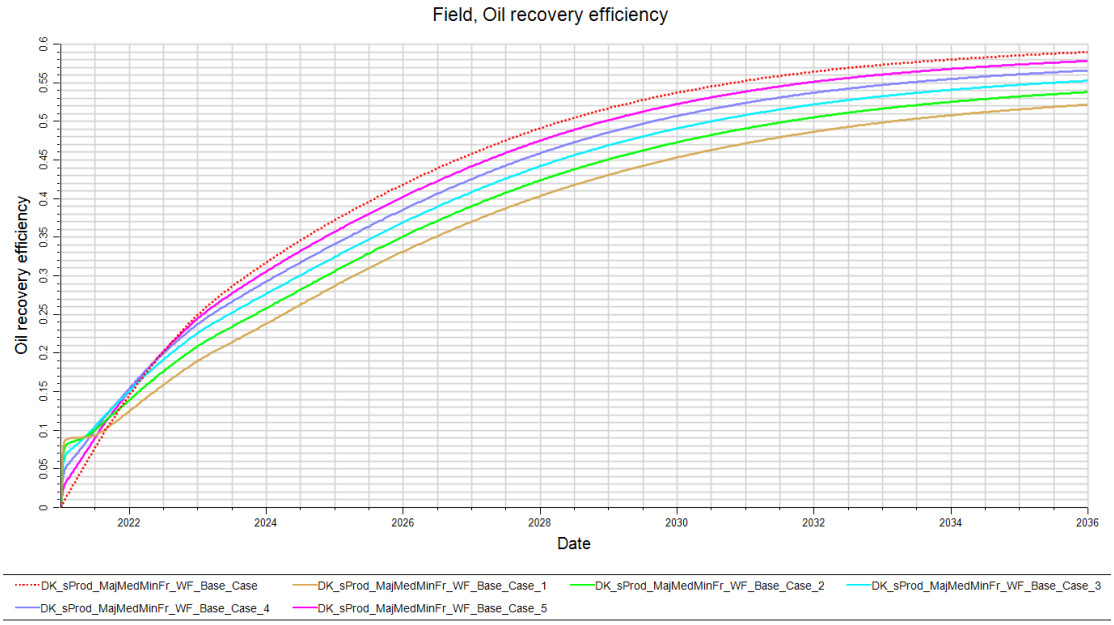

Figure 74: BHP sensitivity runs with major, medium, and minor fractures included

The initial GH SCAL data used so far in all simulations represent a mixed-wet rock type, slightly tipping towards oil-wetness. To study the effects of different wettability conditions, optimized synthetic SCAL data was implemented in simulation cases. These results may, in a later step, be used for the calculation of dimensionless numbers. Due to totally different SCAL data from the GH, a direct comparison of results with the “standard” cases is not recommended. However, a comparison between the different wettability runs can be made to study the effects of the fractures. The results obtained are presented in Figure 75, Figure 76, and Figure 77. The

WW cases initially reached higher recoveries compared to OW or MW conditions. However, the differences are small, and for the cases with more fracture types combined after approximately 5 years, a common point for all wettability conditions is reached. The highest ultimate recovery is achieved under mixed-wet conditions, although the contribution of fracture types changes. Under MW conditions, major+medium fractures resulted in a 9% recovery increase compared to major fractures alone. Another 3% increase is observed if major+medium+minor fractures are considered and compared to the major+medium mixed-wet case. For the water-wet case, fewer notable changes were observed. Introduction of medium fractures combined with major fractures increased recovery by 3.5% compared to major fractures alone. Another increase of 2.5% if minor fractures are included could be observed, indicating that the contribution of minor fractures to ultimate recovery is rather small. In general, for WW conditions, the introduction of different fracture types brought less effect in ultimate recovery than for MW conditions. For an oil-wet rock, major+medium fractures performed 13% better than major fractures alone. This is significantly more than for the water-wet case. Major+medium+minor fractures under OW conditions resulted in a 4% increase, compared to major+medium fractures. From this study, one can conclude that with increasing water-wetness, the difference in fracture contribution diminishes.

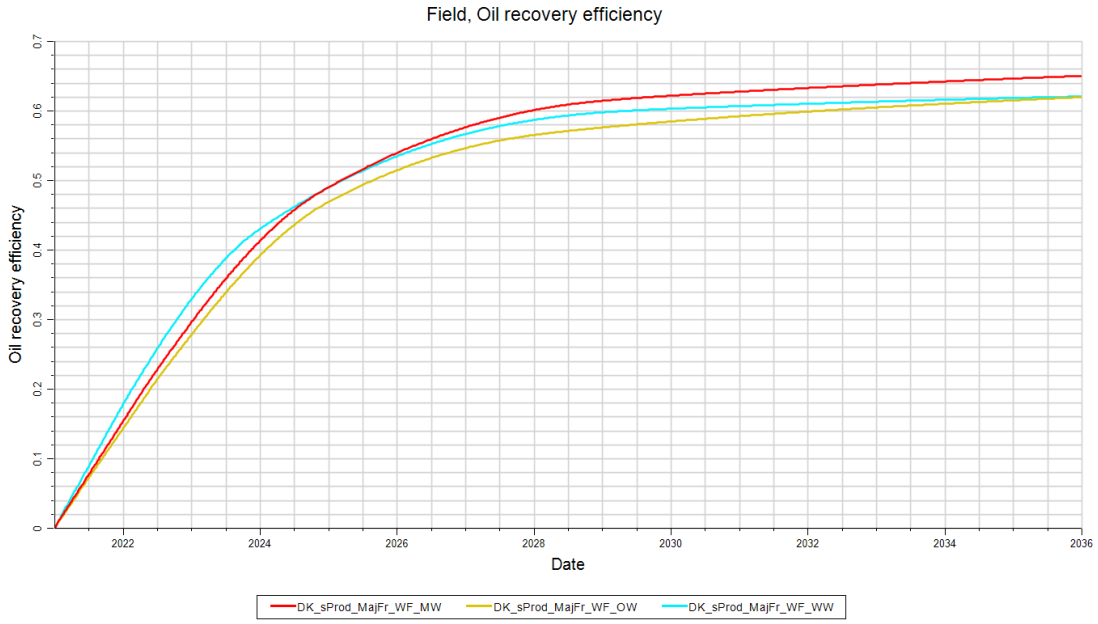

Figure 75: Wettability sensitivity runs with major fractures included

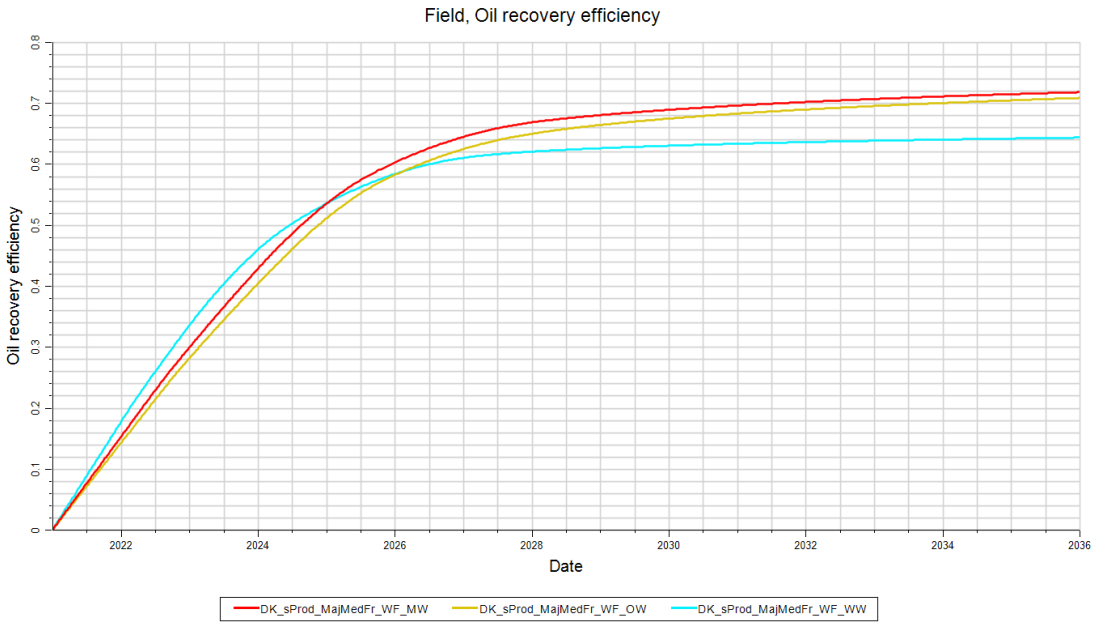

Figure 76: Wettability sensitivity runs with major and medium fractures included

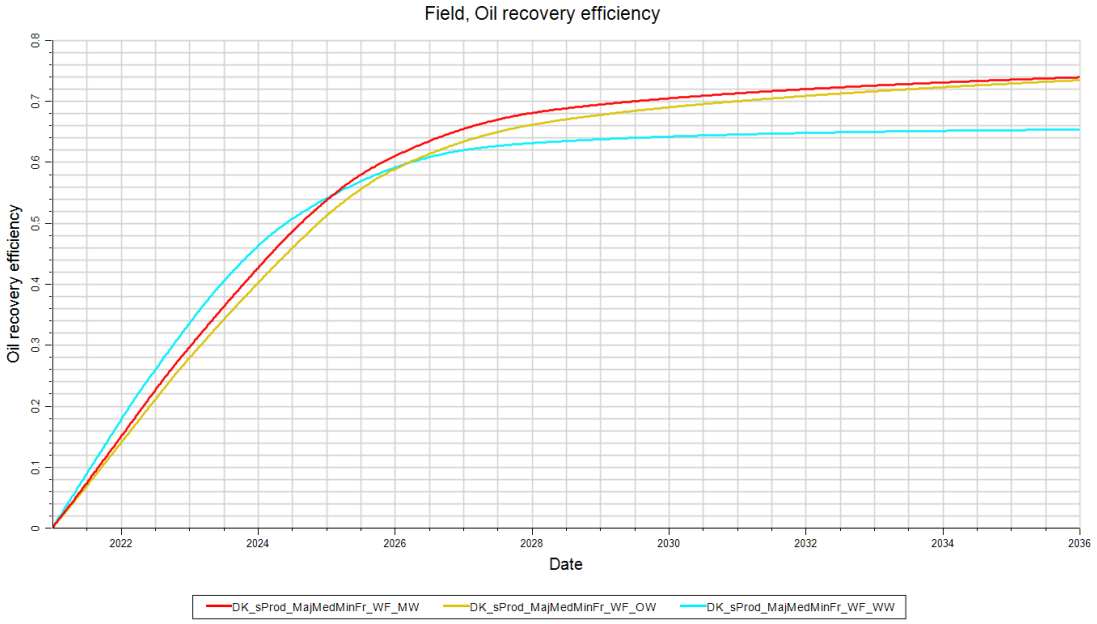

Figure 77: Wettability sensitivity runs with major, medium, and minor fractures included

The synthetic SCAL data used in this wettability sensitivity study are illustrated in Figure 78, Figure 79, Figure 80, and Figure 81.

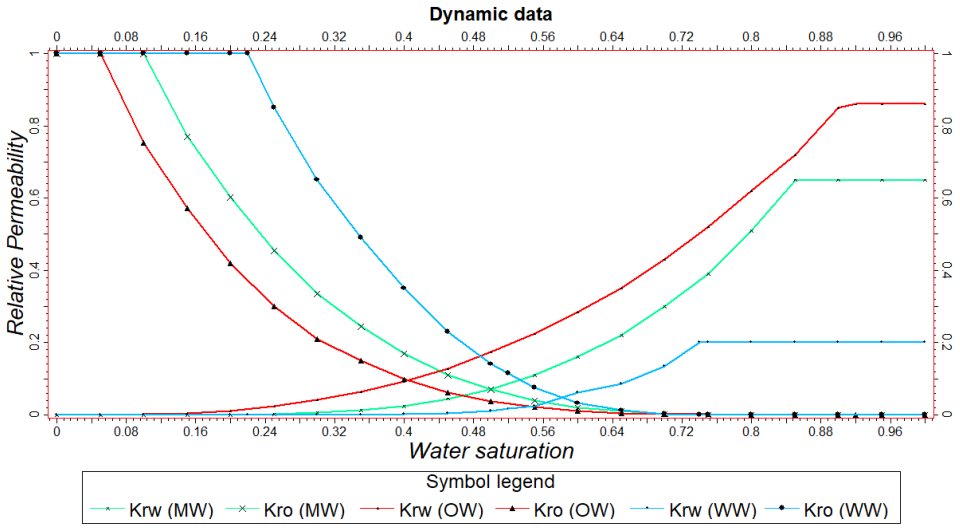

Figure 78: Synthetic water-oil relative permeability curves

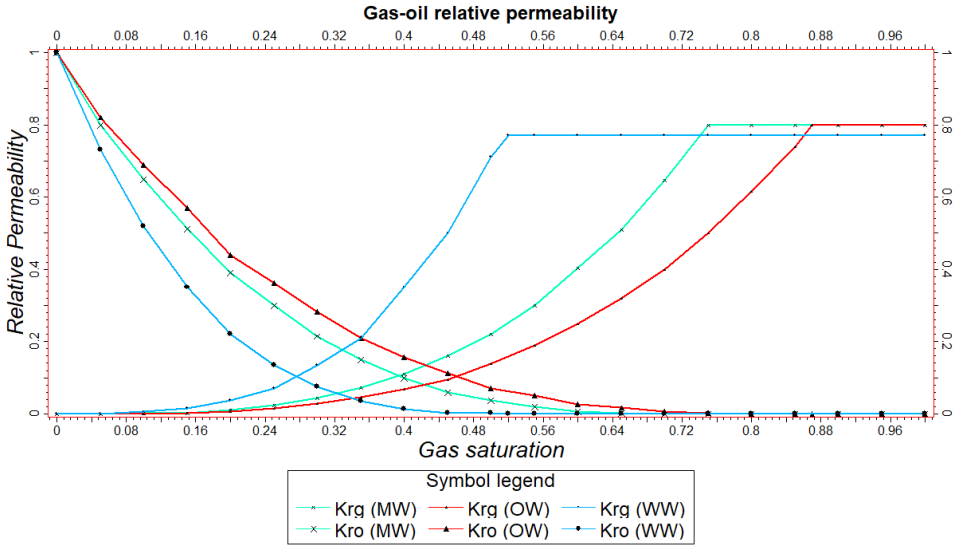

Figure 79: Synthetic gas-oil relative permeability curves

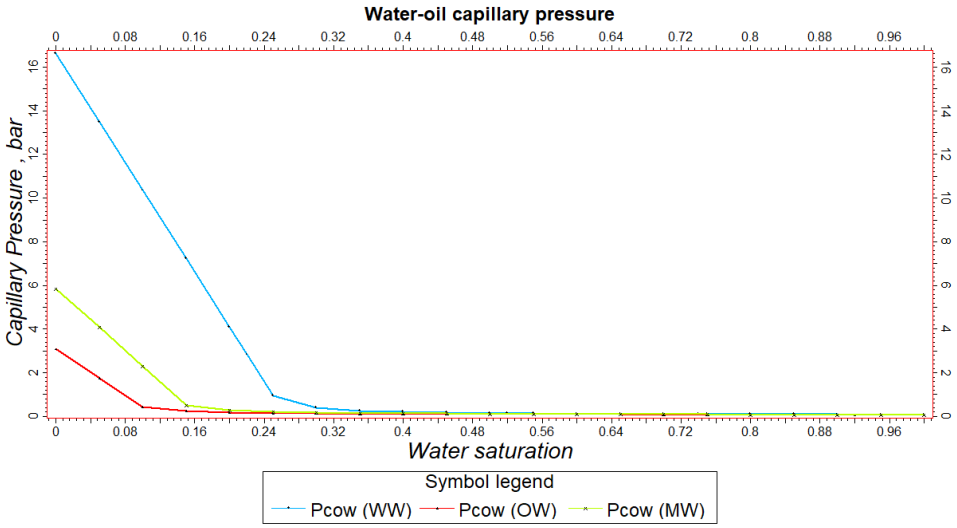

Figure 80: Synthetic water-oil capillary pressure

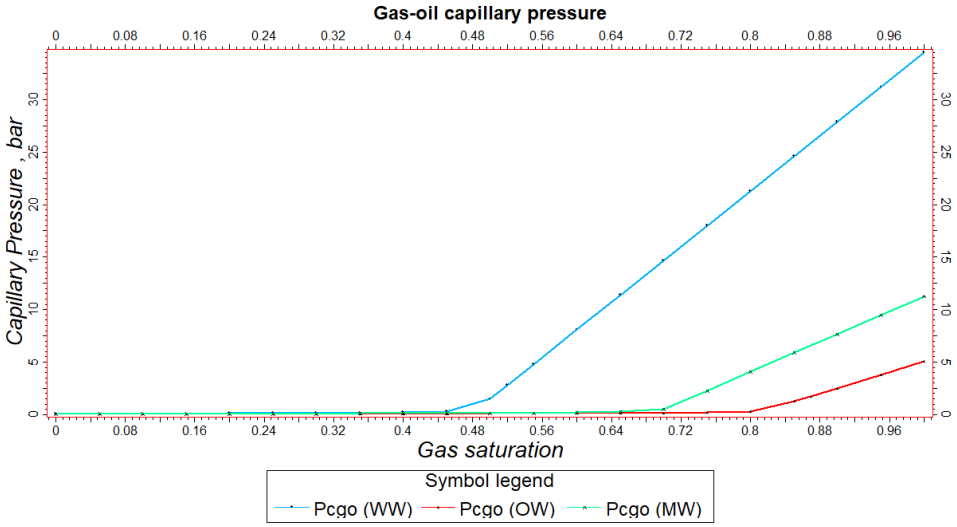

Figure 81: Synthetic gas-oil capillary pressure

For the viscosity-related sensitivity study, changes in the fluid model had to be done. As was already discussed in the section about the gas injection (chapter 4.3.2.1), the changes in the fluid model were kept to a minimum to keep data as close as possible to the GH data. The sensitivity study of viscosity for the waterflooding scheme uses the same fluid model as the gas injection sensitivity study. The density and viscosity values published in Table 16 were used for the sensitivity runs. The results (Figure 82, Figure 83, and Figure 84) are as expected; for more viscous oil, the recovery is decreased. All these figures include one dotted reference line,

representing the “standard” run with GH fluid properties and serves as a direct comparison. These obtained results are used for dimensionless number calculation.

Table 16: 3D cube waterflooding sensitivity of the oil viscosity

Run	Parameter	Value	unit
visco0	Density	800	kg/m^3
	Viscosity	0.2377	cP
visco1	Density	847.5	kg/m^3
	Viscosity	0.46397	cP
visco2	Density	895	kg/m^3
	Viscosity	1.132	cP
visco3	Density	942.5	kg/m^3
	Viscosity	2.406	cP
visco4	Density	990	kg/m^3
	Viscosity	6.383	cP

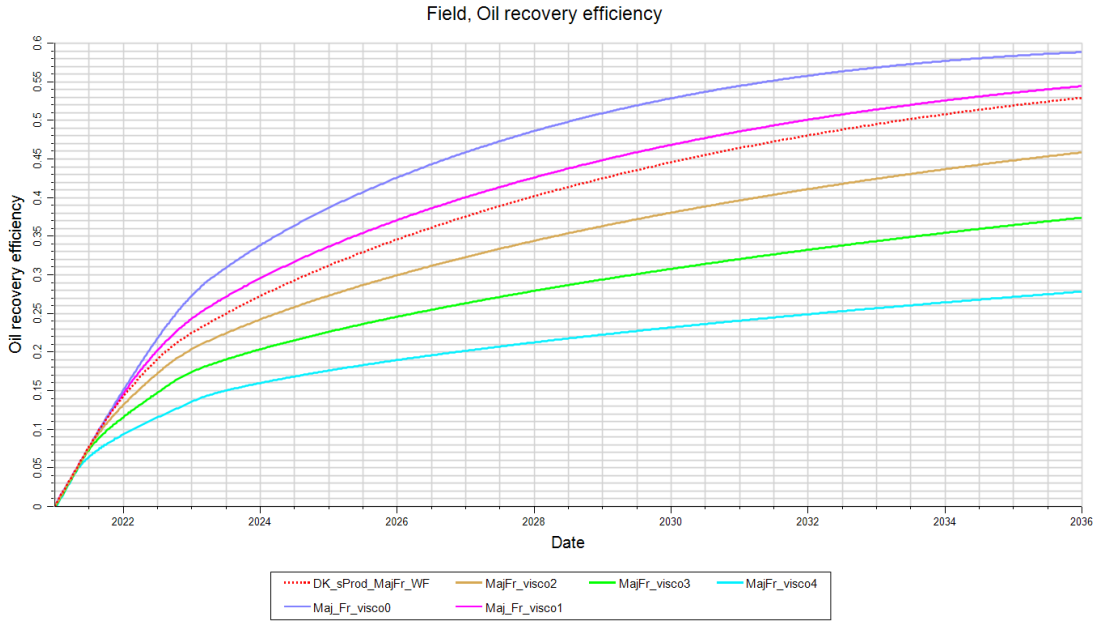

Figure 82: 3D waterflooding viscosity sensitivity utilizing major fractures

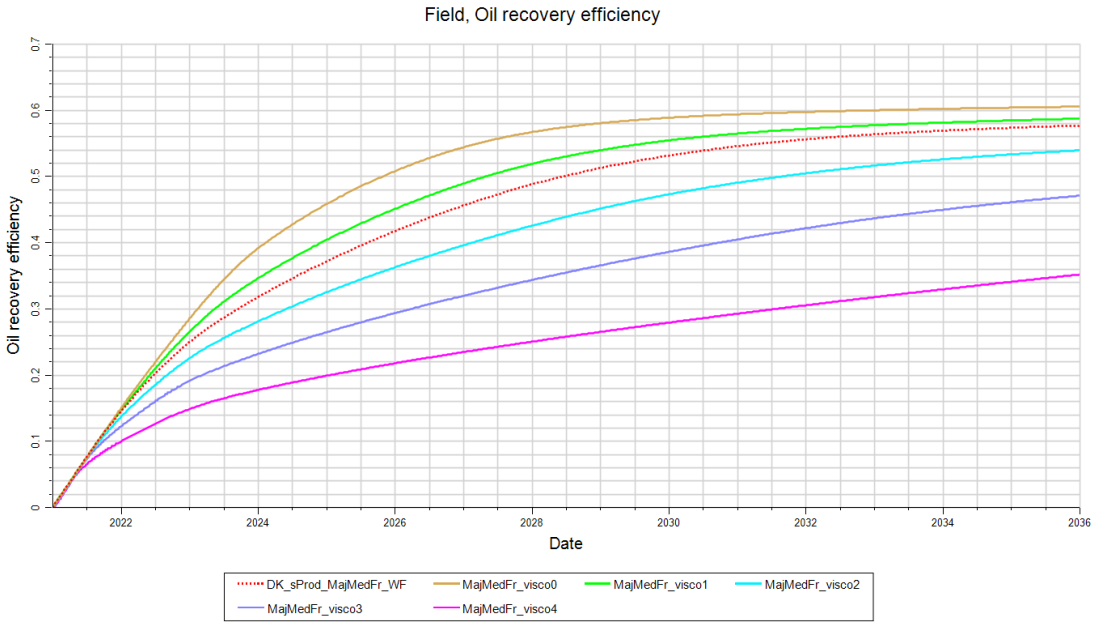

Figure 83: 3D waterflooding viscosity sensitivity utilizing major and medium fractures

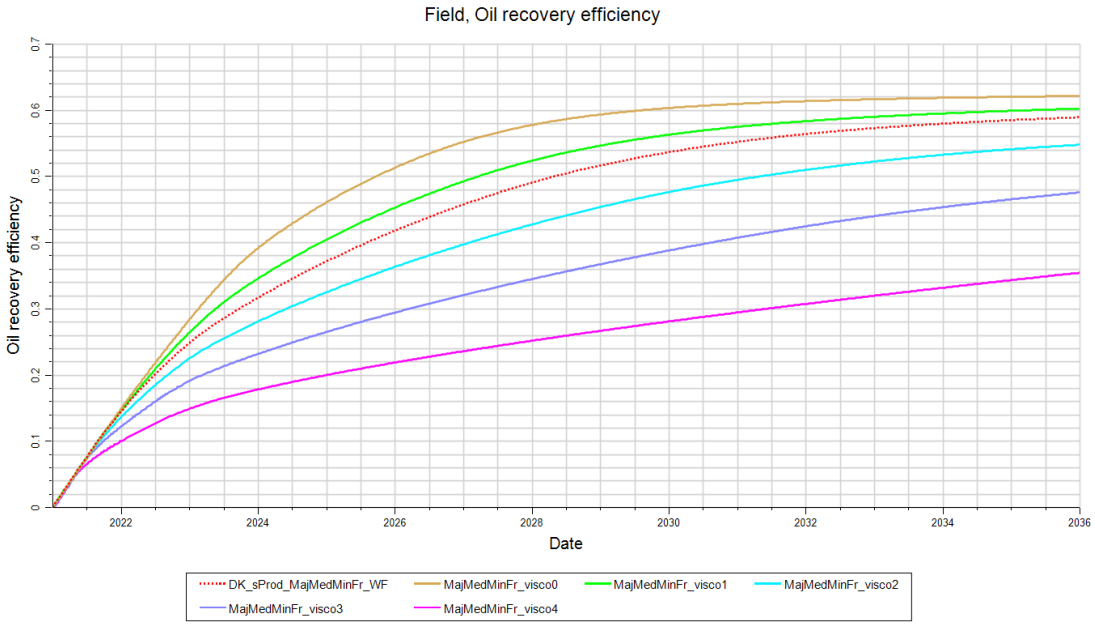

Figure 84: 3D waterflooding viscosity sensitivity utilizing major, medium, and minor fractures

4.4 Prototype model

The Prototype model refers to a certain sector showed in Figure 85 from the GH-field. Production in this sector started in the early 1960s, and good production data was documented up to the 2010s. For the GH-field, including our sector of the Prototype model, a functional history match exists for production rates and pressures. In Figure 86, a detailed view of the Prototype model is taken from different angles. The Prototype sector spans as an anticline from the northeast towards the southwest direction.

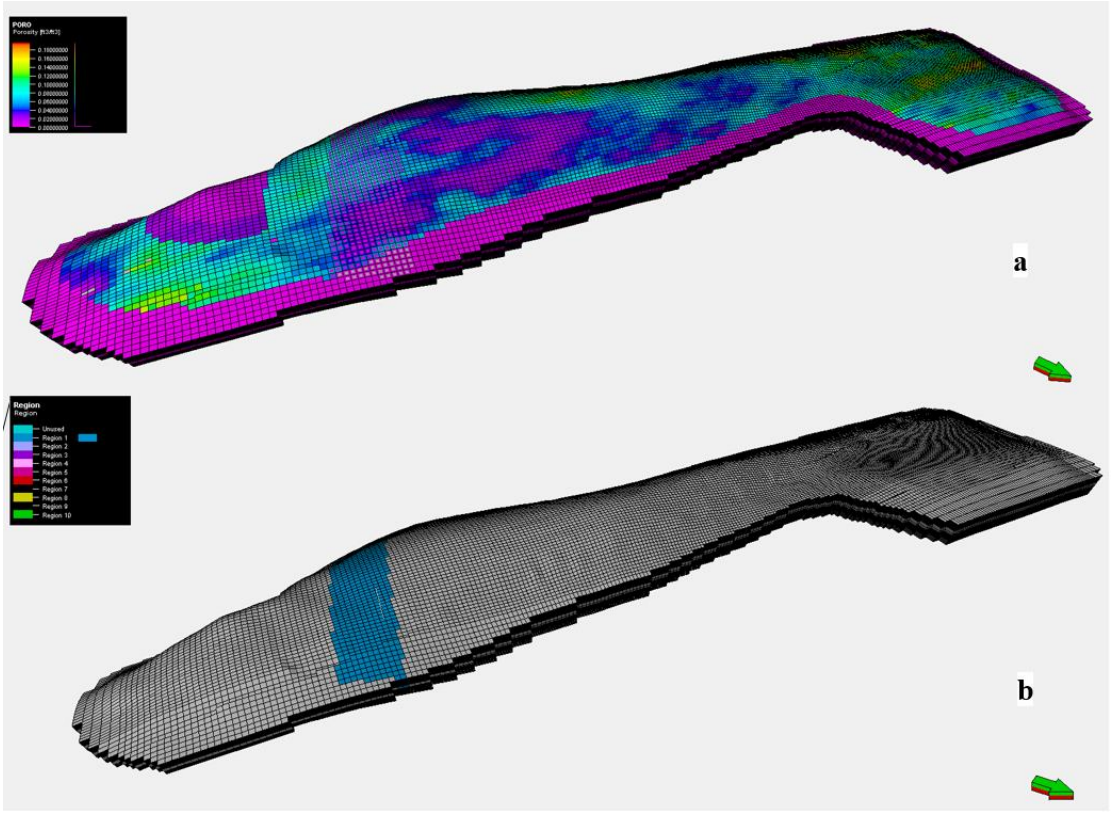

Figure 85: a) Porosity distribution in the GH field b) Prototype sector marked in blue color

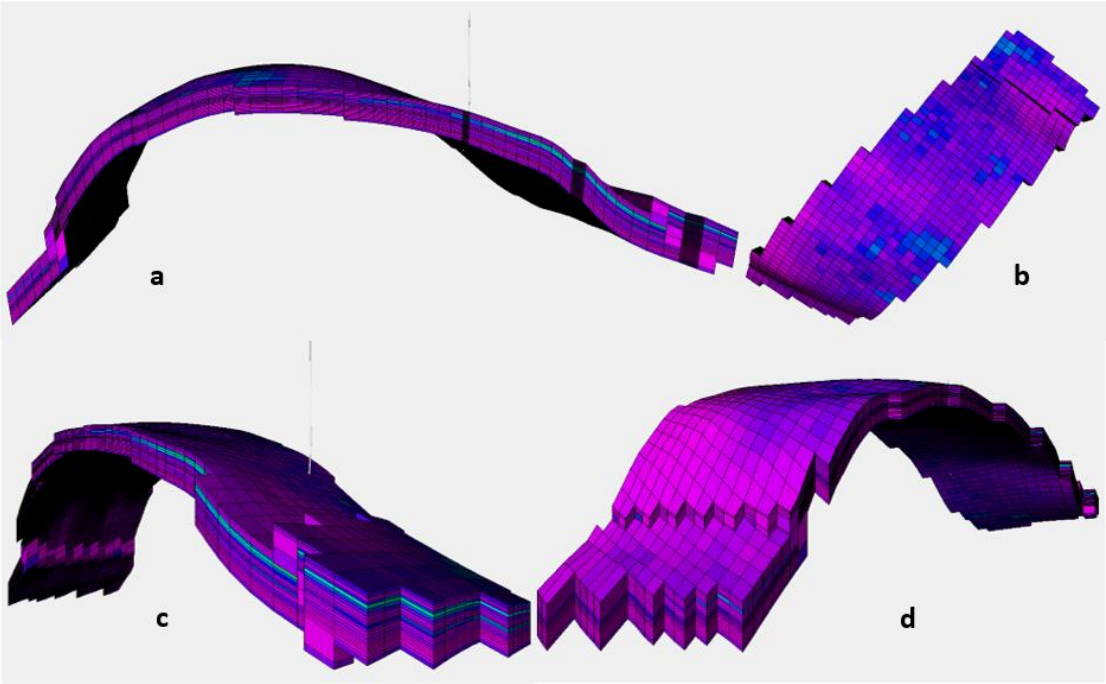

Figure 86: Prototype model from different points of view, taken from a) South b) Top c) East d) South-east

4.4.1 Fracture characterization of the GH field

The GH field is a naturally fractured carbonate reservoir, and as such, it is naturally heterogeneous. Natural fractures are the result of tectonic stresses and can be oriented horizontally and vertically. However, natural vertical fractures are more often observed than horizontal ones. High overburden stress seals the horizontal fractures again in many places if no propping agent can keep them open. In any case, both can be registered and measured by formation image logs. Most Important is that open fractures can be differentiated from closed or filled fractures. In this simulation study, only the open fractures will be classified into specific fracture groups, whereas the closed or filled fractures are considered to be the matrix. Furthermore, open fractures can have positive and negative impacts on production. In general, fractures promote production, creating high permeable highways through the reservoir, but they can also promote early breakthrough or coning effects (Kharrat, 2021).

In the GH field, borehole image logs such as FMI, STAR, UBI, and CAST were used to help determine and characterize the fractures. Natural fractures result from tectonic stresses, so analyzing stress maps is important to resolve where more detailed fracture measurements should be conducted. Tensile-based induced fractures occur in the direction of maximum stresses, whereas breakouts are expected perpendicular to the maximum stress. Information that can be interpreted from image logs are open, filled, or closed fractures, fracture dip and azimuth,

fracture intensity, and fracture spacing. Such image log runs were conducted on 44 wells across the GH field, although interpreted results were recovered from 29 wells (Kharrat, 2021).

One of the tools used for image logging the boreholes is Schlumberger's Formation Micro-Imager (FMI), which can measure the resistivity of fractures. Fractures appear as lines on the FMI images, and their state (open or filled) interpretation can be made via resistivity. Open fractures can be very conductive due to invasion of drilling mud. If calcite or anhydrite fill fractures, then more resistive responses are captured by the FMI log. Nevertheless, a good geological understanding is essential for interpreting FMI logs because other materials such as clay can also fill up fractures and create conductive responses on the measuring device. Such clay-filled fractures can create resistivity responses similar to those of open fractures, which they are not. Different methods can be utilized to validate responses and check if supposedly measured open fractures are open or not. Core analysis, seismic interpretation, or mud loss data are available methods for studying the GH field. Once open fractures are found and verified, they are usually further classified into subgroups. For example, discontinuous open or possible open fractures exist, and their implementation in the model has to be prepared. Because there are too many interpreted open fracture types in the GH field, and based on the fact that this work aims to study the impact of fractures on production, 4 fracture categories for the simulation work were defined based on the fracture's aperture. These 4 open fracture types include major fractures, medium fractures, minor fractures, and hairline fractures. The average aperture size of these fracture types is given in Table 17. All other closed fracture types were not considered since their impact on production is minimal at best (Kharrat, 2021).

Table 17: Fracture properties of each type

Fracture type	Avg. aperture size [μm]
Major	600
Medium	400
Minor	200
Hairline	10

Once all fractures of importance are interpreted, they can be set up for fracture modeling in simulation work. The goal is to implement a Discrete Fracture Network (DFN) in the simulation software. Once the DFN is set up, it includes all the fractures as planes considering fracture properties such as permeability and aperture. To create a DFN, a functional Continuous Fracture Network (CFN) model is required as an input. The CFN combines the information

from the image logs using the Gaussian Random Function Simulation algorithm into a 3D model. The DFN can be created, consisting of all the fracture planes in 3D space (Kharrat, 2021). One DFN can be constructed out of one or more fracture sets, creating multiple DFN's with different fracture type combinations. This is an essential feature of this work, to be able to directly compare results from the same model with different combinations of fractures. The impact of each fracture type can be studied like this. The following fracture type combinations of interest in multiple DFN's were included:

- All fracture DFN, including major, medium, minor, and hairline fractures
- MajMedMin DFN, including major, medium, and minor fractures
- MajMed DFN, including major and medium fractures
- Maj DFN, including only the major fractures.

After the DFN creation, fracture property upscaling had to be conducted. This step is done in Petrel, and it results in grid properties that can be used in simulation cases for dual-permeability cases. Examples of grid properties created through upscaling for each DFN separate are fracture permeability in X, Y, and Z direction, fracture porosity, and the shape factor sigma. Furthermore, as was found with the synthetic models, dual-porosity is not optimal for this purpose due to difficulties between matrix grid cell connection with the fracture grid cell connection, as was already discussed in Chapter 4.

4.4.2 Simulation Properties

As part of the GH field, the Prototype model uses the GH fluid model and SCAL data cropped to only the sector of interest. The fluid model is a black oil fluid model and was already presented in chapter 3.3. The SCAL data consists out of 9 curve sets in total. Four sets of curves were used for the imbibition relative permeabilities; another set of 4 curves is used for the drainage relative permeabilities. The 9^{th} set is used for drainage and imbibition relative permeabilities for the fractures. All SCAL curves can be found in Appendix A.

The generated fracture properties from the DFN are shown in Figure 87, Figure 88, Figure 89, and Figure 90. In these figures, the sub-plot a) refers to the fracture permeability in X-direction, b) in Y-direction, c) in Z-direction, and d) to the fracture porosity. Differences between the DFN can be seen; the general trend is that the more fracture sets are included, the wider the distribution of permeabilities is. Interestingly, the permeability distribution of the MajMedMin-DFN is the same as for the allFr-DFN. Differences are very delicate in the porosity distribution, allowing at an early stage to expect similar results from these two DFN's. On the other hand, the matrix properties were kept constant for all simulation runs in the Prototype model. Figure

91 shows the matrix properties used in this work. The same properties were also used in the past to history match this sector in the GH field.

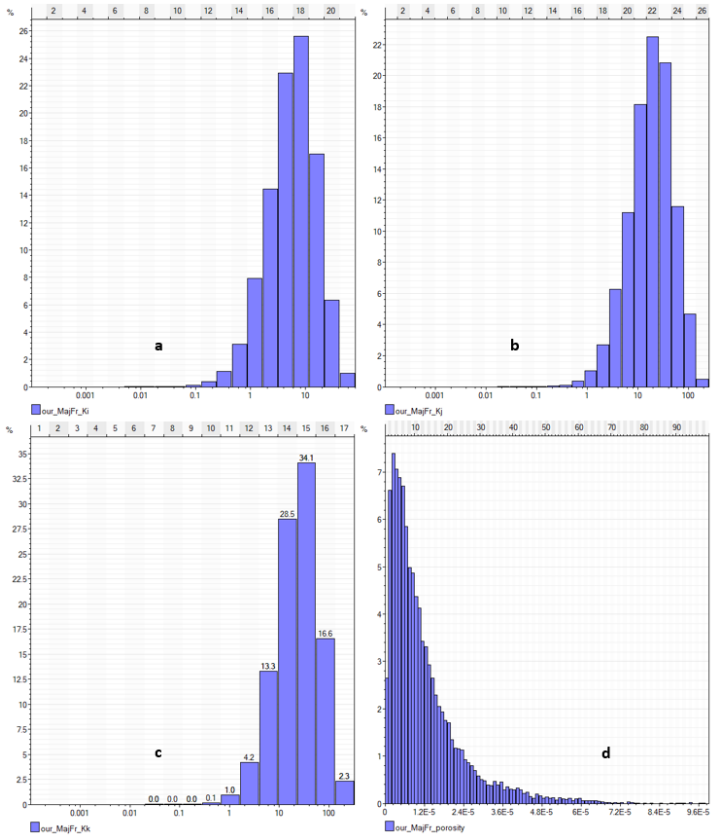

Figure 87: Major fracture properties histogram after upscaling

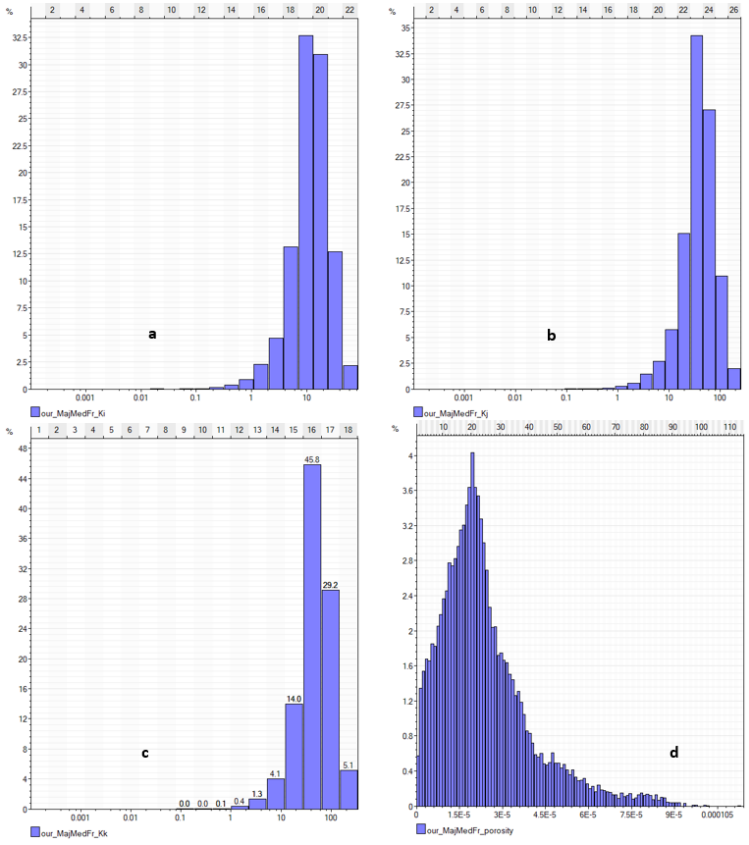

Figure 88: Major and medium fracture properties histogram after upscaling

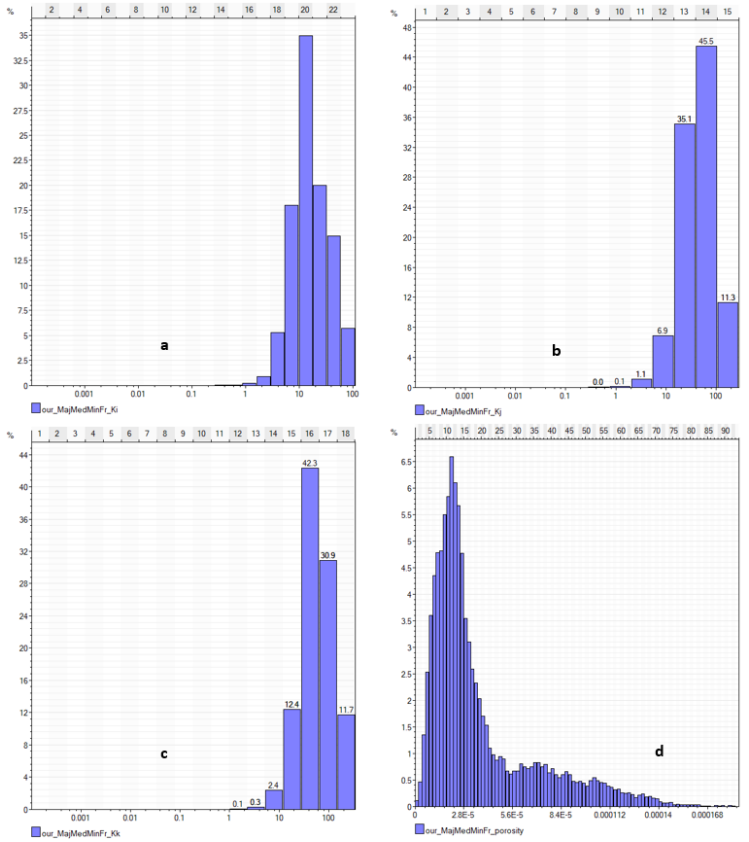

Figure 89: Major, medium and minor fracture properties histogram after upscaling

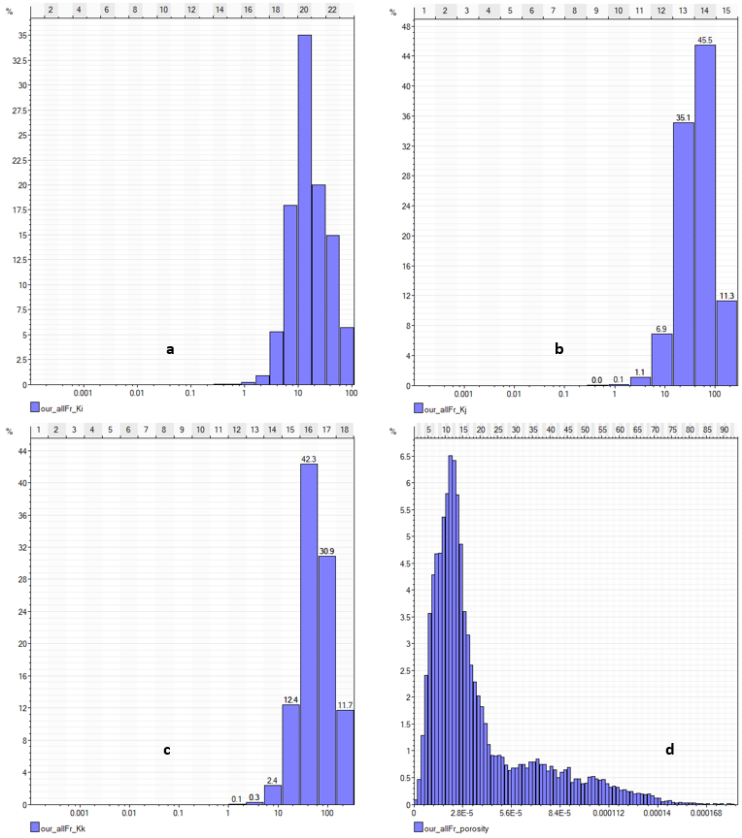

Figure 90: Major, medium, minor and hairline fracture properties histogram after upscaling

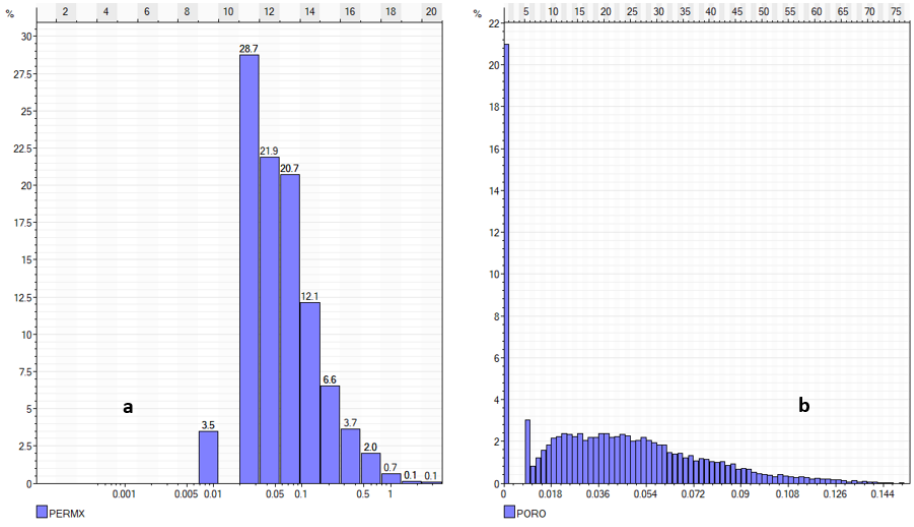

Figure 91: Matrix properties used in the Prototype model

4.4.3 Simulation Results

The simulation work presented in this section is not a history match, neither can it be created as such with the work conducted in this thesis. The real history match of the GH field is obtained with complete data, such as heterogeneities, faults, and wells included in the giant field. Only a fraction of this complete field data is present in the Prototype model, meaning that no history

match was aimed in this thesis. The goal is to study and inspect the contribution of different fracture types. The historical production and pressure data are used as a reference line for a better visual comparison of the results. This approximate comparison seems reasonable because both the GH field's history match and the result obtained from the Prototype model are products of real data taken from the field.

In the sector of the Prototype model, no drilled or proposed injector well exists, so results obtained were only valid for primary recovery. The pressure support is solely conducted by two existing aquifers, cropped down from the GH-field to our sector boundaries. In Figure 92, the oil production of the producer well GS_033 from the Prototype model with different combinations of fracture types is presented. The red dots stand for the observed data in this time period from the well, whereas the curves are simulation results. As expected from the studies with the synthetical models, higher production is achieved with all fractures included. Even a nice trend with the observed history data could be found if all fractures are included. In fact, the cases with all fractures and with major, medium and minor, results in the same curve. This indicates that hairline fractures do not contribute to oil production. The contribution of the minor fractures is significant compared to the hairline fractures but not as high as the contribution of the medium fractures. Although the trend might be coherent with the historical data, the decline of the curves is prominent. This is as expected because the Prototype model represents only a fraction of the whole field.

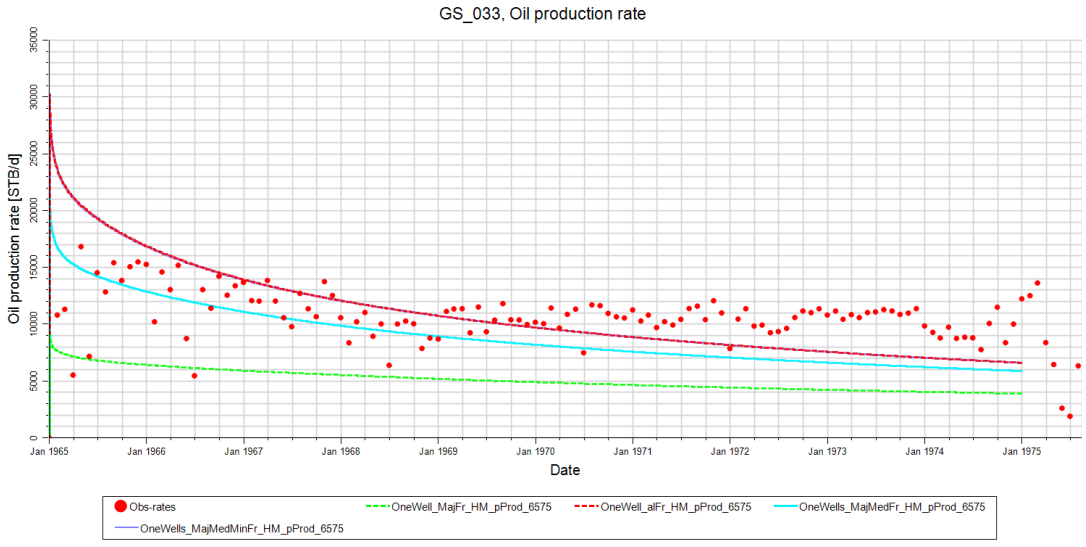

Figure 92: Oil production rates of cases with different fracture type combinations for well GS_033

A similar trend can be observed for the pressure curves, which are shown in Figure 93. Once more, differentiation between all fracture cases, including major, medium, and minor, is possible. As mentioned before, direct comparison with the observed pressure is not reasonable, but it provides visual verification of the trends. The results obtained are only for the mentioned

well. Another producer well is available in this period from 1965 up to 1975 in the Prototype model. The same fracture contribution trend could be observed for this second well, indicating that fractures significantly impact this field recovery.

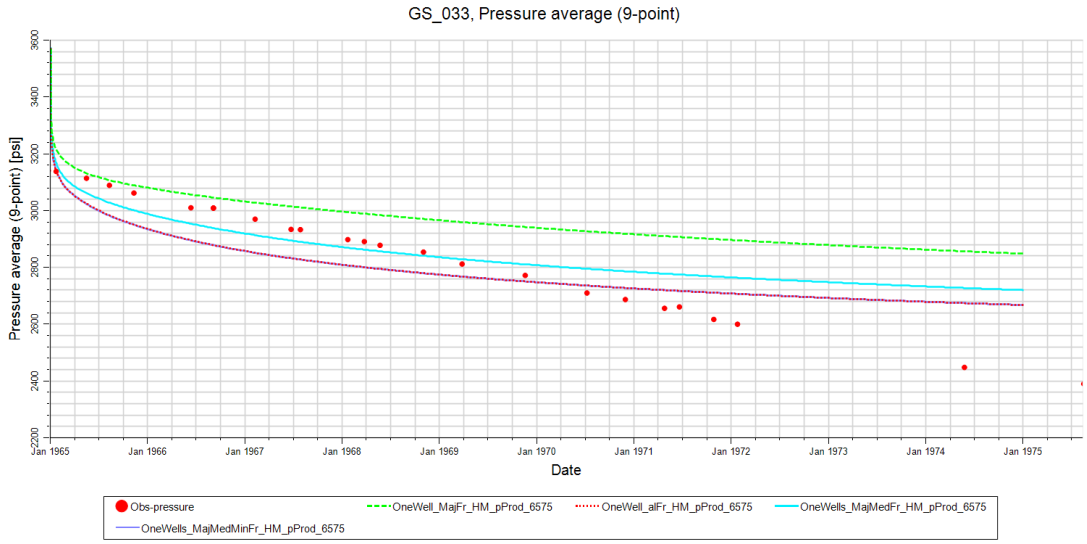

Figure 93: Pressure trend of cases with different fracture type combinations for well GS_033

4.5 Dimensionless Number Calculation

Dimensional numbers were calculated to study how capillary, gravitational or viscous forces affect secondary production schemes in fractured reservoirs. A similar approach was chosen as published in the literature (Zhou, et al., 1993; Heeremans, et al., 2006), using Eq. 2.3.2 and Eq. 2.3.3 from chapter 2.3. By conducting the sensitivity analysis for waterflooding and gas injection discussed in chapter 4.3.2.1 and chapter 4.3.3.1, multiple simulation cases were created to feed the mentioned equations for the capillary and gravity number analysis. A selection of the cases with calculated dimensionless numbers is shown in Table 19. The values presented in this table feature only cases considering major, medium, and minor fractures from the sensitivity runs. This way, it is ensured to implement all the fractures into the dimensionless number calculation. The numbers are defined in a way to represent certain force ratios. The capillary number in this work is a ratio between capillary and viscous force, whereas the gravity number represents gravity over viscous force. Required assumptions and relationships necessary for the proper calculation of dimensionless numbers are provided in the following section.

As the capillary number $N_{cv,m}$ is a function of the transverse capillary pressure p_c^*, the following equation was used as an approximation:

$$p_c^* = 4\sigma \cos(\theta) \sqrt{\frac{c * \Phi}{k_m}} \qquad \text{(Eq 4.5.6)}$$

with c being a material-dependent constant, σ the interfacial tension (N/m), Φ the porosity, θ the contact angle and k_m the matrix permeability (m^2). The constant c is taken for glass bed packs to be 0.02, and glass beds are considered to be strongly water wet, allowing for the simplification that $\cos(\theta) = 1$ (Zhou, et al., 1993). The gravity number $N_{gv,f}$ is a function of fracture permeability, but the permeability is not constant if multiple fracture types are used. The following relationship based on the harmonic average was found to work good for the purpose of this work:

$$k_{f,avg} = \frac{3}{\frac{1}{k_{f,Maj} n_{Maj}} + \frac{1}{k_{f,MajMed} n_{MajMed}} + \frac{1}{k_{f,MajMedMin} n_{MajMedMin}}} \qquad \text{(Eq 4.5.2)}$$

with $k_{f,Maj} n_{Maj}$ being the product of the major fracture permeability multiplied with the number of major fractures present in the model. $k_{f,MajMed} n_{MajMed}$ and

$k_{f,MajMedMin}n_{MajMedMin}$ represent the products analogically for the fracture type combinations of major and medium fractures and major, medium, and minor fractures.

The Darcy flow velocities q_m and q_f (m/s) required for calculation of both dimensionless numbers (capillary and gravity number) are assumed to be equal for the capillary number, representing the matrix domain, and the gravity number, representing the fracture domain. The following relationship gives Darcy's equation:

$$q_m = q_f = \frac{\mathrm{V} * k_m * \sigma_{SF} * (p_{avg} - p_{BH})}{\mu_w * L * H} \qquad \text{(Eq 4.5.3)}$$

where V is the matrix volume (m^3), k_m the matrix permeability (m^2), σ_{SF} the shape factor ($1/m^2$), p_{avg} the average reservoir pressure (Pa), p_{BH} the bottom-hole pressure of the producer, which is in contact with fractures, μ_w the viscosity of water (Pa.s) and L*H being the cross-sectional surface through the reservoir (m^2). The mobility ratio M was calculated separately for waterflooding and gas injection, using the expression:

$$M = \frac{k_{rD} * \mu_o}{k_{ro} * \mu_D} \qquad \text{(Eq 4.5.4)}$$

where k_{rD} stands for the relative permeability endpoint of the displacing phase (water or gas), μ_o is the oil viscosity (Pa.s), k_{ro} is the relative permeability endpoint of oil and μ_D stands for the viscosity of the displacing fluid (Pa.s). The relative permeability endpoints were adjusted for the mobility ratio governing the fluids in the matrix for every simulation case necessary. A constant value was taken for the mobility ratio of fluids inside the fractures because the relative permeability endpoints of fluids inside the fractures were assumed to be constant, with $k_{rw,f,end} = 1$, $k_{ro,f,end}=1$ and $k_{rg,f,end} = 0.5$.

4.5.1.1 Results

The sensitivity study was conducted to study the matrix-fracture interactions and is based on the sensitivity runs presented for the waterflooding and gas injection cases in the 3D cube model. The calculation for each case was done in Excel. The "standard" case is presented in Table 18. Gravity and capillary number were calculated for all sensitivity cases and were put together with the recovery factor of each case.

Table 18: Sensitivity parameters of the standard case

	MajMedMinFr	
BHP_{WF}	245	bar
BHP_{GI}	250	bar
km	1	md
kf	1120	md
$q_{mf,w}$	5.76E-06	m/s
$q_{mf,g}$	9.6E-07	m/s
μ_o	0.727	cP
ρ_o	855	kg/m^3
$k_{rw,end}$	0.1381	-
$k_{rg,end}$	0.12	-
$k_{ro,end}$	0.41	-
M_{ow}	0.408125	-
M_{og}	5.813675	-

Waterflooding Standard case	
Ngv,f	**0.208656**
Ncv,m	**0.000738**
Ngv,f	**0.208656**

Gas Injection Standard case	
Ncv,m	**0.026081**
Ngv,f	**12.22896**

Parameters used for the dimensionless number vs. recovery factor study were BHP of the producer, viscosity of the oil, fracture permeability, and matrix permeability. In Table 19, the values of the changed parameters are shown. Calculated dimensionless numbers and the ultimate recovery factor are also included. Figure 94 illustrates these results in a clustered column chart. In general, waterflooding produces more oil than gas injection in the 3D cube. Changes in the BHP clearly affect the ultimate oil recovery reached, but viscosity has significantly more impact on production. Permeability changes, regardless of matrix or fractures permeability, hardly affect the waterflooding performance. The gas injection, although, shows sensitivity when fracture permeabilities are changed. This might be related to the discussed effect of an early breakthrough if fractures are too permeable (chapter 4.3.2.1).

Table 19: Sensitivity parameter values and results

	Waterflooding					Gas Injection				
			MajMedMin					MajMedMin		
Parameter	value	unit	Nc,m	Ng,m	Rf	value	unit	Nc,m	Ng,m	Rf
Standard	-	-	7.38E-04	2.09E-01	59%	-	-	2.61E-02	1.22E+01	35%
Low BHP	145	bar	4.19E-05	1.19E-02	52%	145	bar	2.48E-04	1.16E-01	24%
High BHP	225	bar	1.71E-04	4.86E-02	58%	225	bar	5.72E-04	2.68E-01	32%
Low visco	0.2377	cP	9.17E-04	8.80E-01	62%	0.2377	cP	1.02E-02	5.83E+00	40%
High visco	6.3835	cP	2.27E-04	1.64E-03	36%	6.3835	cP	5.69E-04	2.69E-01	15%
high kf	2066	md	7.38E-04	3.84E-01	59%	2066	md	4.35E-03	3.76E+00	31%
low kf	20	md	7.38E-04	3.72E-03	62%	20	md	4.35E-03	3.64E-02	57%
high km	50	md	3.69E-02	2.09E-01	63%	50	md	2.17E-01	2.04E+00	46%
int. km	5	md	3.69E-03	2.09E-01	62%	5	md	2.17E-02	2.04E+00	45%

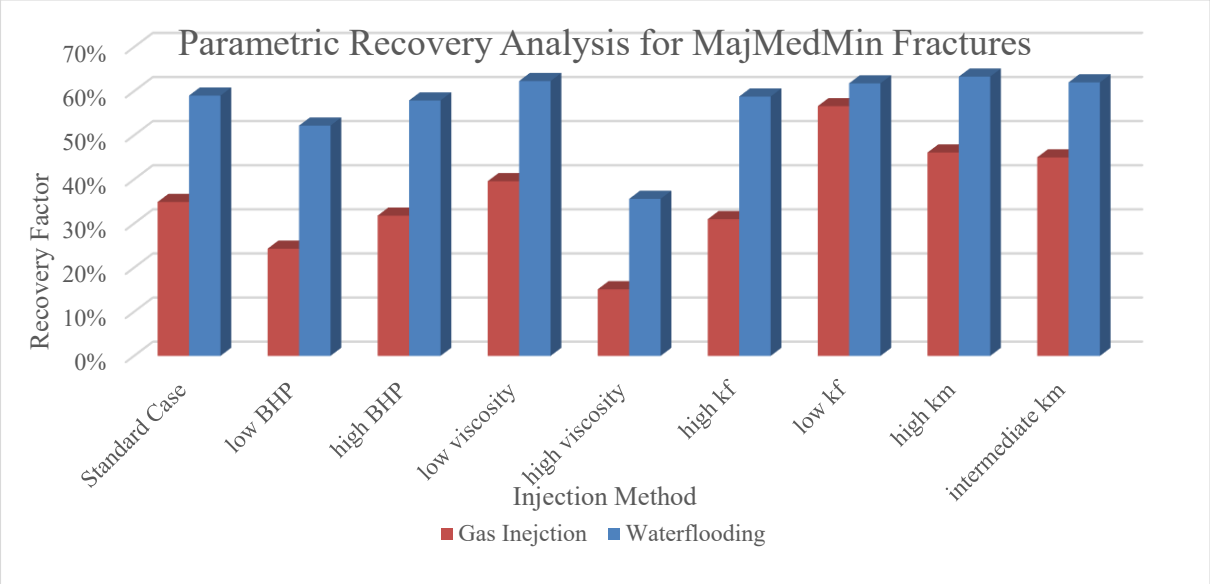

Figure 94: Sensitivity of different parameters

To analyze the performance of waterflooding and gas injection in fractured reservoirs, surface responses created from dimensionless numbers vs. the recovery factor can be used. Samples used for the surface plots were all sensitivity cases discussed in this work. Figure 95 illustrates the waterflooding surface response, and Figure 96 the response for the gas injection.

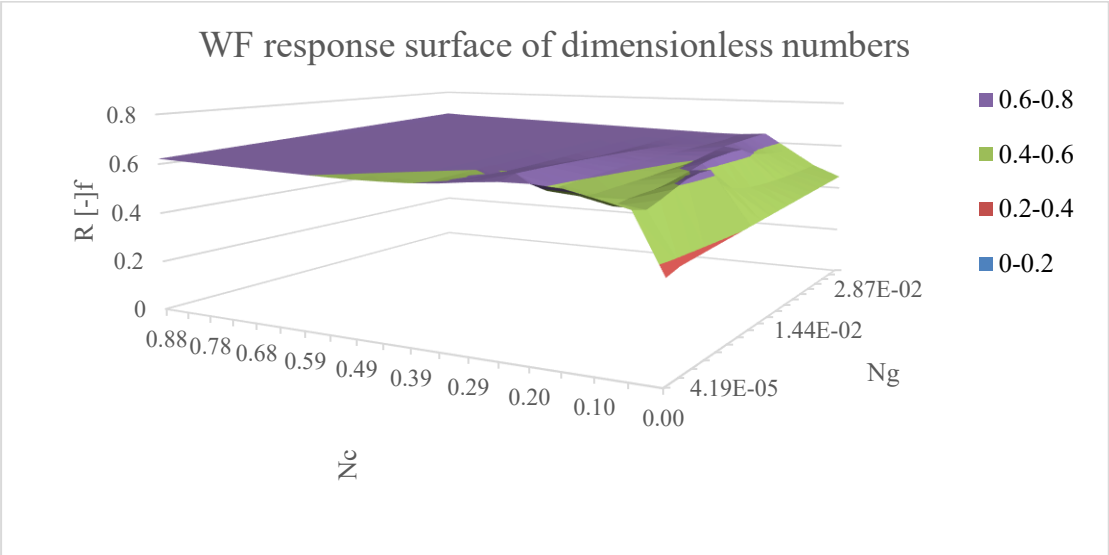

Figure 95: Waterflooding response surface

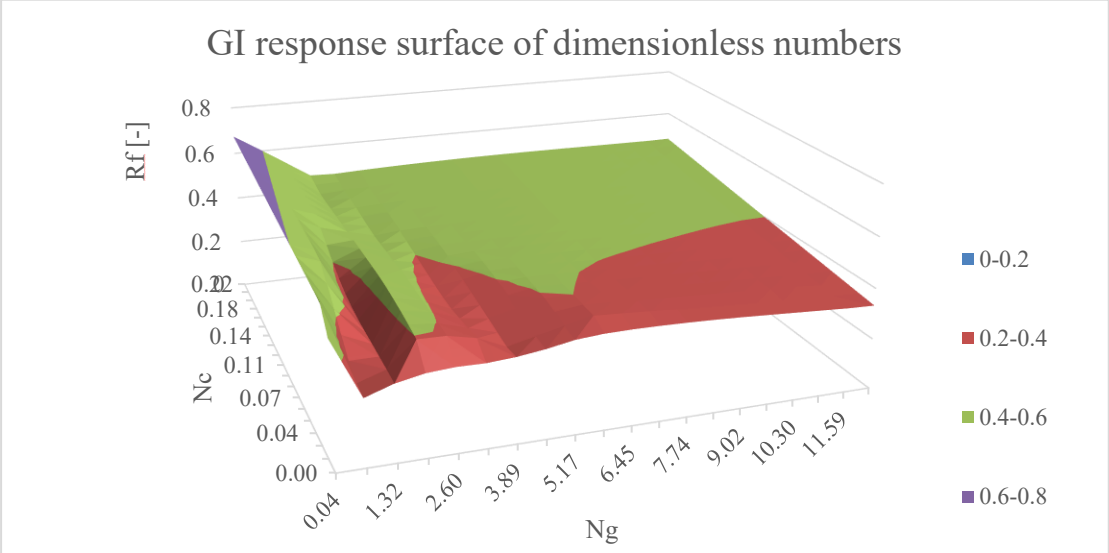

Figure 96: Gas injection response surface

Chapter 5

Conclusion

This chapter summarizes the simulation experiments, evaluates results, and gives a short outlook for future work.

5.1 Summary

This thesis features a group of synthetic models, ranging from 2D slices up to a 3D cube. The 2D slices serve as testing stations to prove the feasibility of different DFN's in combination with primary recovery, waterflooding, and gas injection in a dual-permeability continuum model. At the initial stage, the primary recovery runs in the 2D model were adjusted according to work conducted in the literature to ensure that results were valid. The obtained results from the 2D models were used to construct a 3D cube. Model parameters such as fluid model, SCAL data, well completion, matrix properties, and DFN properties were inherited from the 2D models into the 3D cube. The fluid model and SCAL data are real field data provided from the GH field in Iran. The 3D cube serves as a platform for multiple sensitivity cases for waterflooding and gas injection. Parameters that were studied in the sensitivity runs were the BHP of the producer, oil viscosity, matrix permeability, fracture permeability, and wettability conditions. A systematic calculation of dimensionless numbers was conducted for every sensitivity case, and the results were visualized in surface plots. Lessons learned from the 3D cube were utilized to run cases in the Prototype model, a real GH field sector. The primary production stage was conducted with different combinations of fracture sets to verify the impact of fractures on production.

5.2 Evaluation

Fractures improve the 3D cube's performance regarding natural depletion without any pressure support. The case with major, medium, and minor fractures performed 40% better

than with only the major fractures included. Fractures help to deplete the reservoir more efficiently, resulting in higher pressure drops and faster declines. If no fractures were included in the 2D models, drastically less oil recovery was observed. The contribution of each fracture type to production is analog to their aperture, with major fractures contributing the most and minor fractures contributing the least.

The gas injection cases in the 3D cube are very sensitive to early breakthroughs. Thus, fractures can have a negative effect on oil recovery. The results obtained point out that the injected gas rushes through the fractures and hardly enters the matrix in case of highly permeable fractures. When different fractures types are combined, for instance, major, medium, and minor fractures, then still the performance is retarded, because it seems that the gas had not enough time to enter the matrix and displace the oil. A smaller number of fractures, especially in combination with fracture permeabilities approximately in order of the matrix permeability magnitude, resulted in the most effective displacement. A similar matrix-dominated flow for the gas injection was observed through the sensitivity study and the dimensionless number. Changes in the matrix properties resulted in changes in the capillary number, which strongly impacted gas injection performance. These observed effects might be related to the matrix block size. When gas rushes through the fractures, it surrounds the matrix block, enabling gravity drainage to happen. Larger matrix block sizes result in more prominent gravity drainage and thus higher oil recovery.

In the case of waterflooding, fractures showed in the frame of this work positive effects. The more fractures are involved in the DFN, the better performance could be observed. The water injection utilizes the fractures so that with major, medium, and minor fractures, better results could be obtained than with cases that feature fewer fracture types. Ignoring fractures, lowering their number, or decreasing their permeability would lead to underestimating the model's potential. Fractures seem to help distribute the water in the model, allowing more effective oil displacement through the matrix. The water is imbibing the matrix and displacing the oil. It was found that it takes time before the matrix can react. For higher injection and production rates, this effect is especially good visible. Fractures are depleted very fast, after which a plateau in production can be observed up until the water starts imbibing the matrix and pushing more oil through the fractures towards the producer.

In the Prototype, model fractures were also observed to be key elements in oil production. Cases with all fractures included could generate results very close to the observed data from the whole field. Although this thesis does not feature a history match of the Prototype sector, the results still show a good trend-like match with the historical pressure and rate

data. When all fractures are included, the trend could successfully be matched. Removing fracture types from simulation cases resulted in less production. The contribution of each fracture type to the production corresponds to the findings of the synthetic models during primary production. Major fractures contributed most to the production, followed by medium and minor fractures; hairline fractures hardly contributed to the production. Visually no difference between the cases with all four fracture types and those without hairline fractures could be noticed.

Fractured reservoirs treated during primary production as non-fractured reservoirs, even though they are fractured, are overestimated according to the observed effects of this thesis. Without the transport capabilities of the fractures, the matrix alone cannot supply the observed production. Validating fractures, if any present, plays a key role in optimally understanding and using a given reservoir. Not all fractures contribute equally to oil production. Classification of fractures based on their aperture or permeability allows identification of which fractures contribute more and less. This is especially of interest when the contribution of the fractures is different for primary recovery, gas injection, and waterflooding.

5.3 Future Work

The subject of fractures' contribution to oil production during the different recovery stages of a hydrocarbon reservoir is vast. This thesis serves as a first step towards the goal to simulate the various mechanisms of fractures. Future work might involve a more detailed sensitivity analysis and dimensionless number calculation. Understanding the general behavior of the synthetic models better enables the easier implementation of a real field model. More work is required to understand how secondary production performs with different fracture types in a real field sector. Eventually, the fractures contribution when EOR methods are applied in a real field can be studied as a final step.

Chapter 6

References

Aghabarari, A., Ghaedi, M. & Riazi, M., 2020. Prediction of oil recovery in naturally fractured reservoirs subjected to reinfiltration during gravity drainage using a new scaling equation. *PETROL. EXPLORE. DEVELOP.,* 47(6), pp. 1307-1315.

Aghli, G., Moussavi-Harami, R. & Mohammadian, R., 2019. Reservoir heterogeneity and fracture parameter determination using electrical image logs and petrophysical data (a case study, carbonate Asmari Formation, Zagros Basin, SW Iran). *Petroleum Science,* Volume 17, pp. 51-69.

Aguilera, R., 1995. *Naturally Fractured Reservoirs.* 2; ISBN 13: 9780878144495; ISBN10: 0878144498 ed. s.l.: Pennwell Books.

AlQuaimi, B. I. & Rossen, W., 2017. New capillary number definition for. *Geophysical Research Letters,* Volume 44, pp. 5368-5373.

Bahrami, H., Rezaee, R. & Hossain, M., 2012. Characterizing natural fractures in tight gas reservoirs. *Journal of Petroleum Exploration and Production Technology,* 2(2), pp. 107-115.

Cheng, X., Kleppe, J. & Torsæter, O., 2018. Simulation Study of Surfactant Imbibition Mechanisms in Naturally Fractured Reservoirs. *SPE-191309-MS,* p. 13.

Coll, C. & Muggeridge, A., 2001. Regional Upscaling: A New Method To Upscale Waterflooding in Heterogeneous Reservoirs for a Range of Capillary and Gravity Effects. *Society of Petroleum Engineers (SPE 74139),* p. 12.

Dershowitz, B., LaPointe, P., Eiben, T. & Wei, L., 2000. Integration of Discrete Feature Network Methods With Conventional Simulator Approaches. *SPE Reservoir Eval. & Eng. (SPE 62498),* 3(2), p. 6.

Doe, T., Lacazette, A., Dershowitz, W. & Knitter, C., 2013. Evaluating the Effect of Natural Fractures on Production from Hydraulically Fractured Wells Using Discrete Fracture Network Models. *Unconventional Resources Technology Conference URTeC 1581931,* Issue 12-14, p. 10.

EIA, U., 2021. *U.S. Energy Information Administration.* [Online]
Available at: https://www.eia.gov/outlooks/steo/report/global_oil.php
[Accessed 31 08 2021].

Fatemi, S. & Bahonar, M., 2009. Simulation Analysis of the Effects of Fractures Geometrical Properties on the Performance of Vapor Extraction (VAPEX) Process. *PETSOC-2009-001.*

Fatemi, S., Ghotbi, C., Kharrat, R. & Badakhshan, A., 2011. Application of Toe-to-Heel Air Injection (THAI) Process in Fractured Carbonate Systems: 3D Simulation of the Effect of Fractures Geometrical Properties. *SPE 143434.*

Fatemi, S., Kharrat, R. & Vossoughi, S., 2011. : Investigation of Steam Assisted Gravity Drainage (SAGD) and Expanding Solvent-SAGD (ES-SAGD) Process in Complex Fractured Models: Effects of Fractures' Geometrical Properties. *SPE 150082.*

Fatemi, S., Kharrat, R. & Vossoughi, S., 2014. Investigation of Top-Down In-Situ Combustion Process in Complex Fractured Carbonate Models: Effects of Fractures' Geometrical Properties. *CSUG/SPE 149314.*

Firoozabadi, A., 2000. Recovery Mechanisms in Fractured Reservoirs and Field Performance. *J. Can. Pet. Technol.,* 39(11).

Franchi, J., 2006. *Principles of Applied Reservoir Simulation.* Third Edition ed. s.l.: GPP-Golf Professional Publishing is an imprint of Elsevier.

Ghoodjani, E., Kharrat, R., Vossoughi, M. & Bolouri, S., 2011. A Review on Thermal Enhanced Heavy Oil Recovery from Fractured Carbonate Reservoirs. *Journal of Petroleum & Environmental Biotechnology,* Vol. 2(2), pp. 1-7.

Gilman, J., Wang, H., Fadaei, S. & Uland, M., 2011. A New Classification Plot for Naturally Fractured Reservoirs. *Canadian Society for Unconventional Gas/ Society of Petroleum Engineers,* Volume CSUG/SPE 146580, p. 17.

Golf-Racht, T. v., 1982. *Fundamentals of Fractured Reservoir Engineering.* 1st Edition, Volume 12 ed. s.l.: Elsevier Science.

Gong, J. & Rossen, W., 2016. Shape factor for dual-permeability fractured reservoir simulation: Effect of non-uniform flow in 2D fracture network. *Elsevier, Fuel 184,* pp. 81-88.

Gong, J. & Rossen, W., 2017. Modeling flow in naturally fractured reservoirs: effect of fracture aperture distribution on dominant sub-network for flow. *Elsevier, Pet. Sci. 14,* pp. 138-154.

Gong, J. & Rossen, W., 2018. Characteristic fracture spacing in primary and secondary recovery for naturally fractured reservoirs. *Elsevier, Fuel 2213,* pp. 470-485.

Green, D. & Willhite, C., 1998. *Enhanced Oil Recovery.* Vol. 6 (ISBN: 978-1-55563-077-5) ed. s.l.: SPE Textbook Series.

Heeremans, J., Esmaiel, T. & Kruijsdijk, C. v., 2006. Feasibility Study of WAG Injection in Naturally Fractured Reservoirs. *SPE 100034,* p. 10.

Jiang, L. et al., 2020. Simulation and Optimization of Dynamic Fracture Parameters for an Inverted Square Nine-Spot Well Pattern in Tight Fractured Oil Reservoirs. *Hindawi Geofluids,* Issue Article ID 8883803, p. 9.

Kharrat, R., 2021. *Reservoir Characterization with respect to fractures effect on production data,* Leoben: internal report MUL.

Kharrat, R., Zallaghi, M. & Ott, H., 2021. Performance Quantification of Enhanced Oil Recovery Methods in Fractured Reservoirs. *Energies,* 14(4739).

Khelifa, C., Zeddouri, A. & Djabes, F., 2014. Influence of natural fractures on oil production of unconventional reservoirs. *Elsevier Energy Procedia 50,* p. 360 – 367.

Kleppe, J. & Morse, R., 1974. Oil Production from fractured Reservoirs by Water Displacement. *Society of Petroleum Engineers (SPE-5084-MS),* p. 20.

Kovscek, A., Zhou, D., Jia, L. & Kamath, J., 2001. Scaling of counter-current imbibition processes in low-permeability porous media. *J. Pet. Sci. Eng.,* Volume 33, pp. 61-74.

Litvak, B., Satter, A. & Etebar, S., 1988. An Analysis of Naturally Fractured Reservoir Performance Using a Novel Fractured Reservoir Simulator. *SPE 17615,* p. 10.

Liu, J. et al., 2018. Numerical Simulation Study on Fracture Parameter Optimization in Developing Low-Permeability Anisotropic Reservoirs. *Hindawi Geofluids,* Issue Article ID 1690102, p. 9.

Ocampo, A., Restrepo, A., Clavijo, J. & Mejia, J., 2020. Successful Foams EOR Field Pilot in a Naturally Fractured Reservoir by the Injection of the Foaming Agent Dispersed in the Gas Stream. *SPE-200377-MS,* p. 7.

Ocampo, A., Restrepo, A., Lopera, S. & Mejia, J., 2018. Creation of Insitu EOR Foams by the Injection of Surfactant in Gas Dispersions - Lab Confirmation and Field Application. *SPE-190219-MS,* p. 8.

Rashid, B., Fagbowore, O. & Muggeridge, A., 2012. Using Dimensionless Numbers to Assess EOR in Heterogeneous Reservoirs. *ECMOR XIII - 13th European conference on the Mathematics of Oil Recovery,* Issue B03, p. 24.

Rezaveisi, M., Ayatollahi, S. & Rostam, B., 2012. Experimental Investigation of Matrix Wettability Effects on Water Imbibition in Fractured Artificial Porous Media. *Elsevier, Journal of Petroleum Science,* pp. 165-171.

Rostami, B., Kharrat, R., Ghotbi, C. & Tabatabaie, S., 2010. Gas-Oil Relative Permeability and Residual Oil Saturation as Related to Displacement Instability and Dimensionless Numbers. *Institut français du pétrole,* 65(2), pp. 299-313.

Saidi, A. M., 1987. *Reservoir Engineering of Fractured Reservoirs (Fundamental and Practical Aspects)*. Paris: TOTAL Edition Presse.

Sarkar, S., Toksöz, N. & Burns, D., 2004. Fluid Flow Modeling in Fractures. *Earth Resources Laboratory Dept. of Earth, Atmospheric and Planetary Sciences, Massachusetts,* Issue 2004-05, p. 41.

SayedAkram, N. & Mamora, D., 2011. Simulation Study on Surfactant-Polymer Flood Performance in Fractured Carbonate Reservoir. *SPE 149106,* p. 12.

Schlumberger, 2021. *Schlumberger's Petrel E&P Software Platform.* [Online]
Available at: https://www.software.slb.com/products/petrel
[Accessed 14 05 2021].

Silva, R. & Maini, B., 2016. Evaluation of Gas Assisted Gravity Drainage GAGD in Naturally Fractured Reservoirs NFR. *SPE-179585-MS,* p. 17.

Singha Ray, D. et al., 2012. Characterizing and modeling natural fracture networks in a tight carbonate reservoir in the Middle East: A methodology. *Bulletin of the Geological Society of Malaysia,* Volume Volume 58, pp. 29-35.

Sönnichsen, N., 2021. *Statista.* [Online]
Available at: https://www.statista.com/statistics/271823/daily-global-crude-oil-demand-since-2006/
[Accessed 31 08 2021].

Spence, G. et al., 2014. Advances in the study of naturally fractured hydrocarbon reservoirs: a broad, integrated interdisciplinary applied topic. *Geological Society, London, Special Publications,* Volume 374, pp. 1-22.

Talluru, G. & WuMewbourne, X., 2017. Using Data Analytics on Dimensionless Numbers to Predict the Ultimate Recovery Factors for Different Drive Mechanisms of Gulf of Mexico Oil Fields. *Society of Petroleum Engineers (SPE-187269-MS),* p. 20.

Torres, F. et al., 2020. Comparison of Dual Porosity Dual Permeability with Embedded Discrete Fracture Model for Simulation Fluid Flow in Naturally Fractured Reservoirs. *ARMA - American Rock Mechanics Association,* 20(1462).

Wang, J., Wei, Y. & Luo, W., 2019. A Unified Approach To Optimize Fracture Design of a Horizontal Well Intercepted by Primary- and Secondary-Fracture Networks. *SPE Journal (SPE194490),* p. 18.

Wan, T., Sheng, J., Soliman, M. & Zhang, Y., 2016. Effect of Fracture Characteristics on Behavior of Fractured Shale-Oil Reservoirs by Cyclic Gas Injection. *Society of Petroleum Engineers (SPE 168880),* p. 6.

Wei, Y., Xiaohu, H., Malin, L. & Weihong, W., 20119. Investigation of the Effect of Natural Fractures on Multiple Shale-Gas Well Performance Using Non-Intrusive EDFM Technology. *Energies,* Volume 12(5), p. 16.

Zhou, D., Fayers, F. & Orr Jr., F., 1993. Scaling of Multiphase Flow in Simple Heterogeneous Porous Media. *SPE/DOE 27833,* p. 11.

Zimmerman, R. & Bodvarsson, G., 1996. Hydraulic Conductivity of Rock Fractures. *Transport in Porous Media,* Issue 23, pp. 1-30.

Zuo, L., Tan, X., Yu, W. & Hu, X., 2019. Fracture Detection and Numerical Modeling for Fractured Reservoirs. *Energies 386,* p. 15.

Appendix A

Appendix - SCAL data

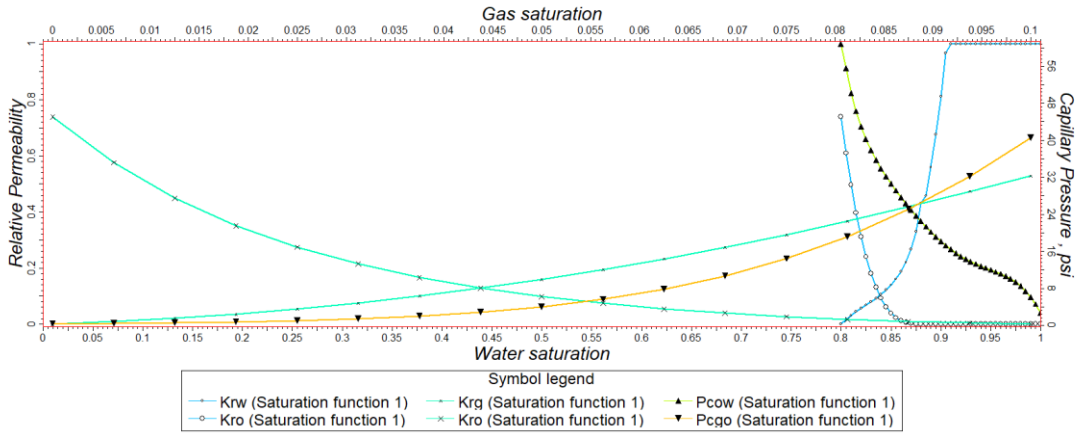

Figure 97: Saturation function 1

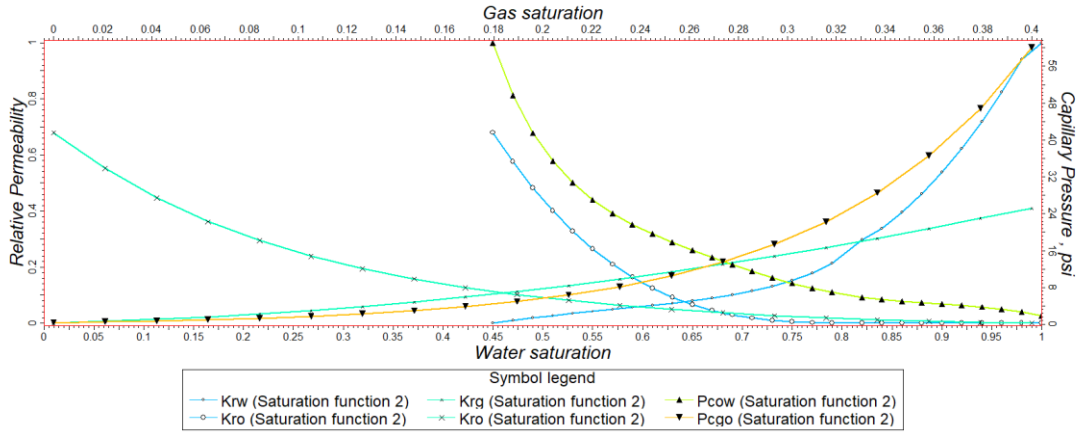

Figure 98: Saturation function 2

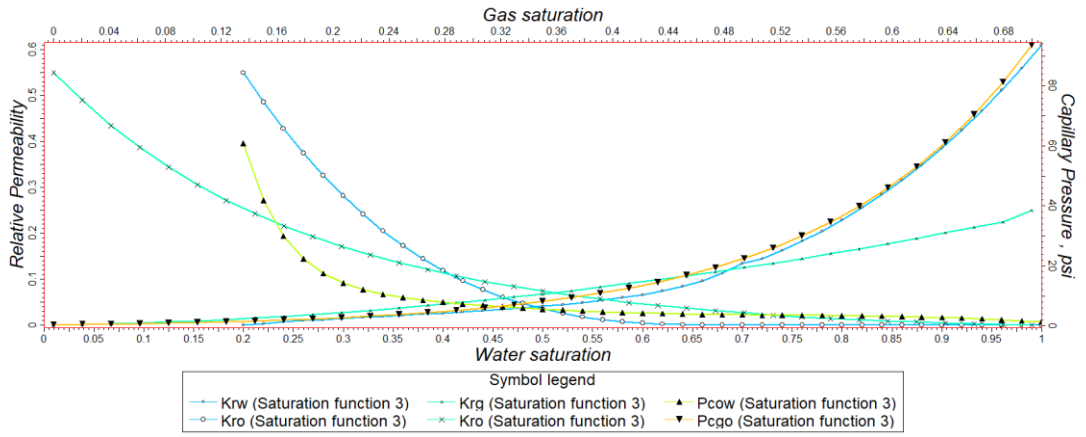

Figure 99: Saturation function 3

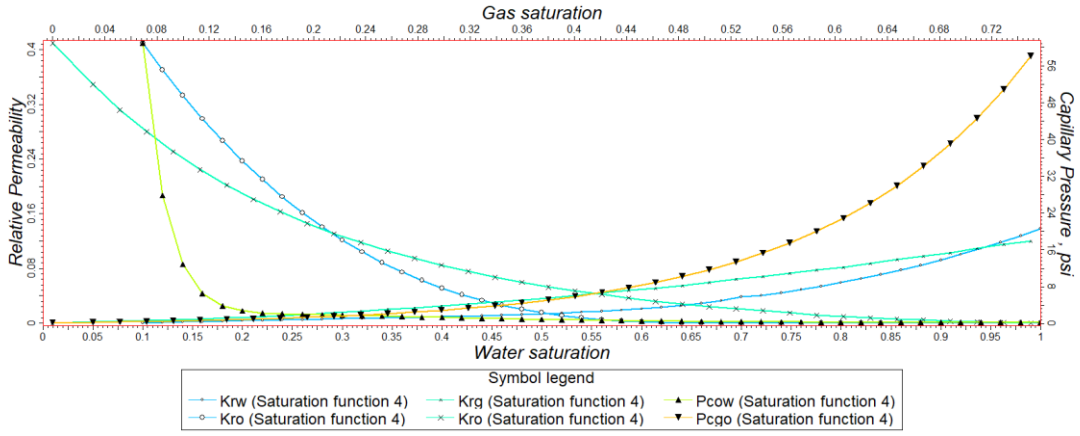

Figure 100: Saturation function 4

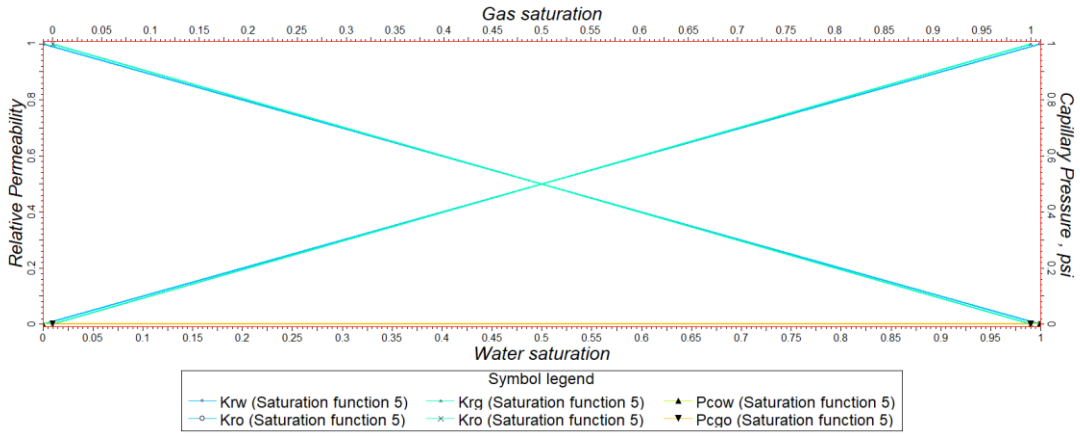

Figure 101: Saturation function 5

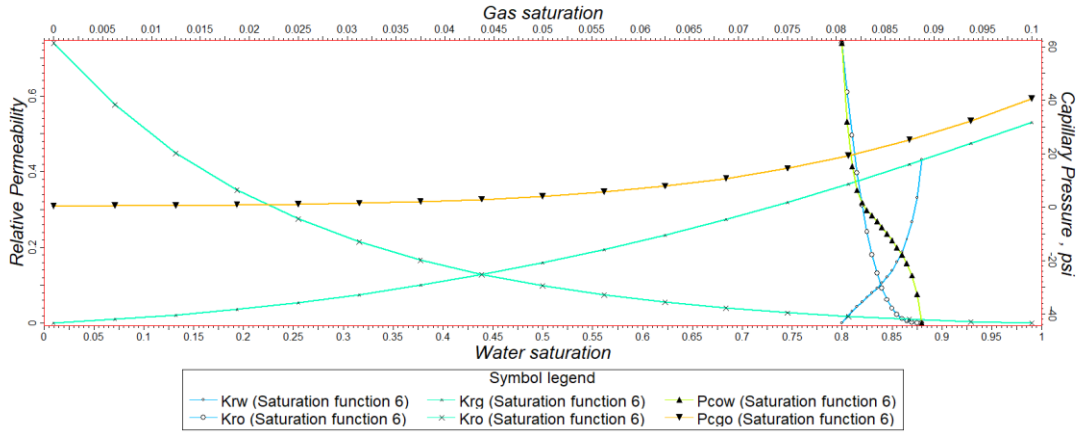

Figure 102: Saturation function 6

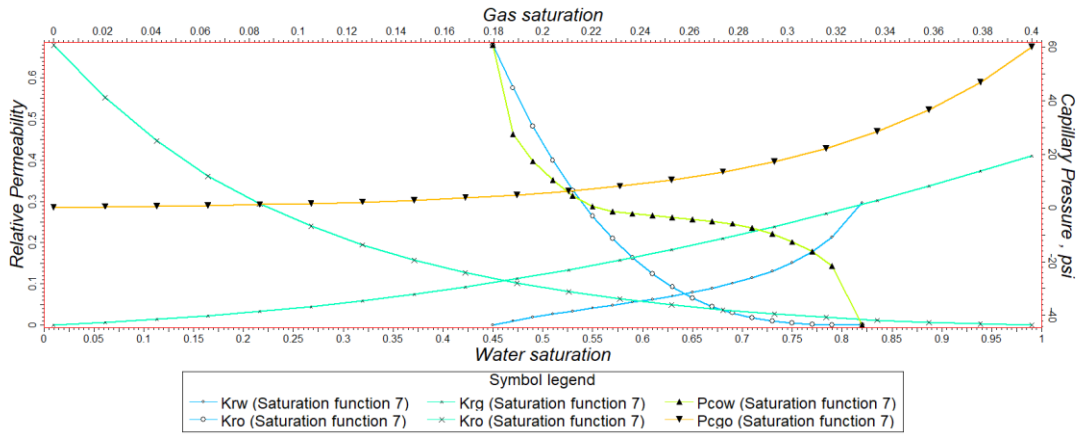

Figure 103: Saturation function 7

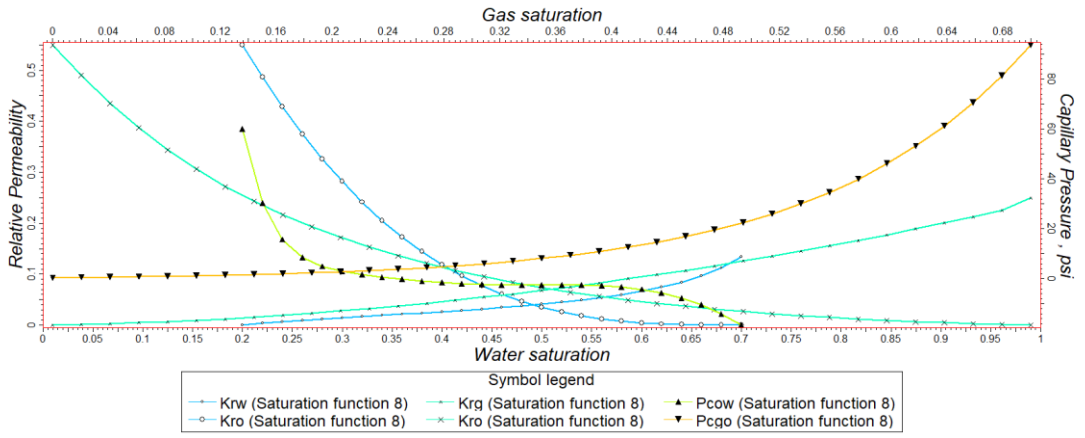

Figure 104: Saturation function 8

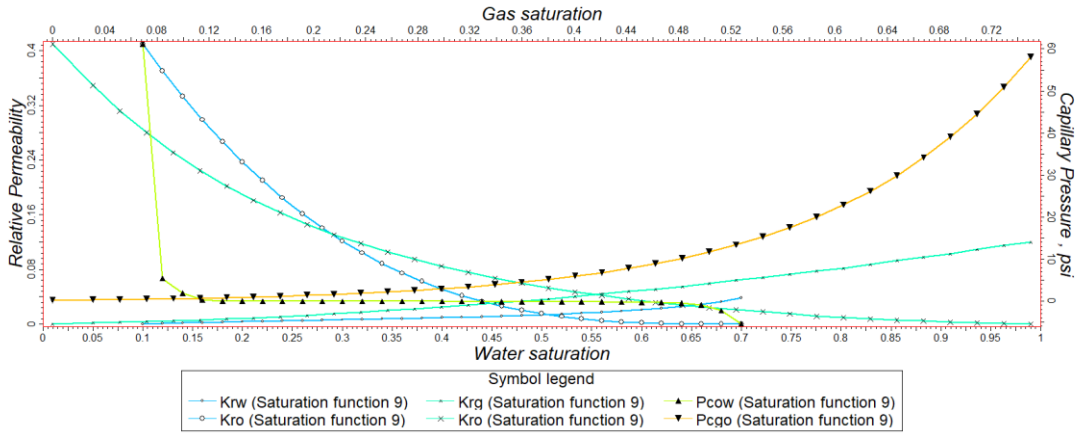

Figure 105: Saturation function 9